Machines with Non-conventional Topologies for More Electric Applications

by

Jiri Dusek

Submitted to the Faculty of Engineering
in partial fulfilment of the requirements for the degree of

Doctor of Philosophy in Electrical Engineering

at the

UNIVERSITY OF NOTTINGHAM

January 2017

Author . . . .
Faculty of Engineering
January 20, 2017

Certified by . . . .
Chris Gerada
Professor
Thesis Supervisor

Certified by . . . .
Puvan Arumugam
Research Fellow
Thesis Supervisor

Machines with Non-conventional Topologies for More Electric Applications

by

Jiri Dusek

Submitted to the Faculty of Engineering
on January 20, 2017, in partial fulfilment of the
requirements for the degree of
Doctor of Philosophy in Electrical Engineering

Abstract

This thesis investigates the design, performance and fault tolerant capability of electric machines with unconventional topologies used in more electric drive applications. Two different machine topologies are analysed: Flux reversal permanent magnet machine and a field wound flux switching machine.

Initially, unconventional flux reversal machine topology in which the volume of the permanent magnet material is minimised to improve the fault tolerance capability and lower the costs whilst achieving significant improvement in the torque is investigated through a simulation and validated through experimental work. It is shown that although the machine belongs to the fault tolerant category, an inter-turn short circuit fault will be a problematic as the magnetic flux from the magnet cannot be neutralised and can cause severe damage to the machine under certain conditions.

This however, does not mean that the topologies with permanent magnet material are not suitable for the fault tolerant solutions. If the appropriate design selection in terms of slot and pole numbers is made, the negative influence of the permanent magnet material can be minimised. Therefore, the influence of the slot pole combination on both fault tolerance and performance is investigated and the results are demonstrated on the set of permanent magnet synchronous machines. It is shown that low rotor pole number machines have better fault tolerance capability whilst high rotor pole number machines are lighter and provide higher efficiency.

To overcome the challenges related to the short circuit fault, the topology which eliminates the permanent magnet material and works on a basis of the wound excitation is developed. As the short circuit fault cannot be fully eliminated, a solution which prevent the catastrophic failure and minimises the consequences by using wound excitation system on the stator side instead of permanent magnets is proposed. The modification of a permanent magnet synchronous machine towards improvement of the fault tolerance is presented in detail. Different rotor structures are investigated and optimised to maximise the torque performance. It is shown that using stator of existing machine and replacing the current rotor containing permanent magnets not only improves the fault tolerance, but also reduces the manufacturing and material costs.

Thesis Supervisor: Chris Gerada
Title: Professor

Thesis Supervisor: Puvan Arumugam
Title: Research Fellow

Acknowledgments

To my closest family, friends and colleagues. I would have never been able to begin and accomplish this journey without you.

Contents

List of Tables

List of Figures

Glossary

AG air gap. 97, 98, 99

BEMF back electromotive force. 7, 9, 29, 34, 46, 45, 46, 88, 91, 92, 95, 104

d–q direct – quadrature. 6, 21, 36, 37, 38, 55

DSPMM doubly salient permanent magnet machine. 24, 25

ECS environmental control system. 15

EMF electro motive force. 26, 28, 38

FE finite element. 19, 25, 54, 102

FEA finite element analysis. 7, 21, 22, 33, 40, 46, 53, 104, 108, 110

FEM finite element method. 40, 109

FFT fast Fourier transformation. 95

FRM flux reversal machine. 6, 7, 20, 21, 23, 24, 25, 26, 27, 28, 29, 30, 32, 33, 34, 36, 37, 38, 39, 40, 41, 42, 46, 48, 50, 51, 52, 55, 108

FT fault tolerant. 16, 18, 20, 21, 22, 24, 55, 57, 58, 108, 109, 110

FT-PM fault tolerant permanent magnet. 59

FTe fault tolerance. 16, 19, 20, 43, 55, 81, 82, 83, 84, 108, 109

FWFS field wound flux switching. 8, 9, 10, 82, 84, 86, 88, 89, 90, 91, 97, 98, 101, 103, 104, 105, 107, 118

FWFSM field wound flux switching machine. 21, 22, 89, 102

GA genetic algorithm. 62

IPMSM inset permanent magnet synchronous machine. 85, 91

MEA more electrical aircraft. 14, 15

MMF magneto motive force. 25

MOGA multi objective genetic algorithm. 21, 56, 59, 109

PF power factor. 34

PM permanent magnet. 6, 18, 19, 21, 24, 26, 28, 29, 30, 32, 33, 34, 54, 55, 57, 81, 83, 84, 91, 105, 108, 109

PMM permanent magnet machine. 26

PMSM permanent magnet synchronous machine. 20, 22, 24, 28, 37, 38, 39, 50, 53, 55, 82, 83, 97

RAT ram air turbine. 14

S/P slot/pole. 19, 59, 109

SC short circuit. 8, 16, 19, 20, 21, 55, 57, 58, 59, 60, 62, 63, 64, 71, 72, 73, 75, 76, 75, 76, 77, 78, 79, 81, 83, 84, 109

SM-PMSM surface mounted permanent magnet machine. 20, 62

SRM switched reluctance machine. 24, 26

Chapter 1

Introduction

In this chapter, the introduction and brief overview on the thesis content is given. The idea and motivation behind the chosen topic is explained and the thesis structure is outlined. Main aim of this chapter is to provide the reader with basic idea of technical challenges that have been addressed in this thesis.

1.1 More electric applications

The term ”more electric” is mostly associated with an aircraft or aerospace applications in which electrical power is employed for a range of both primary and secondary functions including actuation, de-icing, cabin air conditioning and engine start and power generation. Electrification transformed the conventional engine control and has removed the need for hydraulic and bleed air systems. This results in efficient, safe, reliable and light weight solution that will lead to reduction in fuel consumption and also maintenance costs. However achieving greater reliability is still challenging since the system which includes electrical machines controlled by power electronics requires to be operated in extreme environments and is expected to be more and more efficient [1].

Figure 1-1 illustrates how the concept utilising the more electrical aircraft (MEA) differs from conventional aircraft system.

The adoption of the MEA within the aircraft provides enormous benefits such as:

- Replacing the engine-bleed system by electric motor-driven pumps reduces the complexity and the installation cost
- Replacement of hydraulic unit (including centralised reservoir, pump and channel) improves the aircraft efficiency, reliability, and reduces vulnerability, complexity, weight, installation and running cost.
- Electrical starting of the aero-engine by employing the engine starter generator system removes the engine tower shaft and gears, power take-off shaft, accessory gearboxes. This reduces the fuel burn and improves the efficiency.
- Using a fan shaft generator that allows emergency power extraction

under windmill conditions, removes the conventional inefficient single-shot ram air turbine (RAT)

- To pressurise the cabin, electrically driven environmental control system (ECS) compressors and heater/cooler units reduces the cost and operational time of the main engine. [2].

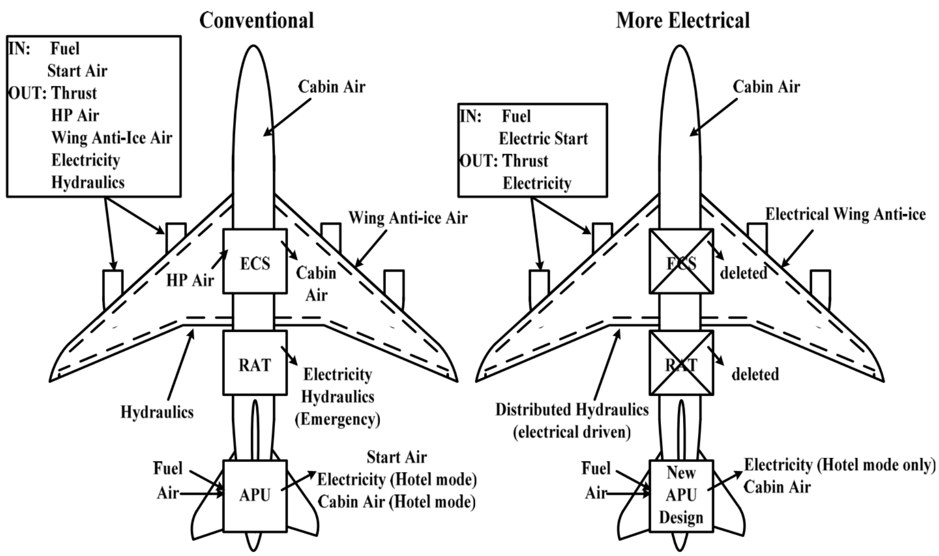

Fig. (1-1): Comparison between conventional and MEA systems [3]

In general, the concept of the MEA revolutionises the aircraft architecture and the aerospace industry completely. It provides significant improvements in terms of aircraft space, weight, fuel consumption, cost per passenger, reliability and maintainability. On the contrary, the concept of the MEA increases the requirements on the aircraft electric power systems, namely areas of power generation and power management. The challenges related to high power density and sufficient reliability are enormous and these need to be addressed.

The power density and reliability are two conflicting requirements involved in a design of electrical drives which are the heart o the MEA. Reliability has been defined as ”the probability that the equipment will give the satisfactory performance, in the specified environments and for the required interval of time, in the manner intended” [4]. Attaining hundred percent reliability is impossible and very often the designer aims to achieve a degree of reliability governed by the function the machine has to perform. Clearly where the function is directly influencing the safety of the aircraft, the reliability must be of the highest priority, even at the penalty of weight and cost.

1.2 Fault tolerance and faults

As previously mentioned, the reliability is directly related to the safety of the system. So the reliability can be improved if the system is designed to tolerate any type of fault. Such system design is referred to as the fault tolerant (FT) system. The term FT has been defined across research disciplines as a basic requirement for modern electric motors and generators and can be achieved with a number of integrated approaches, like condition monitoring, post-fault control strategies and suitable system design architectures [5, 6, 7, 8]. In general, the fault tolerance (FTe) is defined as the property that enables a system to continue operating properly in the event of the failure of (or one or more faults within) some of its components [9]. The concept of a FT machine is that it will continue to operate in a satisfactory manner after sustaining a fault. The term ”satisfactory” implies a minimum level of performance once faulted. The degree of fault that must be sustainable should be related to the probability of its occurrence. For most safety critical applications, it is accepted that the drive must be capable of rated output after the occurrence of any fault [10].

The faults in rotating electric machines can be classified in many ways, depending on the fault nature or cause. Based on place where the fault occurs, we recognise stator or rotor faults. Bearing fault, unbalanced rotor or bent shaft are good examples of mechanical faults, while open or SC faults are examples of faults of an electrical nature. Thus, the machine should be designed to tolerate these faults without compromising the performance.

1.3 Torque/power density

In the more electrical applications, the torque density and consequently the power density is one of the most important factors which is used to evaluate the performance of the system. The definition of "torque density" depends on the constraints of the application. In applications where the utilisation of space is critical, it makes sense to consider the torque density with respect to the volume, and thus it can be defined as the density in terms of the volume (Nm/m^3 or Nm/l). In applications limited by the weight, the obvious parameter for evaluation of the torque density is the torque per unit of the mass (Nm/kg). In case of boundaries constrained by the current available, then the torque density will be express as the torque per ampere (Nm/A). Hence it is not possible to define the torque density in general, but it always depends on the concrete application constrains, limitations or boundaries, that the design has to meet and respect.

The torque generated by the machine is proportional to product of its rotor volume ($\propto$ Diameter^2 x Length) and shear stress, where the shear stress is the product of the magnetic and electric loading. Thus, the high torque density can be achieved by increasing either current loading or magnetic loading or both while minimizing the volume. However, both the current loading and magnetic loading are limited and so torque density by several design factors. The electrical loading is restricted by factors such as the allowable slot area to accommodate the winding, the achievable packing factor of copper (K_f) in the stator slots, and the allowable copper current density based on maximum allowable winding temperature rise or demagnetisation limits of the magnetic materials. The electrical loading can be increased by adopting efficient thermal management in the slot or adopting deeper stator slots to minimise the losses and so heat. The magnetic loading is limited by saturation of the soft and hard magnetic materials. Though magnetic loading can be increased allowing for hard magnetic material within design, due to saturation limitation on soft magnetic core, the design is restricted and thereby restricting the torque density. To achieve a high torque density, these limitations must be considered.

1.4 Description of the problem

The permanent magnet machines are attracting a large amount of attention in aerospace applications due to their high torque and consequently power density [11, 12, 13, 14, 15]. These machines are required to be safe, reliable and available under tight weight, volume and cost constraints. To meet all of these demands, design trade-offs are usually made to balance these design requirements [16]. The common design approach is an adoption of the FT features within the electrical drive system. Such FT features allow the machine to fail safely, without any catastrophic damage and also enable the machine to maintain the same or comparable performance under fault to when the machine was healthy. The most commonly implemented method of fault tolerance is redundancy [17]. However, adding redundancy increases the system weight, volume and cost. In systems, where N+1 redundancy cannot be achieved due to these constraints, alternative FT features must be considered [18]. There is a number of the FT features which can be included in the PM machine designs which increase the availability of the machine without adding redundancy and its associated weight, volume and cost [18, 19, 20].

On the contrary, minimising the volume of the PM material reduces the machines performance, but will also lower the manufacturing cost and lower the consequent effect of eventual electrical fault and thus improved the FTe. Certainly, the way to lower the manufacturing cost and improvement of the controllability in case of fault is to design electric machine with no PMs at all. Omitting the PM materials brings challenges related to torque density that need to be addressed.

1.5 The aim and objectives

The main purpose of this work is to identify a design solution for the direct drive application with emphasis on torque density, the FTe and production costs. The study has been carried out through both analytical and finite element (FE) tools and then, experimentally validated. The key objectives of the thesis can be summarised as follows:

- Investigation on the flux reversal PM machine designed for low speeds, direct drive applications: the study focuses on minimising the volume of the rare earth materials combined with the magnetic gearing effect to amplify the torque performance while maintaining minimal machines size, volume and cost.

- Determine the consequences of the SC fault and their relation to the slot/pole (S/P) combinations: in the study analytical tools are adopted for the investigation of influence of the slot pole combination on the inter turn fault SC current and power density against the FTe of the case study set of machines is investigated.

- Design of non-conventional field wound flux switching machine: this study looks into a systematic design based on existing permanent magnet synchronous machine (PMSM) used for traction an application. For a given stator, the coils are altered and rotor is designed to maximise the torque. Since the field excitation is provided by external current source, it allows to de-excite the coils in case of the inter turn SC fault and also improves the power management during the field weakening operation compared to the traditional surface mounted permanent magnet machines (SM-PMSMs).

- Design validation trough experiments on the prototyped machine.

1.6 Novelty of the thesis

The key contributions included in the thesis are:

- Investigation of the FRM:

  The unconventional electrical machine topology which meets the FT criteria is modelled and tested where the trade-off involved between the FTe and the performance is addressed.

- Investigation of influences of different slot and pole combinations on the SC fault current and thus the FTe:

  For the performance prediction and fault investigation, a complete analytical model is employed whilst numerical tools are used to determine the thermal performance. The investigation highlights the compromise between the power to mass ratio and the fault tolerance in which the influence of the key design parameters and how they affect the fault current is demonstrated.

- Development of the enhanced FT field wound flux switching machine (FWFSM):

  To overcome the challenges related to the SC fault, the topology that eliminates the PM material and is based on the field winding excitation is developed. The challenges related to the high torque density are investigated and the key design factors influencing the performance are identified. The way of achieving high torque density for the considered topology is proposed. The design is carried out via FEA and validated through experiments.

1.7 Thesis outline

This thesis is divided in 7 chapters. These are as follows:

Chapter 2 aims to introduce the concept of the FRM, describe the basic principle of its operation and give an overview on the development of the FRM from the very first mention in literature to the latest modifications of the recent past.

Chapter 3 gives mathematical description of the FRM in the d–q reference frame and the concept of a fictitious magnetic gear is introduced. The process of validation of the parameters of the FRM that has been designed and built as a prove of concept explained. The models used to predict and verify the performance of the FRM presented are created in Matlab® Simulink® and Infolityca MagNet. These models are then compared with the results of experiments performed on the FRM.

Chapter 4 investigates the influence of the slot and pole combination in fault tolerant permanent magnet machines under a short circuit fault. A 2D sub-domain field computational model with the multi objective genetic algorithm (MOGA) is used for the design and performance prediction. During the post processing stage a 1D analysis is employed for the inter turn SC fault analysis.

Chapter 5 presents the idea of utilisation of the existing PMSM and performing its modification to transform it to the FWFSM, a magnet less machine to deliver cheaper machine with improved FT capability. The necessary modifications in the current stator are presented and the process of the optimal rotor design is fully described with the final design of the rotor optimised regarding the torque performance. Also the trade off between best performance and practicality of the solution is risen and the consequences are elaborated.

Chapter 6 presents the experimental rig that has been built for the experiments and tests performed on the FWFSM. The results obtained from the experiments on the FWFSM and comparison to the predictions based on the FEA and models of the FWFSM are provided. The experiments are divided to no load/no excitation and load tests, where each part contains set of experiments. Description of each experiment is provided, as well as comments on the results.

Chapter 7 concludes the thesis.

Chapter 2

Flux Reversal Machine

Aim of this chapter is to introduce the concept of the FRM, describe the basic principle of its operation and give an overview on the development of the FRM from the very first mention in literature to the latest modifications of the recent past. The customised modifications of the FRMs are organised into groups with common features. Also the hybrid parametric model of the machine used for analysis, design and geometry optimisation of the machine is introduced.

2.1 History and Technical Background

The FRMs gained a lot attention during last decades mainly due to their robust and simply rotor construction inherited from the switched reluctance machines (SRMs) and FT capabilities of stator topology of the PMSMs [21]. Typical for FRMs are the PMs placed on the surface, or inside of the stator teeth. The FRMs belong to the group of doubly salient permanent magnet machines (DSPMMs). Doubly salient, as both the stator and rotor are salient [21]. The first type of the DSPMM with PMs placed in stator was introduced back in 1955 in [22] as a promising topology for high frequency alternators. The topology of the DSPMMs is based on magnetic flux transferred from the PMs placed in the stator through the air gap to the rotor when the rotor poles face the stator teeth and is shown on the Fig. 2-1.

The FRMs got their name due to the flux reversing nature of the machine; the phase flux reverses with every electrical cycle of displacement of the rotor. It is evident from Fig. 2-1, depicting the cross section of the single phase DSPMM. In Fig. 2-1a the rotor is aligned with the pair of the stator

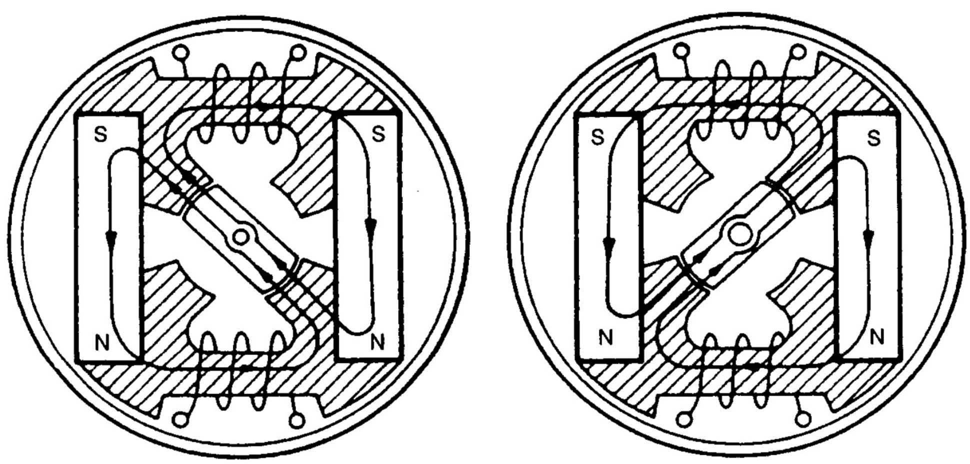

(a) Rotor alignment during first half of the electric cycle

(b) Rotor alignment during second half of the electric cycle

Fig. (2-1): Axial cross section of single phase DSPMM [22] teeth, while the Fig. 2-1b shows the situation after current alternation and consequent shift of the rotor to the second position. The Fig. 2-1a and Fig. 2-1b demonstrate, that as the rotor tooth moves along the stator pole pitch, the flux linked in the stator coils reverses [23].

Although the concept of the DSPMM was novel and improvement upon peak power and minimal volume alternator [22], the topology had also drawbacks such poor utilisation of available rotor volume, stator vibrations and a complicated stator topology which complicated for manufacturing [24, 25].

The FRM is not the only and first representative of the DSPMMs and different single phase [26] or three phase [27] machines were proposed, these machines produce unipolar flux and magneto motive force (MMF) variation, while the FRM produces bipolar flux and MMF variations [21, 25].

First type of the conventional FRM was introduced in 1996 in [24], along with FE analysis in [21]. The proposed machine had two pole stator and three pole rotor and is shown in Fig. 2-2. Surface of each of the stator teeth was equipped with pair of magnets of alternating polarity.

The single phase topology improved the performance dramatically compared to the DSPMMs in [22], but produced cogging torque was of a high level [25]. To reduce the cogging torque whilst maintaining the simplicity of the rotor design, a three phase FRM was proposed in [25, 21] and is shown

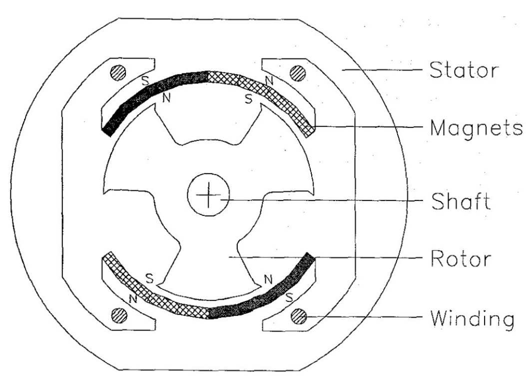

Fig. (2-2): Axial cross section of the single phase FRM [21].

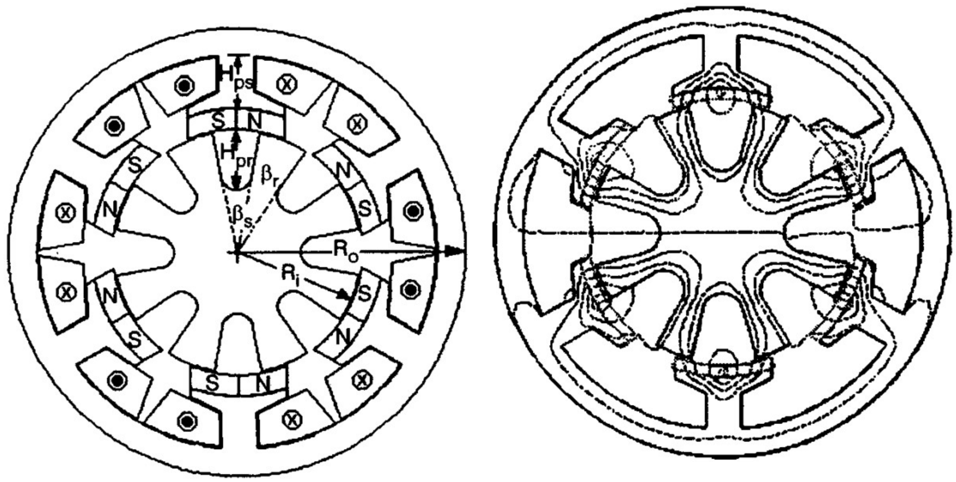

(a) Topology of the three phase FRM (b) Flux distribution in three phase FRM

Fig. (2-3): Axial cross section of the three phase, 6 slots, 8 poles FRM [25].

in Fig. 2-3. Main difference from the single phase FRM is increased number of stator and rotor poles, while the number of magnets per tooth remained the same, although the number of both stator slots and rotor poles can vary for multiphase configuration [25].

2.2 Principle of operation of the FRM

As the topology of the FRM is based on permanent magnet machines (PMMs) and SRMs, the principle of operation is related to both and can be demonstrated on the single phase FRM.

The paths taken by the magnetic flux during different rotor alignments will be discussed. These are shown in Fig. 2-4. In Fig. 2-4(a) the rotor is in equilibrium so the magnetic flux created by the PMs is circulating within individual stator pole.

In this position, there is not magnetic flux flowing through the stator back iron, hence no flux is linking any of the coils. If the rotor is displaced from the neutral position by 30° mechanical (ie. 90° electrical) counter clockwise to the position where two of the rotor poles are overlapping two of the stator magnets, the flux flows through the stator back iron between the two teeth, hence two coils are magnetically linked. In this position the magnetic flux reaches its maximum value, as is shown in Fig. 2-4(b). Another displacement of the rotor by 30° brings the rotor to the second neutral position and situation is similar to the situation in first position, but the electro motive force (EMF) has now reversed polarity, due to the reversed direction of change. At the final position, showed on Fig. 2-4(d) the rotor is displaced of another 30° and the rotor poles overlapping second pair of magnets, hence the flux is linked through the adjoining stator teeth in reverse direction against the case (a) and the rotor completes one electrical cycle.

The single phase FRM was chosen to demonstrate the principle of the

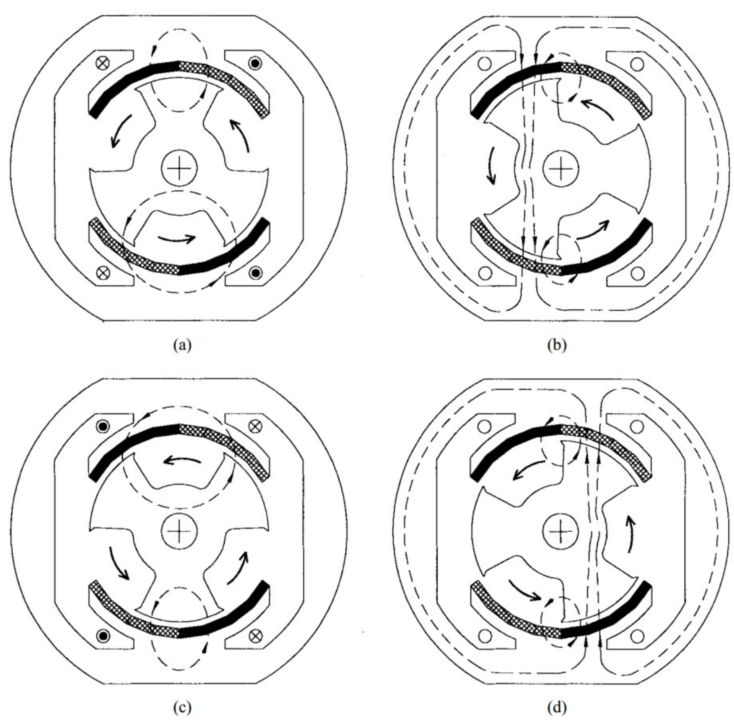

Fig. (2-4): Illustration of the principle of the operation of the FRM during one electric cycle [21] with rotor displacement of (a) 0° (b) 30° (c) 60° and (d) 90°.

operation because of its simplicity, but the description is applicable on multiphase topology as well.

2.3 Categorization of the FRMs

Many of the different design features adopted in other machine topologies can be applied to the FRMs. The most common of the applied design features are discussed in the following section.

2.3.1 Winding topologies

The most widely adopted winding topology for FRMs is the topology with three phase concentrated winding and magnets placed on the surface of the stator teeth [25, 28, 23, 29, 30, 31, 32, 33], an example of the concentrated winding topology is shown in Fig. 2-5.

Alternate winding topologies/configurations also exist, these being the full pitch [34, 35, 36] or fractional slot concentrated winding [37]. The main advantage of these alternate topologies is increased power density of the FRM [34, 35]. It was shown, that the FRM with full pitch concentrated winding delivers can lead to to higher output power as the FRM compare to the FRM utilising conventional concentrated winding and has a potetial to achieve about 13% better power density compared to a PMSM. However, the self inductance of such FRM is up to three times higher, is influenced by the saturation level of the machine and concludes in poor voltage regulation [34].

While the conventional FRM has number of rotor slots higher then number of stator slots, concept of the FRM with compensatory windings topology consisting of 12 stator slots and 10 rotor poles, shown on Fig. 2-6, is introduced in [39]. The ratio of stator and rotor poles, where each phase consist of

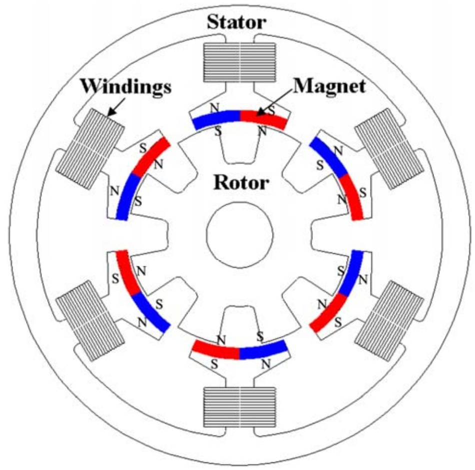

Fig. (2-5): Axial cross section of three phase FRM with double layer concentrated winding and surface mounted PMs [38].

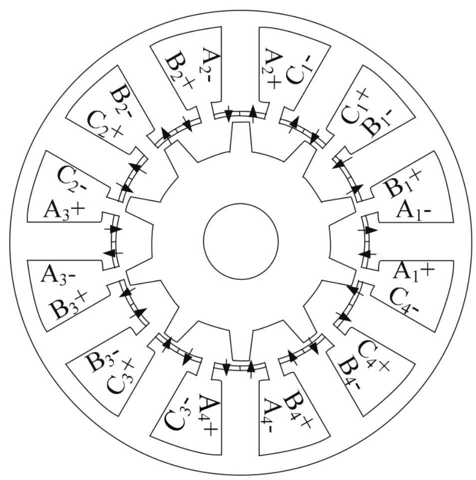

Fig. (2-6): Axial cross section of three phase FRM with compensatory windings [39].

four coils, creates compensatory effect, where harmonics of EMF in each pair of coils are mutually nullified. The positive outcome of this topology is reduced cogging torque at comparable electromagnetic performance compared to the conventional FRMs.

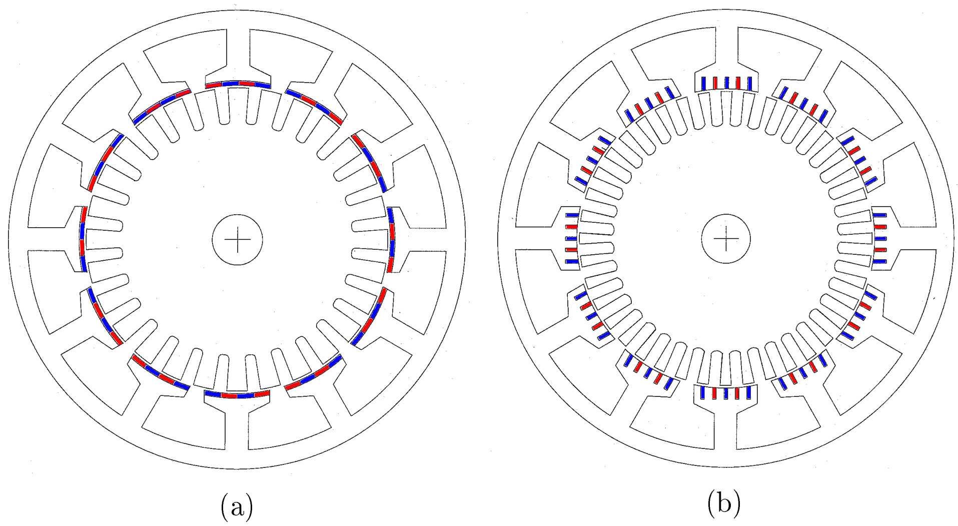

Fig. (2-7): Cross section of the three phase FRM with (a) Surface mounted PMs (b) Inset PMs

2.3.2 Placement of the PMs

A conventional type of FRM has PMs placed on the surface of the stator teeth (Fig. 2-7a). However, surface mounted magnets is not the only way of magnet's placement. Insetting the magnets in the stator tooth can reduce the cogging torque and air gap leakage flux [32, 40]. Because the PMs are placed in parallel to the magnetic flux path the risk of its demagnetisation is reduced. The proposed inset type FRM (Fig. 2-7b) was compared with the equivalent FRM, while inset type used 40% less magnet material, it achieved the same BEMF constant and lower iron losses than the surface mounted FRM.

In addition to the surface mounted or inset FRMs, [41] proposed concept of the consequent pole FRM, that in compare to the conventional FRM uses only half of the volume of magnets in compare to conventional FRM, it delivers 26% higher rated mean torque due to lower torque pulsation and ripple, with equivalent efficiency and weight.

The cross section of the consequent pole FRM is shown on Fig. 2-8.

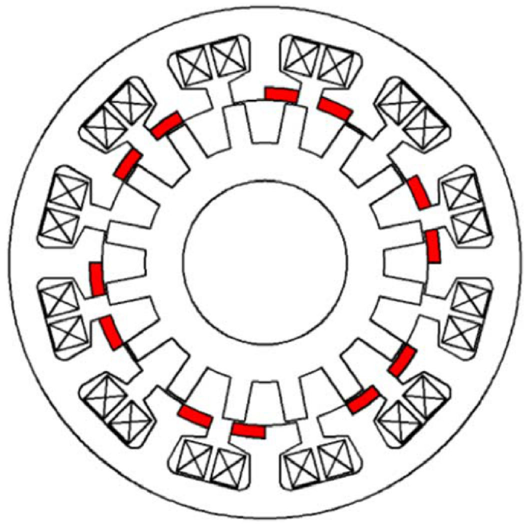

Fig. (2-8): Consequent pole FRM [41]

2.3.3 Width of the slot opening

As it has been presented earlier in subsection 2.3.1, most of FRMs mentioned in literature adapts the topology of a concentrated windings, the topologies utilising distributed windings are in minority. All of the discussed winding topologies were applied without affecting the stator geometry. However, concentrated winding can be used with two types of coils arrangement. With change of the coils' arrangement, modification of the width of the slot opening [33] is necessary. In [33], q - the number of slots per phase per pole and also determines the type of used winding. Hence slot opening with $q = 1$ considers alternated coils type and $q = 0.5$ indicates topology utilising consequent arrangement of the coils. Both topologies are shown on Fig. 2-9. The relation between q and slot opening width can be expressed as a number of omitted pairs of PMs between two adjoining stator teeth and is given as $0.5/q$. Therefore machines with $q = 1$, $q = 0.5$ respectively have the slot opening equal to one and two PMs respectively.

Consequently, the number of rotor slots (Nr) feasible for chosen stator

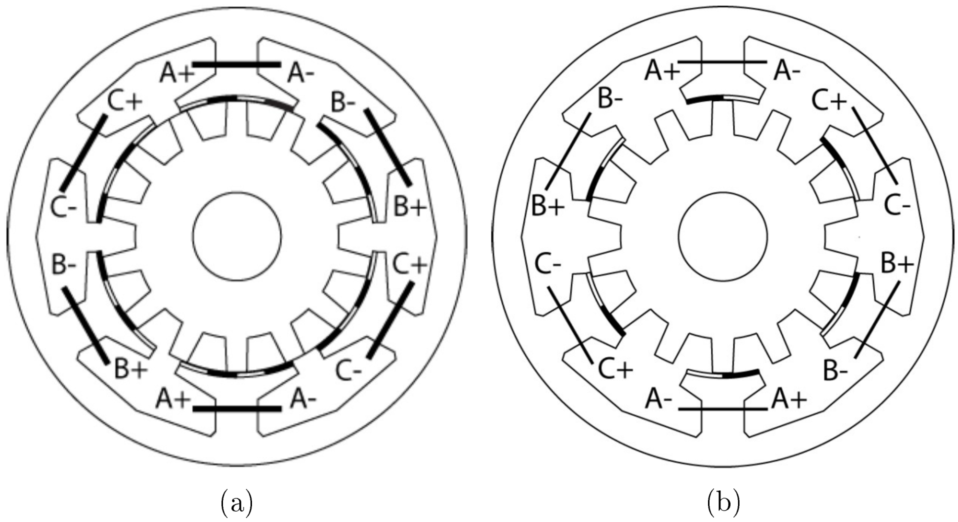

Fig. (2-9): Winding configurations of FRMs (a) $q = 1$ (b) $q = 0.5$

configuration can be identified from the following relationship:

$$N_r = p_m \pm p \tag{1}$$

Where p_m the represents total theoretical number of the PMs pairs, those on stator teeth and those omitted in between them and p is representing number of pole pairs of the spatial field distribution. As was declared earlier, the number of omitted PMs pairs is given as $0.5/q$ for both configurations so the equation (1) becomes:

$$N_r = \left(N_{pp} + \frac{0.5}{q} \right) \cdot N_s \pm \frac{N_s}{6q} \tag{2}$$

Where N_{pp} is number of PMs per stator tooth. The ratio between the number of rotor slots N_r and stator slots N_s can be expressed as:

$$\frac{N_r}{N_s} = \left(N_{pp} + \frac{0.5}{q} \right) \pm \frac{1}{6q} \tag{3}$$

Equation (3) shows direct relationship between number of PMs per stator tooth and number of rotor teeth N_r . For any stator of the FRM exist two feasible rotors due to the $\pm$ sign in the (2) and also the N_r is determined by the N_{pp} parameter. Author [33] used this relation to show feasible rotor configurations for machines with commonly used slot pole combinations.

2.3.4 The background of the FRM prototype design

Although the design of the FRM is not the subject of the thesis, the experimental part is based on it. Therefore it is important to introduce the model and process that was behind the final prototype parameters and identification of optimal geometrical dimensions.

The design process is very well and in detail described in [33], where the analysis described led to the final parameters of the prototype. The goal of the analysis was to design the FRM with the best performance possible in terms of the maximal shear stress and power factor. The dependencies of these two criteria on the main geometrical variables are investigated utilising a hybrid approach where the FEA and analytical model are used to determine the equivalent magnetic loading for different geometrical parameters of the machine using the parametric machine model. The FEA part of the analysis was used to determine B_0, the equivalent magnetic loading at no load. Its value is obtained using a virtual sensing coil around the tooth of the FRM and it measures the magnetic flux to estimate the equivalent magnetic loading B_{m0} assuming the case of the geometry of the stator with maximal possible tooth width of the linearised stator geometry. This approach is valid if the coil section is assumed to be represented as a linear instead of cylindrical and the PM pair pitch is assumed to be equal to the rotor slot pitch.

The outcome of the FEA is used as one of the inputs to the analytical model. The parameters that were varying through the parametrisation process are:

- Airgap thickness

- Height of the PM
- Number of PM pairs per tooth - n_{pp}

The results of the analysis show that the value of B_0 increases with the n_{pp} while increasing the height of the PM over certain extent causes reduction of B_0 and torque per ampere. The simulation gives also information that increasing thickness of the airgap and PM increase the core saturation limit, represented by electrical loading that saturates the stator core A_{sat}. The electrical loading is mainly determined by airgap length, PM thickness and stator tooth width. Combination of thick airgap and PM leads to a higher A_{sat}. On the other hand, the optimal ratio between thickness of PMs and airgap that led to optimal B_0 does not lead to an optimal shear stress value. Shear stress maximisation is important not only as as a main machine performance indicator, but also due to the conclusion, that the machine's power factor (PF) is maximal when the shear stress is maximal. The PF is estimated from the model's vector diagram, where it is equal to the angle between the vectors of flux linkage at load and no load. The PF of FRMs is low in general even for optimised geometric parameters of the machine. It can be influenced mainly via the ratio between the thickness of the PMs and airgap, like in the optimisation of the B_0. Also higher n_{pp} that leads to higher shear stress causes lower PF. Hence optimal number of PMs pairs per tooth compromise tends to be 2. The trade of between the performance and efficiency is evident also from another conclusion that the analysis gives, the larger width of the machines tooth, the larger A_{sat} bud reduced PF. These findings are based on the results of the parametric analyses that apart from these led to the optimal machine design parameters. The details regarding the geometry and other parameters of the FRM that was manufactured for experimental validation can be found in the table 3.2 presented in the next chapter.

2.4 Conclusion

This chapter describes the development of FRMs. The topology of FRMs gained a lot of attention in the literature for its robust rotor, high power density and small inductance variation with the rotor position. Many publications have sought some of the shortcomings of the FRM topology. The high torque ripple can be mitigated by skewing the rotor [25], the BEMF harmonics can be reduced using special combination of stator slots and rotor poles [39], the air gap leakage flux can be reduced using inset PMs [32, 40, 42], the power density and efficiency can be increased using the full pitch winding [30, 34, 35]. However, these are also the areas of performance of the FRMs that need to be improved and further research could be focused at. At the end of this chapter, a insight to the hybrid model of the FRM and the outcomes that this model provided are presented. Next chapter focuses on deeper introduction of the concrete FRM prototype and the experiments that were executed on the machine to confirm the FRM's model.

Chapter 3

Modelling and experiments on the FRM

In this chapter, mathematical description of the FRM in the d–q reference frame is presented and the concept of a fictitious magnetic gear is introduced. The process of validation of the parameters of the FRM is explained. The models used to predict and to verify the performance of the FRM presented are created in Matlab® Simulink® and Infolityca MagNet. These models are then compared with the results of experiments performed on the built prototype of the FRM as a proof of concept. The parameters of the prototype are also presented.

3.1 Mathematical description of the FRM in d-q coordinates

Mathematical description of FRM in the d–q reference frame is based on and very similar to the mathematical description of the conventional PMSM. Main difference is made by the fictitious electrical gear effect introduced in [35]. Mechanical speed of FRM is given as:

$$n = \frac{60 \cdot f}{n_r} \tag{1}$$

Where flux pattern speed n_f is defined as:

$$n_f = 60 \cdot f \tag{2}$$

Equations (1) and (2) show, that mechanical speed and flux pattern speed are different.

The mechanical speed is n_r times lower while at conventional machines these speeds are equal. This is called the fictitious magnetic gear effect and

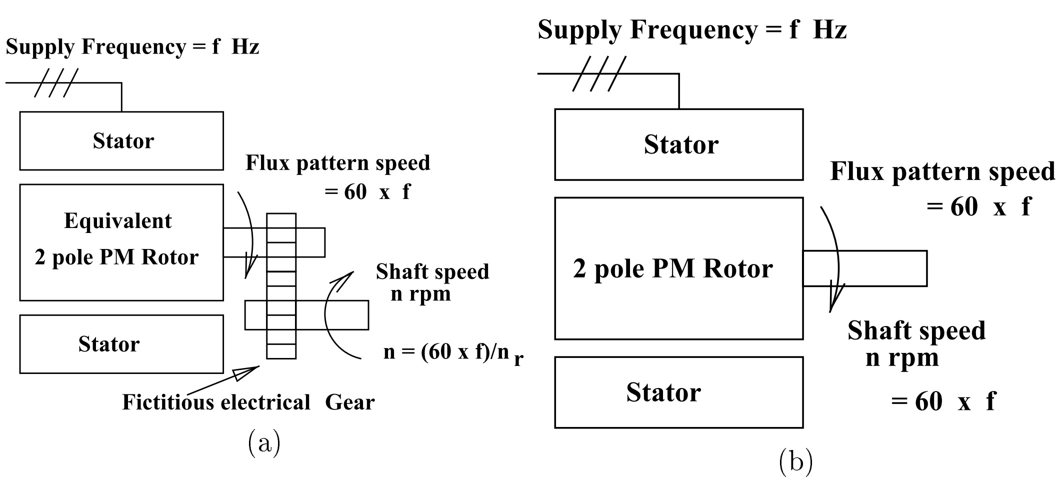

Fig. (3-1): Concept of the fictitious electric gear introduced to compare (a) FRM and (b) PMSM [35].

it can be expressed as:

$$K = \frac{n_r}{P_{eq}/2} \tag{3}$$

Where the P_{eq} is the number of the flux pattern poles. As has been stated earlier, this is the main difference between mathematical description of PMSM and FRM, and the difference can be visualised as shown on Fig. 3-1.

Hence the equivalent d–q circuits for FRM in direct and quadrature axis respectively correspond with Fig. 3-2 equivalent circuits.

To derive this circuit, following assumptions were made [35]:

- Saturation in the machine is negligible
- The induced EMF is of sinusoidal shape
- Eddy current and iron losses are negligible
- No field current dynamics
- There is no cage on the rotor

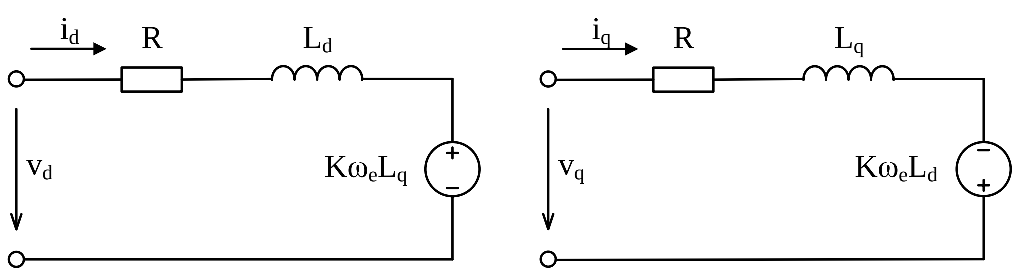

(a) (b)

Fig. (3-2): The d–q equivalent circuits of the FRM (a) d-axis (b) q-axis

These circuits can be then described by Kirchhoff's laws as follows:

$$v_d = Ri_d + \frac{d\lambda_d}{dt} - K\omega_e\lambda_q \tag{4}$$

$$v_q = Ri_q + \frac{d\lambda_q}{dt} + K\omega_e\lambda_d \tag{5}$$

$$\lambda_d = L_d i_d + \lambda_{PM} \tag{6}$$

$$\lambda_q = L_q i_q \tag{7}$$

Electrical equations are completed by electro-dynamical equation for torque:

$$T_e = \frac{3}{2}\frac{P_{eq}}{2}K\left[\lambda_{PM} i_q + (L_d - L_q)\cdot i_d i_q\right] \tag{8}$$

Due to fact, that d and q inductances are equal, equation (8) can be written as:

$$T_e = \frac{3}{2}\frac{P_{eq}}{2}K\lambda_{PM} i_q \tag{9}$$

According to the fact, that mathematical description of FRM is almost identical to the PMSM one, the control algorithm is also very similar to PMSM control.

The equations describing the FRM are the same of equations describing isotropic PMSM, hence the maximal torque per ampere is obtained while current $i_d = 0$. Therefore considered linear magnetic flux, the equations (4) - (7) will reduce to:

$$v_d = -K\omega_e\lambda_q \tag{10}$$

$$v_q = Ri_q + K\omega_e\lambda_d \tag{11}$$

$$\lambda_d = \lambda_{PM} \tag{12}$$

$$\lambda_q = L_q i_q \tag{13}$$

The equations references (4) - (13) gives simplified description of the FRM, but accurate enough for creating the model in Simulink for controller design.

3.2 Introduction to finite element modelling

The finite element method (FEM), or FEA, is a computational technique used to obtain approximate solutions of boundary value problems in engineering. It is useful for problems with complicated geometries, loadings, and material properties where it is too complicated or even impossible to obtain an analytical solution.

Originally, the FEA was used in aerospace industry for designing jet planes and similar, where accurate stress analysis for light weight structures were demanded. With the increase of computational power and decreasing costs of CPU time, it has become a standard development tool not only in aerospace, but in all kind of engineering areas, where the FEMs are used for structural, stress, fluid, electromagnetic or even acoustic and other analysis.

FEM consists of discretisation of the problem, therefore the model of the problem is divided into an equivalent system of many smaller units (finite elements) connected at points common to two or more elements and/or boundary lines and/or surfaces [43].

3.3 Finite element model of the FRM

To make the description of the creation of the FRM model easier to imagine, the parameters of the tested prototype are used. The summary of the prototype's parameters can be found in the Table 3.2.

To speed up the modelling process, first step in creation of the model is to find a mirror symmetry hence the model can be as small as possible and therefore with the same amount of elements the mesh can be smoother. If only part of the machine is to be modelled, appropriate boundary conditions have to be applied to reflect the symmetry.

In the case of the FRM, the main features, that decided the geometry is number of stator slots ($N_s = 12$), number of rotor teeth ($n_r = 28$) and number of phases ($m = 3$). Therefore the greatest common divisor of the number of slots n_r and number of teeth n_s is 4. This means that only one quarter of the machine is enough to obtain representative results. The number of phases is important as the model has to represent all the parts of the machine, hence all three phases.

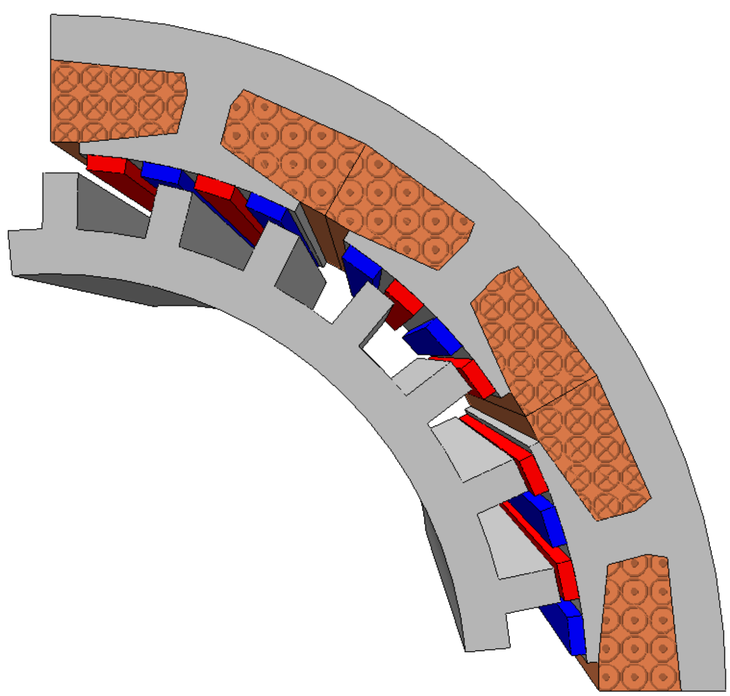

Fig. (3-3): Cross section of the FRM with the rotor aligned to the quadrature axis

It is also worth noted, that if only part of the machine is modelled, the results of the simulations will be scaled down accordingly to the ratio of the machine modelled. For example if only one quarter of the machine is modelled and simulated using transient with motion solver, the torque calculated will be representing only the quarter simulated and hence the actual torque produced by whole machine is actually four times higher than the results of the simulation shows. In this thesis, this is taken into account and so all the results representing the performance of the complete machine.

The model of the FRM is presented on Fig. 3-3 while the Fig. 3-4 shows the model with boundary conditions applied on the boundary surfaces. The boundaries have to be specified for all outer surfaces of the model. As the simulation of the model requires rotational motion, during the rotation of the rotor becomes the surface of the air gap, separating the rotor and the stator, also exposed.

Hence the boundary condition has to be applied on the air gap surface as well. The boundary condition applied here on the air gap surface can be either of an odd or an even type. The type of the periodicity corresponds to the pattern of the alternation of excitations between repeating sections. The type of periodicity is different for other FRMs, depending on m, N_r and N_s and leads to either even periodic or an odd periodic boundary condition. If the the excitations do not alternate from one repeating section to adjoining one, even periodic boundary can be used. On the contrary, if the excitations alternate from one repeating section to the adjoining one, the odd periodic boundary is to be used.

As in the modelled FRM the direction of the excitation in the repeating sections of the machine alternates in compare to the adjoining one, the odd periodic type of a boundary condition is used.

The materials assigned to the individual parts of the model are summarised in the Table 3.1. Together with the material assignment can be set up the size of the mesh elements. The size of the mesh can seriously affect not only validity of the model and hence the accuracy of the results, but it can also cause prolongs and longer the simulation times. Therefore the fine mesh should be defined only on the parts of the model, that is important for the result of the outcome of simulation (air gap in case of motion component) or parts that are of closer interest (edges of the stator teeth).

Part	Material
Stator laminations	M-36 24 Ga
Windings	Copper: C10700
Magnets	Neodymium Iron Boron: 38/23 ($Nd_2Fe_{14}B$)
Rotor laminations	M-36 24 Ga

Table (3.1): Materials assigned to the parts of the FRM model

Once the materials are assigned to the model parts, the magnetisation

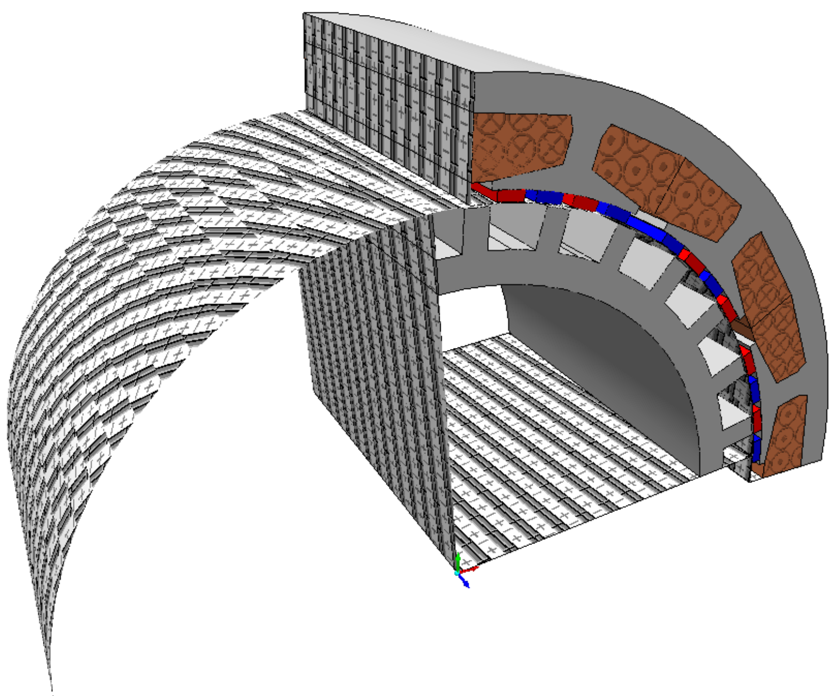

Fig. (3-4): Cross section of the FRM machine with boundary conditions present direction must be set, to achieve correct function of the model. Next step is to set up coils and windings. In this case, thanks to the symmetry, there is only one coil per phase modelled. As the machine was designed with a stress on FTe, each phase is formed of four coils in case of operation as a three phase machine, or two coils per phase in case of operation as a six phase machine. In both cases are the phase windings connected in star connection. Therefore in the event of a fault, one set of windings can be disconnected and the machine can maintain the function utilising only half the slots (three phase operation using half the number of slots).

The main parameters of the coils are number of turns and fill factor. The fill factor can be calculated automatically based on number of turns and wire diameter, or can be set manually through the material properties. The second option is more favourable as in case of scripted modification of the machine parameters in case of optimisation, the fill factor will remain the same, even the number of turns of the coil will change. Unlikely in the first case, with every modification of the number of turns, the wire cross section must be changed as well.

Together with the coils set up, the current sources can be connected through the circuit window. Example for the three phase windings connected in the star connection is shown on Fig. 3-5.

As the model is meant to be used to simulate transient with motion, the motion component needs to be set up. This means that all the parts of the rotor has to be selected (including air and boundaries rotor related). Once the motion component is created, it is important to set its offset. Aligning the rotor with the quadrature axis of the machine means that amplitude of the phase A current is also the i_q current while the i_d is effectively zero. On the Fig. 3-3 is the rotor already aligned with the quadrature axis. It is necessary to highlight that with every change of the speed of the motion component

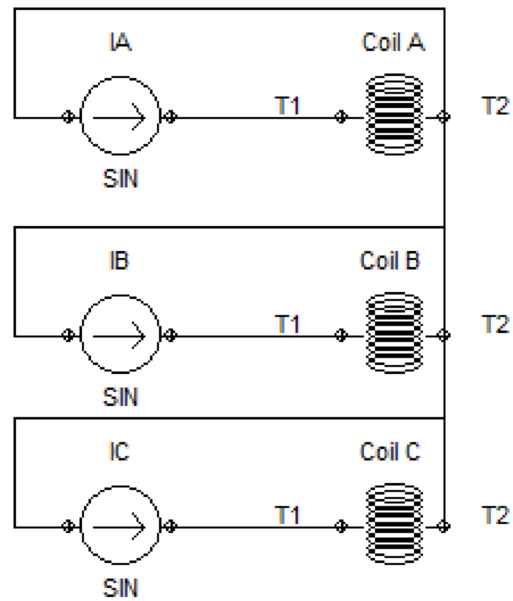

Fig. (3-5): Connection of the windings and current sources

also other parameters of the simulation must be changed, such a eventual frequencies of the current sources, the length of the simulation, simulation step and so on. Of course this depends on concrete purpose of the simulation. For this purposes, I have developed complex script in Matlab, that can be run and change all the needed parameters according to the settings of the simulation. This automation not only save time and speed up the reporting and results evaluations and post processing, but removes chance of mistakes creation as it lowers the input needed to the minimum.

3.4 FEA results

In this section, the simulation results are presented and discussed. Selected situations are then compared with the experiment results.

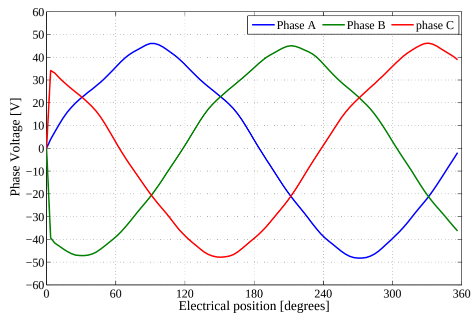

(a) One electrical cycle of three three phase BEMF for speed 1000rpm

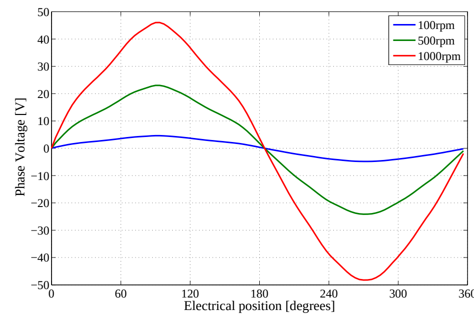

(b) One electrical cycle of the single phase BEMF for variable speeds

Fig. (3-6): No load BEMF waveforms for FRM

3.4.1 No load simulations

The Fig. 3-6a shows results of the no load test. This is usually first type of simulation that is performed, as it is on first sight obvious if the machine model is performing as expected or not. From the Fig. 3-6a is obvious that the three phase induced BEMF is right order and balanced.

The Fig. 3-6b presenting induced BEMF in phase A and compares them for different speeds.

The no load flux linkage shown on the Fig. 3-7a proves that the FRM is capable of generating the smooth sinusoidal flux linkage. One instant of the no load simulation is captured on the Fig. 3-7b where is shown the zero flux linked with the coil A while all the flux is flowing through the rotor back iron, across the air gap and through the both phase teeth. The leakage flux caused by the magnets on the phase A tooth tip can be also observed.

Fig. 3-8 gives first look on the simulation compared with the results of the no load test performed on the FRM. It compares single phase BEMF at speed 100rpm. Although the waves do not match perfectly, the experiment confirms the validity of the model.

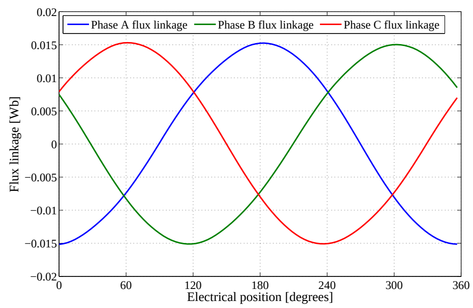

(a) No load flux linkage for one electrical cycle

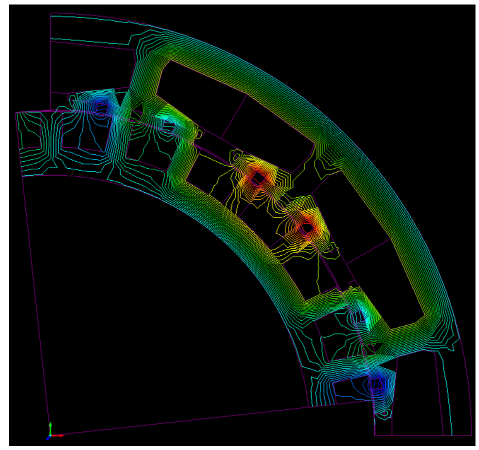

(b) No load flux linkage distribution at 100rpm

Fig. (3-7)

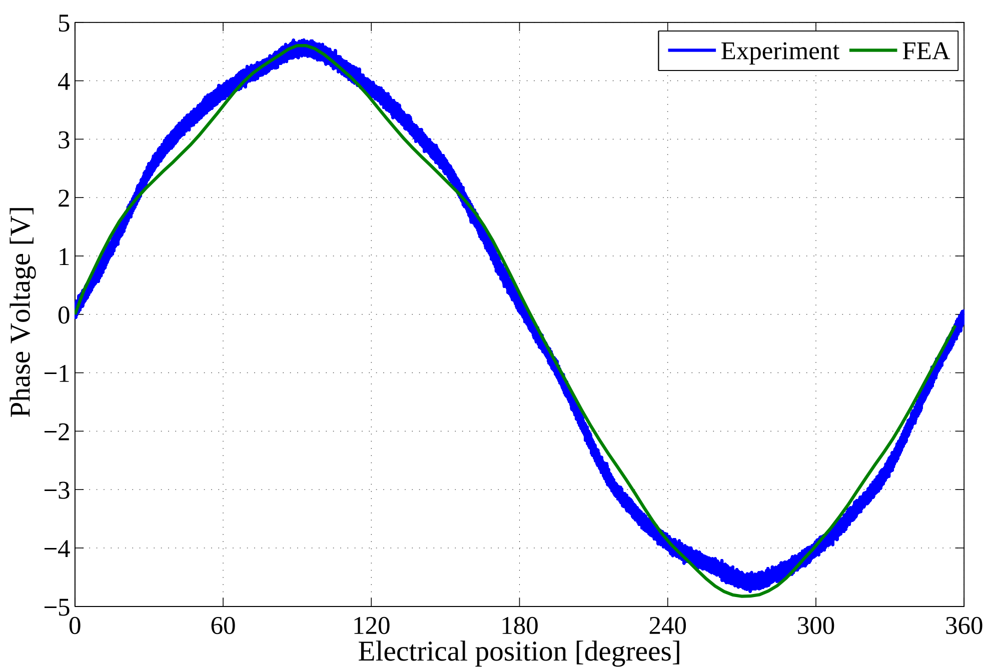

Fig. (3-8): Comparision of BEMF obtained via FEA and from experiment at 100rpm

3.4.2 Load tests

The simulation, when the referenced current of more then four times higher then is the rated current, was performed to confirm the assumption that the capability to remain in linear region even in case double the nominal current is applied.

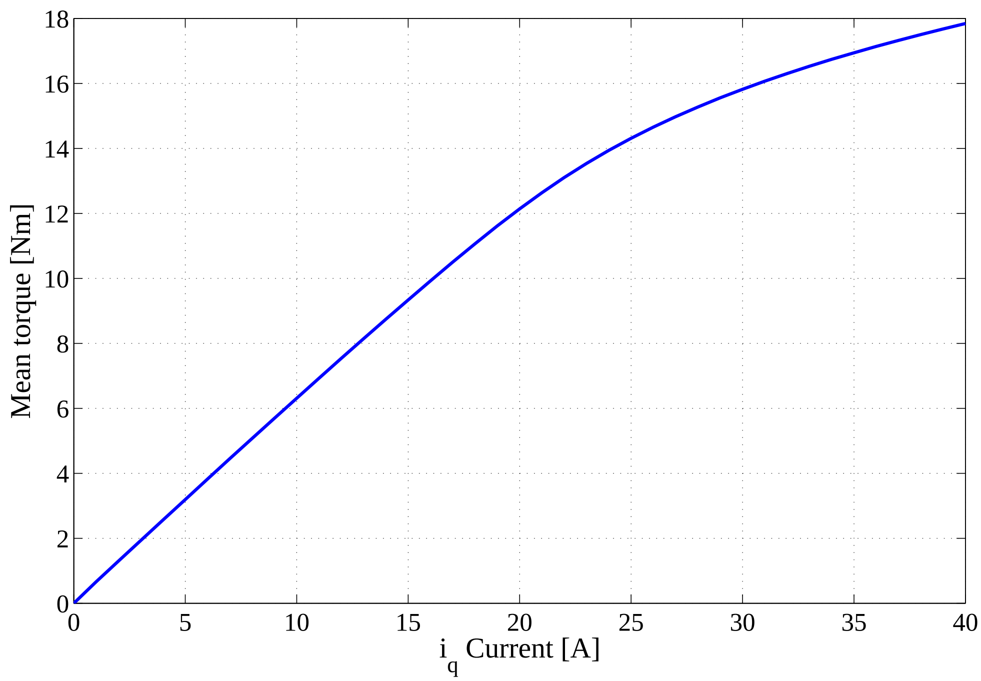

Fig. (3-9): Saturation of the FRM with increasing i_q, FEA evaluated

3.5 Parameters of the FRM

Parameter	Value
Rated current	$10A$ $(peak - peak)$
Rated Voltage	$280V(dc - link)$
Number of turns per coil	23
Rated speed	$1000rpm$
Continuous torque	$12Nm$
Power factor	0.55
Rotor OR	$46mm$
Rotor IR	$38.95mm$
Stator OR	$60mm$
Stack length	$50mm$
Rotor slots	28
Stator slots	12
Number of PMs	48
Magnet height	$1.36mm$
Magnet pitch	0.7
Connection	Star

Table (3.2): Parameters of the FRM

Parameter	Value
Rated current	$5.78A_{rms}$
Peak current	$10.53A_{rms}$
Rated voltage	$187V_{rms}$
Rated power	$1.65kW$
Power Factor	0.91
Rated speed	$4000rpm$
Continuous torque	$4.3Nm$
Peak torque	$7.46Nm$
Torque constant	$0.75Nm/A$

Table (3.3): Parameters of the Ultract 2 - PMSM used as a load during the experiments

3.6 Experiments

3.6.1 The FRM's test rig

The test rig that was used for the experiments on the FRM can be divided in two parts. The part of the FRM and part of the loading PMSM. To control the FRM, custom made inverter fed from rectifier was used, while the control was maintained using the dSpace platform.

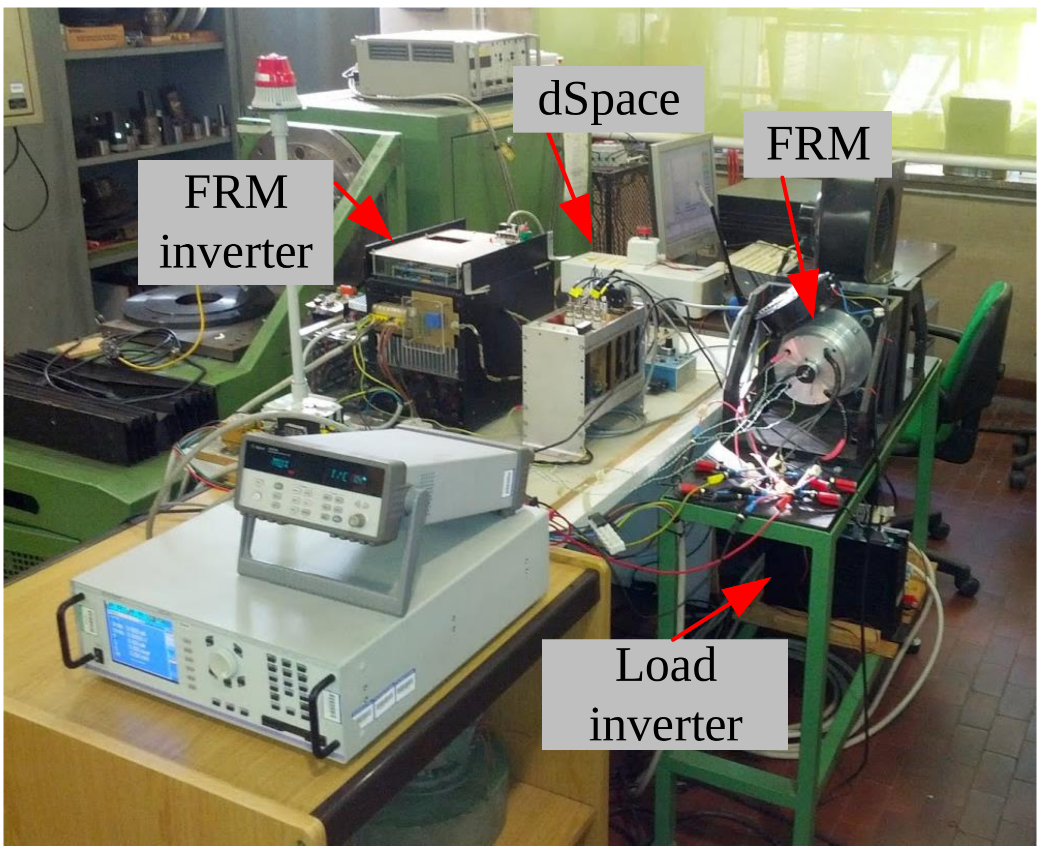

Fig. (3-10): FRM test rig at the lab of Politecnico di Torino

3.6.2 Torque evaluation

Due to the fact that the test rig was not fitted with an torque-meter, the torque could not be measured directly, hence indirect method to estimate

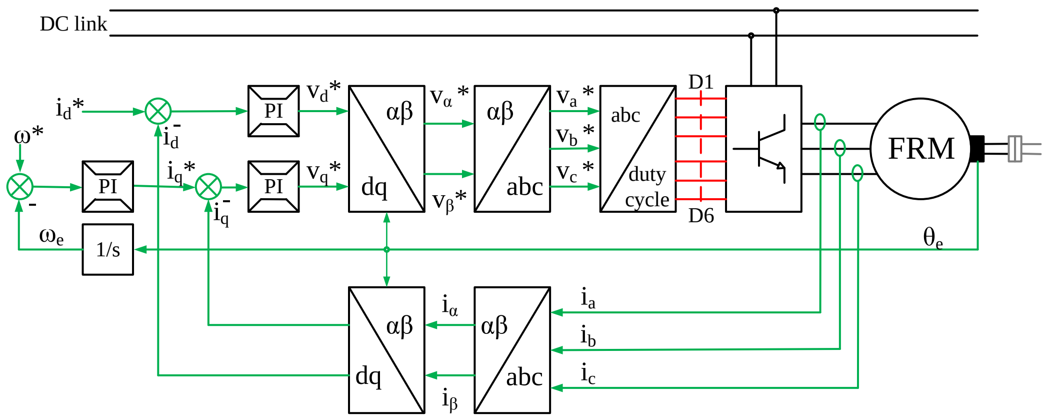

Fig. (3-11): the diagram of control topology used with the FRM test rig

the torque had to be applied. This method is so called ”wave test” and is well described in [44].

The method used to evaluate the torque consists of consequent application of positive and negative current in q axis, while measuring active power during both, motoring and breaking operations. Due to possible variation of copper and magnet losses during the test procedure, the test should be done in shortest time intervals as possible, however the test for each regime must last long enough to allow speed settling and accurate power reading. To minimise the influence of changing winding resistance, the procedure consisted of three steps, where the FRM has undergone motoring, breaking and motoring load again. The reason for three repetitions is that averaging active power measured during first and third step (motoring regimes) leads to

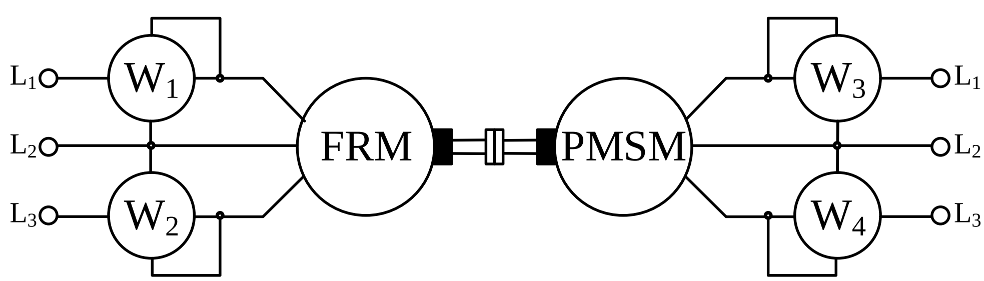

Fig. (3-12): Power measurement during the wave test using four watt meters

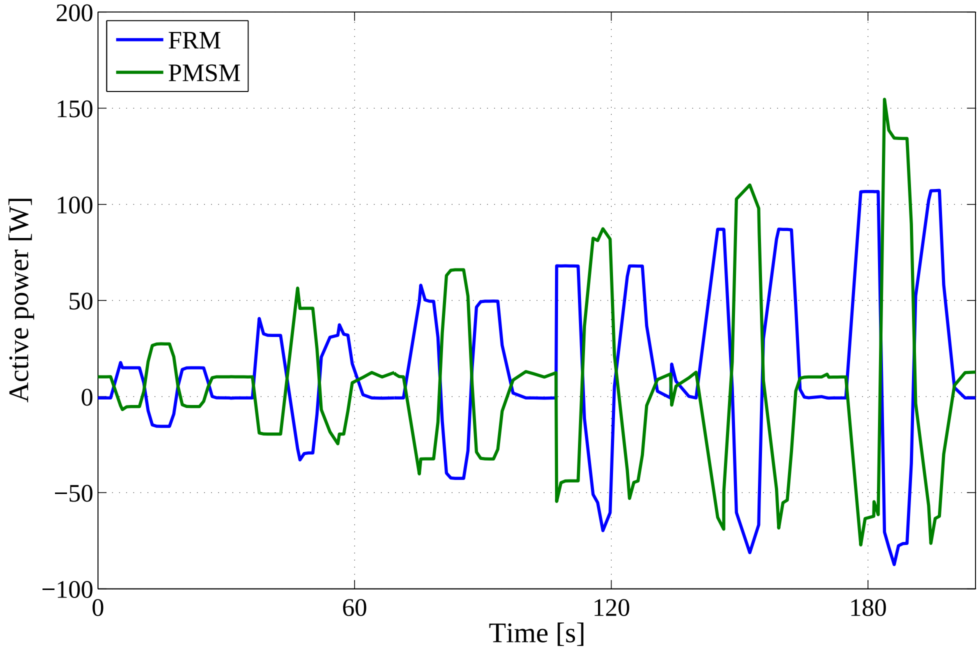

Fig. (3-13): Wave test for $i_q = 1 - 6A$.

power reading obtained under equal thermal conditions as the measurement during second step (breaking regime).

In other words, if the winding temperature changed during the three steps, averaged results from first and third measurement can be considered as measured under the same thermal conditions as results obtained during the second (middle) step. To achieve higher accuracy, the whole process was automated and each of the three steps took 15 second. The time was chosen to allow speed control to react on step change of the load and the current transient subsided while it was not too long to minimise increase of temperature. The measured values are shown on the Fig. 3-13.

Example of the evaluation of mean torque of the FRM for the first row of the Table 3.5:

$$P_{AvrMot} = \frac{P_{mot1} + P_{mot2}}{2} = \frac{14.97W + 14.95W}{2} = 14.96W \qquad (14)$$

	$P_{FRM}[W]$			$P_{PMSM}[W]$		
$I_q[A]$	Mot_1	Gen	Mot_2	Gen_1	Mot	Gen_2
1	14.97	-15.49	14.95	-5.33	27.41	-5.22
2	36.86	-29.66	32.38	-19.53	45.91	-19.59
3	50.28	-42.57	49.56	-32.44	65.68	-32.42
4	67.97	-60.41	67.96	-43.94	82.40	-44.73
5	87.04	-68.00	86.93	-55.23	97.94	-55.29
6	106.6	-77.59	107.0	-62.27	134.40	-63.46

Table (3.4): Active power measured during the wave test for $i_q = 1A \div 7A$ and $\omega_{mech} = 30rad/s$.

$$P_{FRM} = \frac{|P_{AvrMot}| + |P_{AvrGen}|}{2} = \frac{|14.96W| + |-15.49W|}{2} = 15.23W \quad (15)$$

$$T_{FRM} = \frac{P_{FRM}}{\omega_{mech}} = \frac{15.23W}{30rad/s} = \underline{\underline{0.51Nm}} \quad (16)$$

From the visualisation of the results of the torque estimation is evident, that using proposed method to evaluate mean torque of the machine can be obtained accurate results, as the evaluated torque is not only in close match with the FEA, but also control evaluation of the torque from the other, PMSM side are in agreement with found values.

	$P[W]$		$P[W]$		$Torque[Nm]$		
$I_q[A]$	FRM_{mot}	$PMSM_{gen}$	P_{FRM}	P_{PMSM}	FRM	$PMSM$	FEA
1	14.96	-5.27	15.23	16.34	0.51	0.54	0.55
2	34.62	-19.53	32.14	32.72	1.07	1.09	1.08
3	49.92	-32.43	46.24	49.05	1.54	1.63	1.60
4	67.96	-44.32	64.19	63.36	2.13	2.11	2.13
5	86.98	-55.23	77.49	76.58	2.58	2.55	2.65
6	106.81	-62.84	92.22	98.64	3.07	3.28	3.17

Table (3.5): Quantities evaluated from measured values obtained from the wave test.

If the torque meter would be present, the process of obtaining results would be much faster and more accurate. Also described method does not allow to obtain instantaneous torque values, hence it could not be used to evaluation of real time cogging torque and torque ripple values.

As it has been shown that the FE model is trust worth, it can be assumed that the machine is capable to achieve simulated states. Hence the continuous torque 12Nm can be handled and according to the mass of the PM material in used in the machine, the torque density can be estimated, considering the weight of the PMs used to the level of continuous torque. The machine accommodates 110g of PMs hence it achieves torque density of 110Nm/kg of PMs.

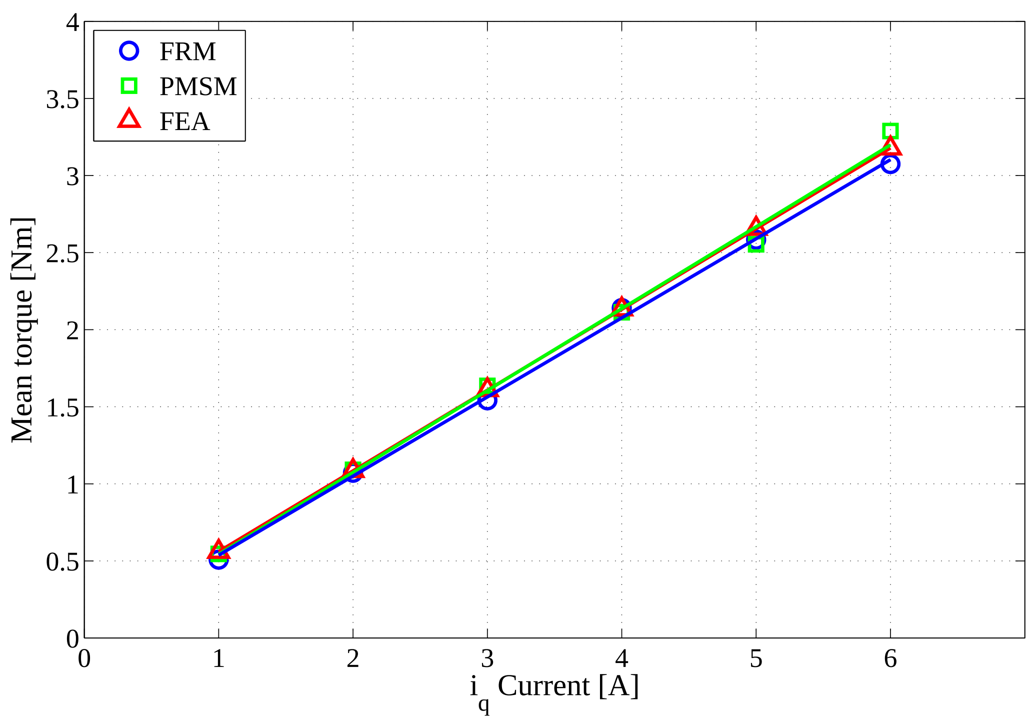

Fig. (3-14): Comparison of mean torques obtained through experiment and FEA.

3.7 Conclusion

The mathematical description of the FRM in the d–q reference frame was introduced in this chapter. Also the magnetic gearing effect was introduced, to make the FRM comparable and compatible with the PMSM and its mathematical description. The results of the no load and load simulations and experiments were presented, compared and their match was highlighted. Although due to the rig limitations, the full capability of the FRM could not be fully tested and proved, the results obtained with lower load still confirms the assumptions and shows the credibility of the model. The FRM proved itself as a machine that can be considered for specific applications, where decent level of the FTe is required. Although the FRM can be considered as a machine with decent level of FT capability, the fact that it utilises PMs brings the issue, that in case of SC fault the winding could suffer form high SC fault current and caused serious damage. Therefore next chapter is investigating the dangers of the inter turn SC faults in PM machines.

Chapter 4

Inter Turn SC Fault

The investigation on the influence of the slot and pole combination in fault tolerant permanent magnet machines under an inter turn short circuit fault is carried out through this chapter. A 2D sub-domain field computational model with MOGA is used for the design and performance prediction. During the post processing stage a 1D analysis is employed for fault analysis.

4.1 Introduction

In previous chapter, it has been shown that the torque density improvements can be achieved also through reduced amount of PM material and adopting unconventional machine topology. However the fault tolerance is still an issue due to magnetic field generated by PM which cannot be removed at event of failure. Generally, several design adaptation are included within the design in order to address this issue. This allows the machine to fail safely, without any catastrophic damage and also enable the machine to maintain the same or comparable performance under fault to that when the machine was healthy.

The most commonly implemented method of fault tolerance is redundancy [17]. However adding redundancy increases the system weight, volume and cost. In systems where $N + 1$ redundancy cannot be achieved due to these constraints, alternative FT features must be considered [18]. There are a number of FT features which can be included in PM machine designs which increase the availability of the machine without adding redundancy and its associated weight, volume and cost. [18, 19, 20].
These are:

1. Use of the concentrated single layer windings which allow the phase windings to be separated physically and magnetically as shown in Fig. 4-1.

2. Overrating of the phase inductance, limits the phase SC current to a safe value in the case of winding short circuit fault.

3. Designing the machine that is capable to withstand increased current loading to deliver the rated output power during a fault, enabling continuous operation.

Although the above mentioned features improve the fault tolerance of the machine, they also reduce the torque density of the machine. However, a design using these features has an advantage over a system using redundancy in terms of weight, volume and cost as the system is not duplicated.

The key fault in such FT design is inter-turn SC fault that cannot be completely mitigated due to the permanent magnetic field. During inter-turn SC fault, post-fault control methods are often adopted to minimize the fault current [28, 45, 46]. The most common post-fault control method involves shorting the machine terminals [46]. This method is easy to implement via a converter without the need of any additional hardware. However, this method requires large winding inductances so that the SC current is limited to a safe value. In general, designs with 1pu phase inductance are preferred solutions to limit the SC current [18].

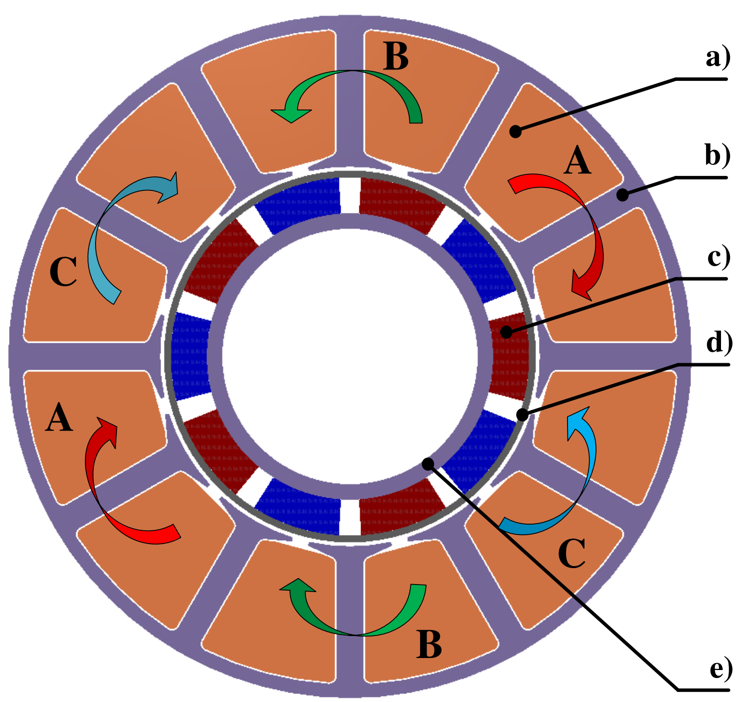

Fig. (4-1): Cross section of a fault tolerant - permanent magnet (FT-PM) machine with single layer concentrated winding: a) coil face of phase A b) stator core iron c) PM d) rotor sleeve e) rotor core iron

The analysis will show that a single turn-turn (an inter-turn) fault is still problematic, because the fault current mainly depends on the turn inductance which depends on the location of the fault in the slot. More importantly, an inter-turn fault, occurring close to the slot opening region, experiences a high SC current due to its low inductance [19, 47].

The influence of the S/P combination on the inter-turn SC fault in a fault tolerant permanent magnet (FT-PM) machine is therefore investigated. The study considers applications where it is safe to short the terminals of the machine windings as part of the post-fault control. Using analytical tools, a set of machines with different S/P combinations are studied. A 2D sub-domain field computational model with MOGA is used for design and performance prediction of the studied machines, where the electromagnetic losses including iron, magnet and winding losses are systematically calculated. A 1D analysis is employed for turn-turn fault prediction by calculating the self and mutual inductances of both the faulty and healthy turns during aSC fault condition with respect to the fault locations and thus fault current. The obtained results show that the SC fault current is highly influenced not only by the position in the slot where the inter-turn fault occurs, but also by the selected slot and pole number. It has been shown that the inter-turn fault current becomes significant with high pole numbers machines.

4.2 Inter-turn SC fault

Because FT-PM machines have alternate tooth wound concentrated windings that provide magnetic isolation between phases, mutual coupling is negligibly small [48]. Thus, the electrical circuit representing the phase winding during a turn-turn SC fault can be described using the differential equations (1) and (2) that represent the healthy turns and the faulty turns respectively.

$$V_1(t) = I_1(t)R_h + L_h\frac{dI_1}{dt} + L_m\frac{dI_s}{dt} + e_1(t) \tag{1}$$

$$0 = I_s(t)R_s + L_s\frac{dI_s}{dt} + L_m\frac{dI_1}{dt} + e_2(t) \tag{2}$$

where:

e_1: electro motive force in the healthy turns;

e_2: electro motive force in the shorted turns;

I_1: phase current induced in the shorted turns;

I_s: SC fault current;

L_h: self-inductance of the healthy turns;

L_s: self-inductance of the shorted turns;

L_m: mutual inductance between the healthy and the shorted turns;

R_h: resistance of the healthy turns;

R_s: resistance of the shorted turns;

Hence, the steady-stateSC fault current (I_s), after the machine has been shorted via the converter terminals, can be estimated using the following equation:

$$\begin{aligned} I_s = &\frac{j\omega_e L_m}{R_s R_h + {\omega_e}^2\left({L_m}^2 - L_s L_h\right) + j\omega_e (R_h L_s + R_s L_h)} e_1 - \\ &\frac{j\omega_e L_h + R_h}{R_s R_h + {\omega_e}^2\left({L_m}^2 - L_s L_h\right) + j\omega_e (R_h L_s + R_s L_h)} e_2 \end{aligned} \tag{3}$$

where ω_e is the angular electrical pulsation. From (3), it can be seen that I_s is related to three major parameters which are resistances R_s and R_h, inductances L_h, L_s and L_m and operational frequencies.

For clarity, terms in (3) can be substituted as follows:

$$\begin{cases} a = {L_m}^2 - L_s L_h \\ b = R_h L_s + R_s L_h \\ c = R_s R_h \end{cases} \tag{4}$$

With electro motive forces expressed as

$$\begin{cases} e_1 = \omega_e \varphi N_h \\ e_2 = \omega_e \varphi N_s \end{cases} \tag{5}$$

where N_h and N_s is number of healthy and shorted turns respectively. Substituting (4) and (5) into (3) yields

$$\begin{aligned} I_s = \frac{jL_m\omega_e}{a{\omega_e}^2 + b\omega_e \ + \ c}\omega_e\varphi N_h - \\ \frac{jL_h\omega_e + \ R_h}{a{\omega_e}^2 + b\omega_e \ + \ c}\omega_e\varphi N_s \end{aligned} \tag{6}$$

where, φ represents the non-load flux linkage per turn. Dividing numerator and denominator of (6) by ${\omega_e}^2$ yields

$$I_s = \frac{jL_m\varphi N_h - \ jL_h\varphi N_s - \varphi N_s \dfrac{R_h}{\omega_e}}{a + j\dfrac{b}{\omega_e} \ + \ \dfrac{c}{{\omega_e}^2}} \tag{7}$$

as ω_e is significantly greater than b, c and R_h, (7) can be simplified to:

$$I_s = \frac{jL_m\varphi N_h}{a} - \ \frac{jL_h\varphi N_s}{a} \tag{8}$$

For considered single turn-turn fault condition the $N_s = 1$, therefore the second term of (8) can be neglected:

$$I_s = \frac{jL_m\varphi N_h}{a} \tag{9}$$

Substituting the original term for a from (4) into (9) yields

$$I_s = \frac{jL_m \varphi N_h}{{L_m}^2 - L_s L_h} = \frac{j\varphi N_h}{L_m - \dfrac{L_s L_h}{L_m}} \tag{10}$$

As the second term of the denominator $\frac{L_s L_h}{L_m}$ in (10) is significantly smaller compared to the first term of the denominator L_m, it can be neglected and the equation can be expressed as:

$$I_s = \frac{j\varphi N_h}{L_m} \tag{11}$$

From (11), it is evident that the steady state SC fault current I_s is proportional to the number of turns and inversely proportional to the mutual inductances between healthy and faulty turns. As with increasing pole number both the number of turns per slot and mutual inductance between the healthy and faulty turns reduce, it is not evident how the S/P combination influences the SC fault current. Therefore detailed analyses has to be performed to draw such conclusion.

4.3 Selection of the Slot/Pole Combination

For design simplification, SM-PMSM is considered within this study. This allows using the analytical tool developed in house and consequently reduces the computational time involved during the optimisation process of different slot and pole design variants. The analysis are based on complete analytical model in which a 2D sub-domain field computational model is coupled with multi objective genetic algorithm (GA) to obtain an optimised design for given slot and pole number. The machine electromagnetic losses including iron, magnet and winding losses are systematically computed at post processing stage. Based on winding parameters evaluated at post processing stage, fault current associated to the fault in accordance with its fault locations are estimated using a 1D model.

For the slot and pole selection, alternate tooth wound concentrated winding topologies are considered due to the physical and magnetic isolation between the phases [49, 50]. Due to the inherent FT capability, a number of FT-PM machines with different S/P combinations are selected for the ensuing studies. In total, eight S/P combinations have been considered for this study, specifically: 6/4, 12/8, 12/10, 12/14, 18/12, 24/16, 24/20 and 24/28. The design specifications, together with the considered design variables are presented in the Table 4.1. The aim of the selection of S/P combinations is to compare reasonable number of S/P cases to obtain set of data that will provide insight into the influence of S/P combination onSC fault current. The slot number is selected as multiple of six (12, 18, 24) in a way to ac-

Table (4.1): Design Requirements of the FT-PM Machine

Parameter	Value
Stator outer diameter (OD)	120mm
Rated speed	2000rpm
DC link voltage	270V
Phase self-inductance	1pu
Rated torque	10Nm
Split ratio (SR)	Variable
Tooth-width ratio (TR)	Variable
Axial length (l_{stk})	Variable
Aspect ratio (AR)	l_{stk}/OD
Slot opening (So)	Variable
Tooth height (h_t)	Variable
Magnet height (h_m)	Variable
Number of turns per slot (N_t)	Variable
Phase current (I_p)	Variable

commodate three phase windings and alternate tooth winding arrangements. For slot number selected, a number of pole combinations could be considered. In this paper, a number of poles for each slot configuration has been considered to investigate the characteristics of the particular machine designs during fault. The selected S/P combinations, though, not exhaustive, are considered to be significant enough to demonstrate such influence.

4.4 FT-PM machine modelling

Fig. 4-2 represents the process involved in optimisation of the electrical machine design and both the performance and turn-turnSC fault analysis of the optimised design. The optimisation process starts with initially selected S/P combinations in section 4.3 and the fixed outer diameter (OD) of 120mm which is limited by envelope of the target application. Other design variables such as split ratio (SR), aspect ratio (AR), tooth width to slot ratio (TR), slot-opening (So), tooth-tip height (h_t), magnet span (α_m), magnet height (h_m), number of turns per slot (N_t) and phase current (I_p) are set as variable parameters.

The design process is limited by three design constraints which are:

1. A maximum no-load air gap flux density of 0.9T.

2. Phase winding inductances are overrated to have 1pu inductance in order to limit the phase SC current equivalent to rated phase current of the design.

3. DC Link voltage limit of the converter is fixed to ±135V.

The key design optimisation target is to produce high efficient and high mass density PM machines while satisfying the above mentioned constraints and application requirements given in Table 4.1. A multi objective genetic

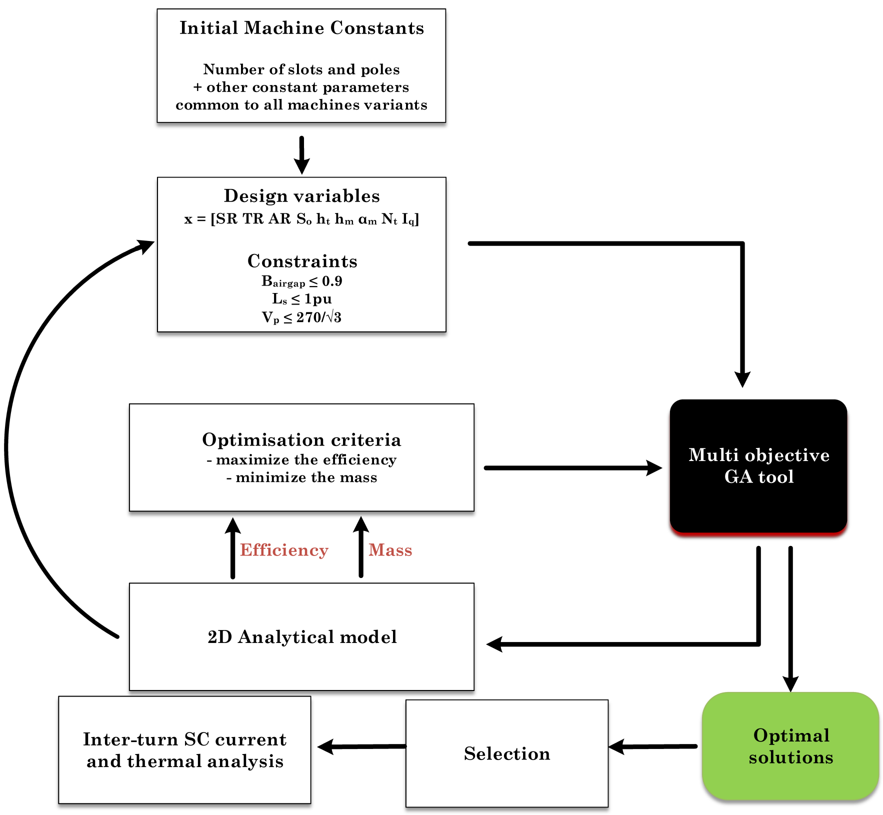

Fig. (4-2): The flow chart of the machine optimisation process and performance analysis.

algorithm (GA) is adopted for the optimisation process, in which a 2D electromagnetic model is used during the design process, while to investigate the turn-turn SC fault current 1D SC fault model is used. It is worth noting that by adopting an analytical model for the design and analysis the computation time is greatly reduced whilst maintaining a high level of accuracy. Finite element (FE) is therefore not considered here. The adopted analytical model and the GA technique for the design and analysis are discussed in the detail in following sub-sections.

4.4.1 2D Sub-domain Field Model

The analytical model is based on a sub-domain field model that solves Maxwell's equations in polar coordinates considering the associated boundary conditions of each domain. In order to establish the model, the machine geometry is divided into four sub-domains: rotor PM sub-domain (A_I - region I), air-gap sub-domain (A_{II} - region II), slot opening sub-domain (A_i - region III, $i = 1, 2...Q$) and stator slot sub-domain (A_j - region IV, $j = 1, 2...Q$), as shown in Fig. 4-3. The following assumptions were made:

1. The machine has a radial geometry as shown in Fig. 4-3.
2. The stator and rotor cores have an infinite permeability and zero conductivity.
3. The magnets are magnetized in the radial direction and their relative recoil permeability is unity ($\mu_r = 1$).
4. The current density (J_c) over the slot area is uniformly distributed.
5. The end-effects are neglected and thus the magnetic vector potential has only one component along the z direction and it only depends on the polar coordinates r and θ.

6. The walls of the slot are finely laminated so that the effect of eddy currents within the iron can be neglected.

The magneto static partial differential equations governing in the behaviour of the machine in the different sub-domains can be derived from Maxwell's equations.

These equations are formulated in terms of vector potential as in (12).

$$\begin{cases} \dfrac{\partial^2 A_I}{\partial r^2} + \dfrac{1}{r}\dfrac{\partial A_I}{\partial r} + \dfrac{1}{r^2}\dfrac{\partial^2 A_I}{\partial \theta^2} = \dfrac{-\mu_o}{r}\dfrac{\partial M_r}{\partial \theta} \\ \dfrac{\partial^2 A_{II}}{\partial r^2} + \dfrac{1}{r}\dfrac{\partial A_{II}}{\partial r} + \dfrac{1}{r^2}\dfrac{\partial^2 A_{II}}{\partial \theta^2} = 0 \\ \dfrac{\partial^2 A_i}{\partial r^2} + \dfrac{1}{r}\dfrac{\partial A_i}{\partial r} + \dfrac{1}{r^2}\dfrac{\partial^2 A_i}{\partial \theta^2} = 0 \\ \dfrac{\partial^2 A_j}{\partial r^2} + \dfrac{1}{r}\dfrac{\partial A_j}{\partial r} + \dfrac{1}{r^2}\dfrac{\partial^2 A_j}{\partial \theta^2} = -\mu_o J_c \end{cases} \tag{12}$$

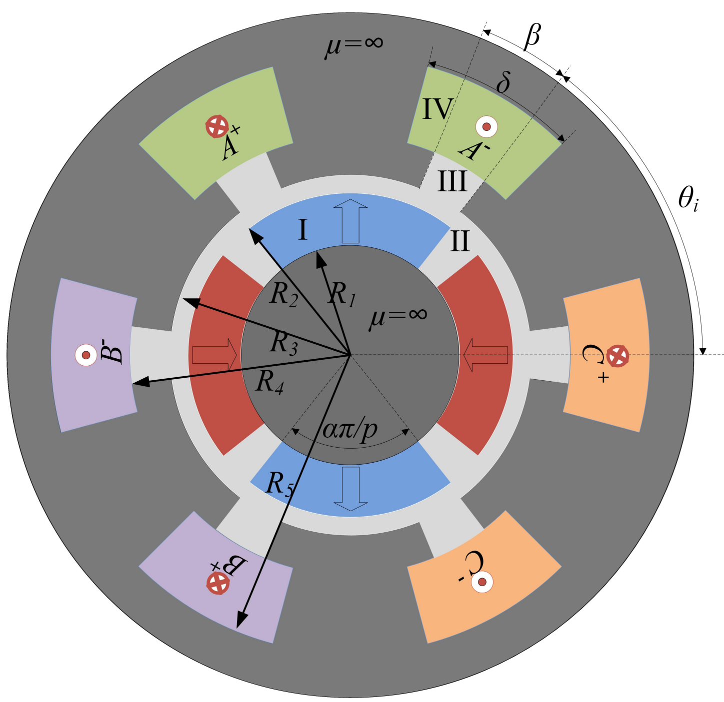

Fig. (4-3): Axial cross-section of a 6 slot-4 pole FT-PM machine.

where, A represents the magnetic vector potential and its subscript is related to the associated sub-domains. μ_0 is the permeability of air, J_c is the current density and M_r is the magnetisation radial component. Employing the separation of variables method in each sub-domain, the general solution can be obtained [51, 52]. Detailed solution of (12) can be found in [51]. Since the magnetic vector potential is known everywhere in each domain, the performance of the machine can be calculated [51, 52].

4.4.2 Performance Estimation

Using the Maxwell stress tensor, the electromagnetic torque can be calculated by considering a circle of radius r_c in the air-gap sub-domain as the integration path. Hence, the electromagnetic torque can be given as follows:

$$T_e = \frac{l_{stk} r_c}{\mu_o} \int_0^{2\pi} {B_r}^{II}(r_c, \theta)\, {B_\theta}^{II}(r_c, \theta) \; d\theta \tag{13}$$

where,

$${B_r}^{II} = \frac{1}{r} \frac{\partial A_{II}\,(r, \theta)}{\partial \theta} \tag{14}$$

$${B_\theta}^{II} = -\frac{\partial A_{II}\,(r, \theta)}{\partial r} \tag{15}$$

and l_{stk} is the axial length of the machine, μ_0 is permeability of air and B_r, B_θ are radial and tangential component in the air gap sub-domain respectively.

In order to estimate both the self-inductances (L_p) and the voltage (V_p) of the phase windings, the flux linkage associated with the cross-section of each slot (A_s) with respect to the rotor position (θ), need to be determined. The flux linkage associated with each coil can be represented by averaging the vector potential over the slot area considering the assumption (15) in the model. Thus, the flux can be described by (16).

$$\phi = \frac{l_{stk}}{A_s} \iint\limits_{A_s} A_j(r,\theta) r dr d\theta \tag{16}$$

Hence, the phase self-inductance and voltage can be represented as a function of flux as described in (17) and (18):

$$L_p = \frac{\phi\, N_{ph}}{J_c\, A_s\, K_f} \tag{17}$$

$$V_p = -N_{ph}\,\omega\,\frac{\partial \phi}{\partial \Theta} \tag{18}$$

where, N_{ph} is the number of turns per phase, K_f is the fill factor and ω is the rotor angular speed.

For the efficiency evaluation, the losses associated with the machine are calculated. The three main loss components: winding losses, iron losses and eddy current losses in the magnet are considered, while the mechanical losses are neglected. The winding losses consist of both eddy current losses in the slot and DC losses which take into account both the losses in the slot and the end windings.

To estimate the winding eddy current losses in the slot, the magnetic vector potential obtained in the slot is used. The eddy current density (J_e) and the associated copper losses (P_c) in a conductor are estimated using (19) and (20) respectively.

$$J_e = -\sigma \frac{\partial A_j}{\partial t} + C\,(t) \tag{19}$$

$$P = \frac{\omega\, l_{stk}}{2\pi\sigma} \int_{0}^{2\pi/\omega_{rm}} \int_{r_{c1}}^{r_{c2}} \int_{\theta_{c1}}^{\theta_{c2}} {J_e}^2\, r\, dt\, d\theta\, dr \tag{20}$$

where, A_j is magnetic vector potential in j$^{\text{th}}$ slot, σ is the conductivity and r_{c1}, r_{c2}, σ_{c1} and σ_{c2} are the radial and tangential coordinates delimiting the cross-sectional area of interest. In similar manner, the eddy current losses associated with the magnet are estimated using the magnetic vector potential obtained in the magnet sub-domain.

Both hysteresis and eddy current losses associated to the stator iron are estimated using well the known Steinmetz equations where, the losses generated due to localized saturation phenomena are neglected. As given in Fig. 4-4, the stator iron is divided into three parts. The flux density in each part is evaluated considering average flux density in the air gap domain. Finally, the iron losses are estimated by using the evaluated flux density together with the material properties from its associated data sheet. It is worth highlighting here that flux density harmonic effects in localized point and time harmonics associated to pulse width modulation (PWM) are not accounted for.

Since the total electromagnetic losses (P_t) are known, the efficiency (η) can be obtained from (21):

$$\eta = \frac{T_e\,\omega}{P_t + T_e\,\omega} \tag{21}$$

4.4.3 Optimization Process of the Design

The design process is carried out using an optimization routine based on a non-dominated sorting genetic algorithm (NSGAII) where above-mentioned 2D electromagnetic computational methodology is integrated to evaluate the performance [53]. The goal of the GA is to maximize the efficiency and minimize the mass of the machine. As previously mentioned, the optimisation envelope was constrained by the no-load air gap flux density (B_{airgap}), phase self-inductance (L_p) and converter voltage limit. The per-unit base

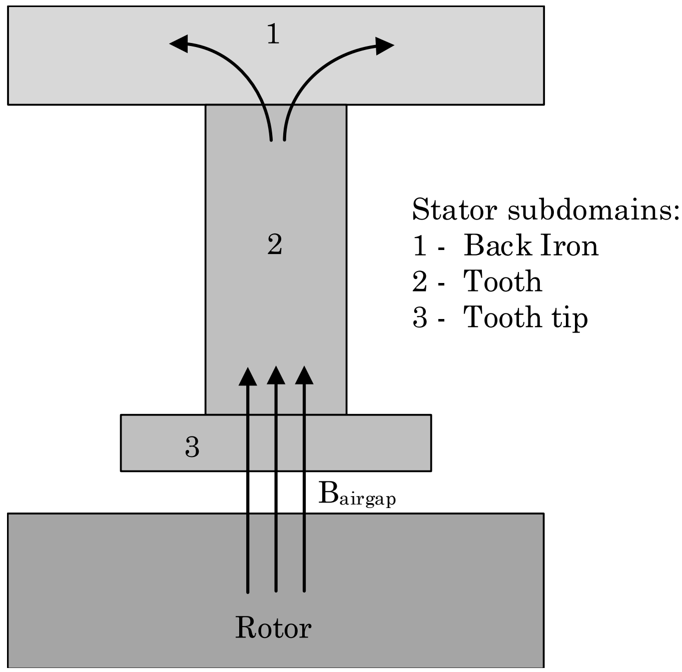

Fig. (4-4): Illustration of the stator partition for the purpose of the stator iron losses estimation.

inductance L_{pu} is set as follows:

$$L_{pu} = {}^{\Psi_{PM}}/_{I_p} \tag{22}$$

where Ψ_{PM} is flux linkage due to the permanent magnets and I_p is the rated phase current of the machine. Thus, the SC fault current during a fault will be limited to its nominal value.

The machine is chosen for analysis once the GA generates a set of Pareto-optimal solutions of the multi-objective optimization problem that satisfies both the optimization criteria and constrains. The obtained Pareto-optimal sets for all analysed machines are shown in Fig. 4-5. As in an aerospace application oriented study, lower mass is prioritised over the efficiency and therefore the set of the parameters is selected at the end of first quarter of the Pareto front with the respect to the mass. The red points in the Fig. 4-

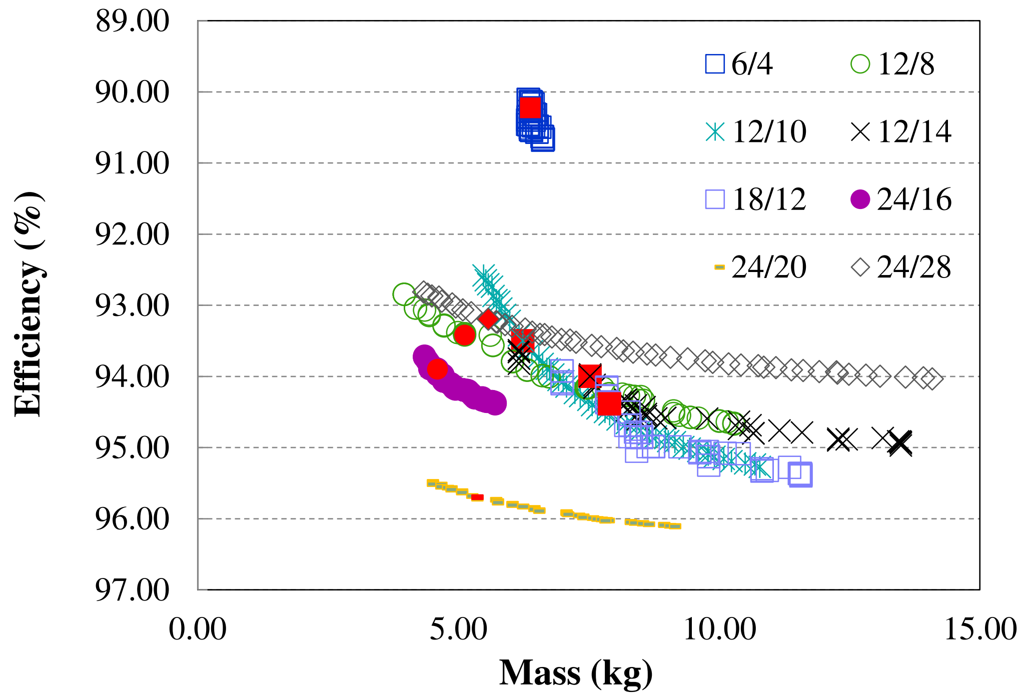

Fig. (4-5): Pareto-optimal sets for analysed machines.

5 highlighting the machines selected for the SC fault analysis presented in the paper. The design parameters of the selected machines for different S/P combinations are summarised in Table 4.2.

S/P	SR	TR	AR	H_m	N_t	Stator Mass	Machine Weight	η
[-]	[-]	[-]	[-]	[mm]	[-]	[kg]	[kg]	[%]
6/4	0.65	0.64	0.67	3.1	92	2.20	6.41	90.15
12/8	0.65	0.64	0.56	4.4	52	1.98	5.12	93.41
12/10	0.67	0.46	0.68	4.3	38	2.61	6.28	93.55
12/14	0.69	0.43	0.82	3.9	32	3.06	7.52	94.05
18/12	0.59	0.59	0.89	4.6	26	3.31	7.85	94.37
24/16	0.68	0.52	0.60	4.4	24	2.13	4.60	93.89
24/20	0.69	0.55	0.70	4.5	23	2.30	5.26	95.70
24/28	0.69	0.51	0.74	4.7	20	2.50	5.57	93.17

Table (4.2): Final parameters of the optimised machines

4.4.4 SC Current Calculation

Once the machine design has been finalised, the SC analysis is carried out at the post processing stage. A simplified 1D analytical method proposed in [19] is adopted for this study. The 1D model used to predict the SC current is computed during post processing. A 2D model can be considered but it involves solving the problem in each conductor sub-domain instead of in the slot sub-domain. This would significantly increased the evaluation time of the considered optimisation process. The adopted model estimates the inductances during a SC fault condition considering that the short-circuited turn is surrounded by the remaining healthy turns. This facilitates the accurate prediction of the leakage fluxes; consequently, the inductances can be determined and taking into account the total winding resistance the fault current can be calculated [19].

4.5 Performance comparison between different slot and pole combinations

In this section, results from the investigation of the effect of S/P combination on inter-turn short circuit current in FT-PM are presented. This section is divided into three subsections, where the outcomes of the individual analyses are explained. Losses and SC fault current were analysed for each S/P combination and thermal analysis has been performed for selected S/P variants. In addition, a method which minimizes the SC fault current is proposed.

4.5.1 Losses and Efficiency of the Studied Machines

The loss break down for each of the machines studied is shown in Fig. 4-6. While the AC and the DC winding losses are a major part of the total losses

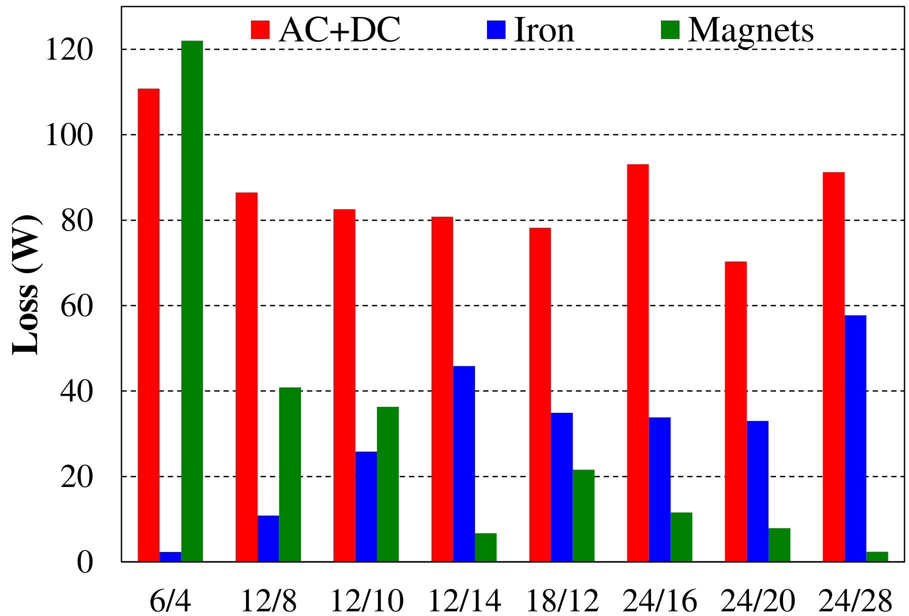

Fig. (4-6): Comparison of the individual losses across the studied machines ("AC+DC" represents AC and DC copper losses, including the end winding losses; "Iron" and "Magnets" represents eddy current and hysteresis losses in the stator iron and magnets respectively).

in all cases, the low slot number machines show high winding losses. The increase of the winding losses is mainly due to the bigger end windings' length of the machines with low slot number. The high pole number machines have high iron losses due to the higher electrical frequency necessary for their operation. Also it is worth noting that the 12/14 machine has higher iron losses than the 24/16 and 24/20 machines. The stator iron loses are dictated not only by the fundamental frequency of the phase current, but also by the mass of the machine's stator core. As is shown in the Table 4.2, the mass of the 12/14 machine's stator core is bigger than the mass of both 24/16 and 24/20 machines' stator core and so are the iron losses of the 12/14 machine.

From Fig. 4-6 and Fig. 4-7, it can be seen that the 6/4 machine proved to have the highest losses and thus lowest efficiency. This is mainly due to high winding losses and magnet eddy current losses. If the segmentation is

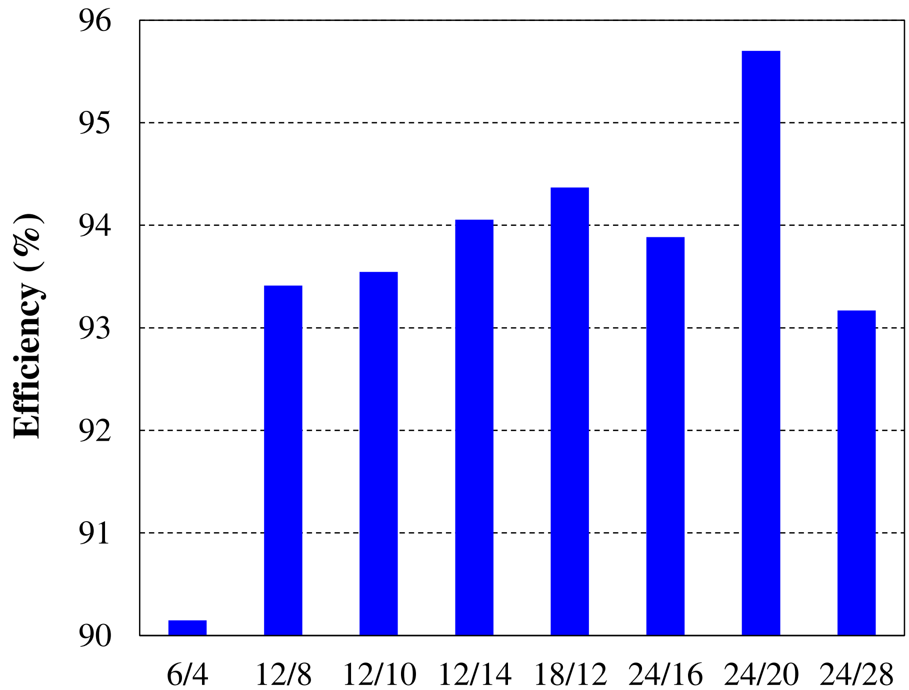

Fig. (4-7): Comparison of efficiencies across the studied machines.

adopted for the machine, the magnet eddy current losses can be reduced. Although this would be possible, the resultant efficiency will depends on number of segments adopted in the design.

As can be seen from Fig. 4-7, it is obvious that amongst the considered machines, the 24/20 machine variant which delivers rated output with 95.7% efficiency is the best design choice in terms of the performance.

4.5.2 Short Circuit Current in the Faulty Turn

As explained earlier, the results of the SC analysis are based on a 1D analytical approach. In the analysis, position of the faulty turn in the slot is expressed by the relative position, where 0 corresponds to the outer border of the slot, and 100 corresponds to the inner border of the slot which close to the slot opening as is illustrated in Fig. 4-8. The obtained SC fault currents with respect to the location are given in Fig. 4-9.

Clearly, for all the analysed machines, the highest SC current is caused when the inter-turn fault occurs near the slot opening area. It is worth noting that the magnitude of the SC fault current increases with increasing pole number.

Although the S/P combination of 24/20 variant has higher efficiency, it produces the largest SC fault current of more than 5pu. If the focus mainly is given to the fault tolerance, the 6/4 variant is the best candidate amongst analysed machines. This clearly explains that a balanced trade-off between efficiency and FT is required for the design of machines for applications where FT is desired.

Amongst other candidates, S/P combinations of the 12/8 and 12/10 machines have similar SC behaviour. It also can be seen in S/P combinations 12/14 machine and 24/16 machine. This is because of associated electrical frequencies which are almost equal. Although these pairs of machines pro-

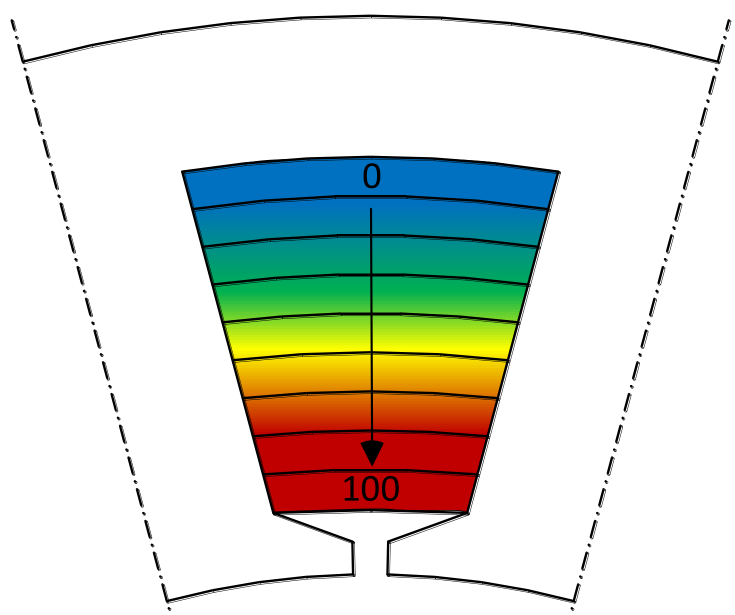

Fig. (4-8): Illustration of an inter-turn SC fault location reference in a slot.

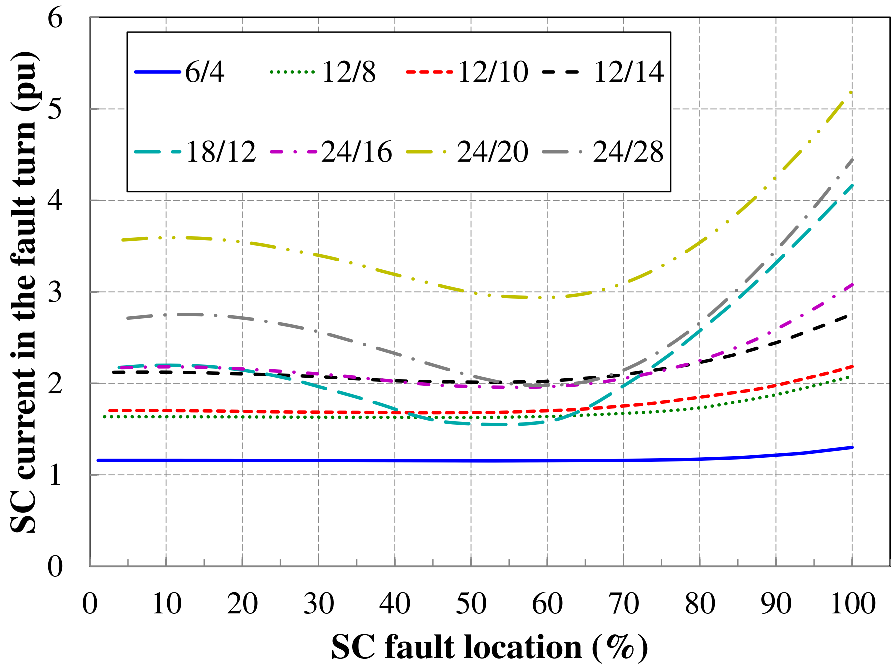

Fig. (4-9): The inter-turn SC fault current vs. fault location in a slot (0 and 100 represent locations close to the inner and outer boundary of the slot respectively).

vide almost identical results regarding SC, in terms of efficiency, the 12/8 and 12/14 machines show increased efficiency.

4.5.3 Thermal Analysis of the Studied Machines

In order to visualize the thermal behaviour, the thermal analysis was performed using FE software and was carried out in a coupled electromagnetic and thermal FE environment. Two states, the healthy and faulty, are studied. The healthy state is simulated with a nominal phase current.

For the faulty state, to minimize the evaluation time, the steady state SC current obtained in the inter-turn SC fault analysis is injected into the faulty turn. The remaining healthy windings are separately excited using the nominal phase current. In the analysis, thermal continuity between stator and rotor is taken into account and the thermal boundaries (stator outer surface temperature is fixed to 120 °C) are kept the same for all cases. The conductors' cross-sectional area and insulation thickness are carefully selected considering slot fill factor $K_f = 0.5$. Results obtained for four cases are presented in Fig. 4-10.

The SC analysis proved that the 6/4 machine is the most tolerant to the inter-turn SC fault, the difference in the thermal distribution in the slot between the healthy and fault condition is almost negligible. As expected, high pole number variants 24/16 and 24/20 shows noticeable temperature rise at fault condition. Fig. 4-10g), h) show that the 24/20 machine variant has critical hotspot due to the larger fault current. It is worth highlighting here that although 24/16 machine variant is subject to less magnitude of worst-case SC current than 18/12 variant, it has poorer thermal behaviour. This is due to the windings resistance associated to the 24/16 machine variant which is higher than in case of 18/12.

From the analysis and the results presented in Fig. 4-9 and Fig. 4-10, it can be summarised that analysed low pole number PM machines are suitable for FT design although they have low efficiency compared to the analysed high pole number machines. Overall, the 12/8 and 12/10 machine variants proved to be the best compromise for such FT designs since they have higher efficiency and the SC current almost twice the rated value.

4.5.4 Modifications towards SC Current Reduction

Although the 12/8 and 12/10 machine variants are best choice amongst others in terms of FT and efficiency, those machines have almost twice the rated current when fault occurs close to the slot opening region. One way of minimizing the fault current is to design the machine with a larger inductance which can be even higher than one per unit inductance. Whilst possible, this would result in a lower power factor and a significant reduction in the

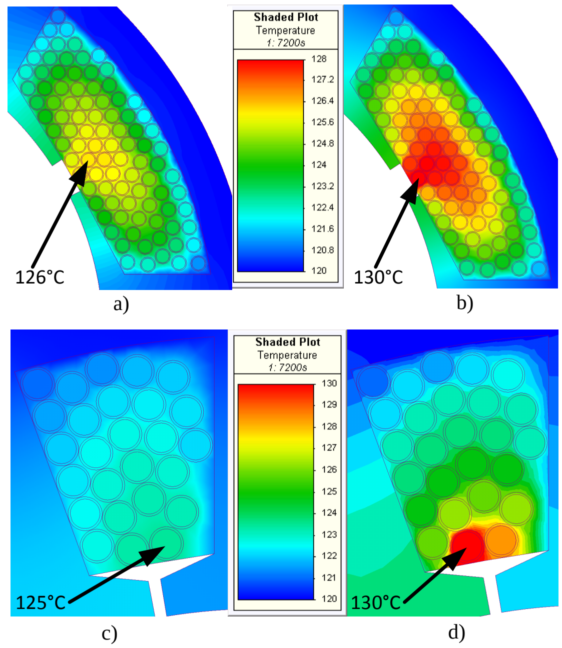

Fig. (4-10): Thermal distribution in a slot of: 6-slot, 4-pole machine under (a) healthy, (b) faulty condition; 18-slot, 12-pole machine under (c) healthy, (d) faulty condition

achievable torque density.

Alternatively the maximalSC current can be maintained at twice the rated by avoiding, the placement of the winding closer to slot opening region. From Fig. 4-9, it is obvious that by using only 90% of the slot for the winding and avoiding 10% closest to the slot opening region replaces the maximalSC fault current significantly. For the 12/8 and 12/10 machine variants, theSC current can be limited under 2pu, if the 10% slot region is avoided. However, this will reduce the slot fill factor, consequently increasing the DC losses. However it would be beneficial if the machine is operated at high speed as the AC losses would be reduced [54].

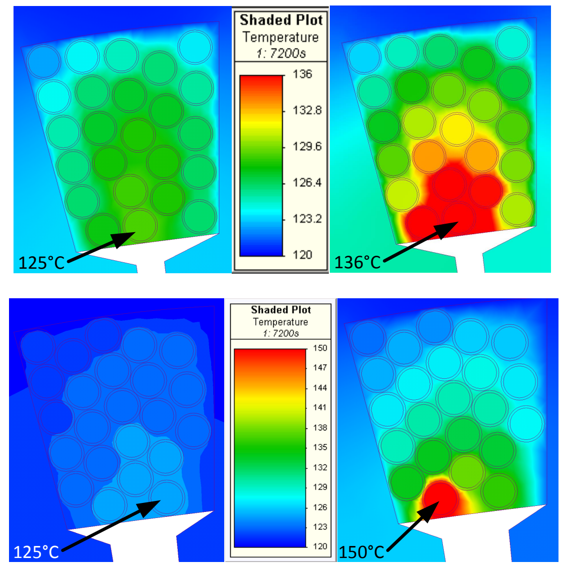

g) h)

Fig. (4-11): Thermal distribution in a slot of 24-slot, 16-pole machine under (e) healthy, (f) faulty condition; 24-slot, 20-pole machine under (g) healthy, (h) faulty condition.

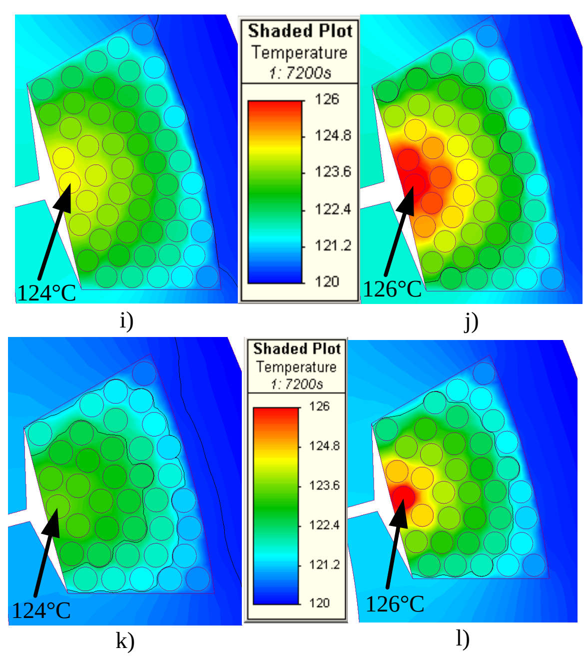

Fig. (4-12): Thermal distribution in a slot of 12-slot, 8-pole machine under (i) healthy, (j) faulty condition; 12-slot, 10-pole machine under (k) healthy, (l) faulty condition.

4.6 Conclusion

This chapter has highlighted the issues on permanent magnet assisted machine under the SC fault. From the analysis, it is evident that the performance has to be compromised to achieve a better FTe. To achieve a high torque to mass ratio, it is required to have higher pole number. On the other side, high pole number significantly influences the fault current. To improve the FTe without compromising the torque density, alternative design topologies should therefore be considered. The topology that eliminates the PM material would be an ideal candidate. This is the subject of the next section.

Chapter 5

Field Wound Flux Switching Machine

This chapter introduces an idea of utilisation of the existing PMSM stator and performing its rotor modification to transform it to the FWFS; a magnet less machine to create cheaper machine with improved FTe capability. Minor but necessary modifications regarding winding connection are presented and the process of the optimal rotor design is fully described as well as the final design of the rotor optimised for maximal torque performance. Also the trade off between the best performance and practicality of the solution is risen and the consequences are elaborated.

5.1 Introduction

As was pointed out Chapter 4, the inter turn SC fault can have serious consequences for the machine condition, especially if it is PMSM used in a direct drive application. There is no simple and non-destructive way of de-excitation of PMs in case of SC fault occurrence. Although the electric machines containing or utilising the PMs for excitation purposes achieves high torque density among other types of electric motors, the use of the PMs increases the manufacturing cost of the motor.

Hence for the applications, where the main factors of the valuation of the suitability of the machine are costs and FTe, while lower torque performance is acceptable, the way of an machine topology with alternative excitation system allowing omitting PMs is the solution that can deliver desired low cost while improved FTe solution. The excitation system can be chosen with the stress on its controllability and the manufacturing simplicity, therefore there will be no charges for PMs materials and manufacturing costs coupled with their fitting and also the emphasis can be on designing machine with the rotor topology of simple geometry.

5.2 The task

The opportunity to use one of current machines manufactured by the Cummins Generators has risen. In detail, use the stator of so called Gen 3.1 machine with none modification in its geometry and with minimal changes in coils arrangement to create a new machine that would utilised not PMs at all and offered higher FTe capability in case of the inter turn SC fault compared to Gen 3.1.

5.3 The motivation

The reasons behind, why to even investigate such possibility are evident. The Gen 3.1 has been designed to deliver requested performance and to fulfil its duty. It is obvious, that the effort and and finance put in the design of the Gen 3.1 can be increased by utilising the Gen 3.1 stator for another type of machine. Also simplifying the rotor structure together with avoiding PMs means noticeable price drop.

5.4 The benefits

As has been pointed out already, the fact that the new machine is excited by winding instead of PMs brings huge improvement in FTe capability as in case of inter tyrn SC fault the excitation is under control and can be used to minimise the consequences of the fault. This makes the FWFS machine great candidate for direct drive application or for applications, where the machine cannot be disconnected from the drive train, but is in use only for part time of the operation.

5.5 The evaluation criteria

Although there is no intention to deliver machine with comparable performance to Gen3.1, the main evaluating factor is torque performance. The reason, why these two machines won't be compared are, at first, because the application of the two machines are different and second, it is rather very challenging to design a machine of the same size and power rating with at least similar torque capability with and without any PMs used, while using the same stator configuration. Although it has been pointed out that the torque wise the machines can not be compared as it is, the design of the machine is focused on maximising the torque performance. To achieve conditions under which the machines' comparison can be considered as fair, the nominal current of the new machine is set to be the current of equal copper losses as during the Gen 3.1 normal operation.

5.6 The Gen 3.1

The Gen 3.1 is an inset permanent magnet synchronous machine (IPMSM) designed by the Cummins Generators for traction application and it is already implemented on large size hybrid vehicles such as hybrid buses and trucks. It is a three phase 30kW, 16 poles, water cooled machine that accommodates concentrated winding placed in 24 stator slots with 8 coils per each phase. The coils in each phase are connected in parallel and the three phase winding is connected through the connection rings to allow operation in the delta connection.

The detail of the section of one quarter of the Gen 3.1 is shown on the Fig 5-1 and its detailed parameters are summarised in the Table 5.1.

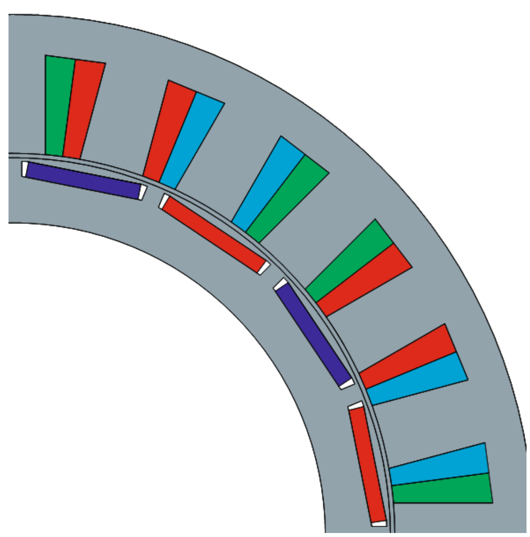

Fig. (5-1): Cross section of quarter of the Gen 3.1

Parameter	Value	Units
Nominal torque	220Nm at 1300rpm	
Peak torque	660Nm at 868rpm	
Stator OR	200	mm
Rotor OR	145	mm
Tooth type	Parallel tooth	
Stack length	85	mm
Air gap length	1.7	mm
Number of poles	16	-
Number of slots	24	-
Number of parallel paths	8	-
Turns per slot	73	-
Magnet mass	2.7	kg
Connection	Delta (concentrated)	

Table (5.1): Parameters of the Gen 3.1

5.7 Principle of operation of the FWFSM

Prior the design of the machine, the principle of operation of the machine must be clear, hence it is going to be explained bellow. A section of the FWFS is shown on the Fig. 5-2. FWFS machine is characteristic by two types of windings placed in the stator slots. These are armature and field

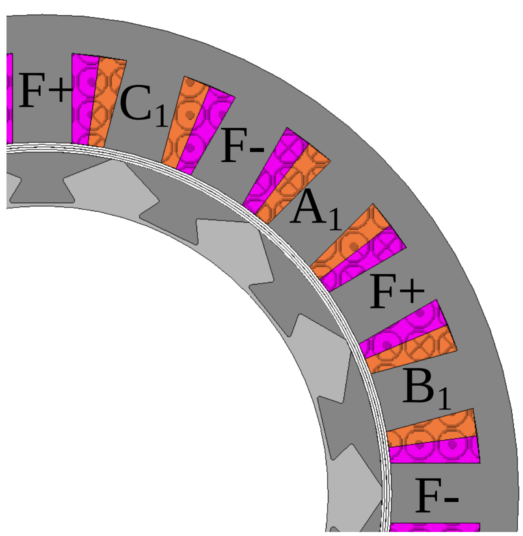

Fig. (5-2): Section of the quarter of the FWFS winding and their placement in the slots alternate. Further will be referred to the tooth surrounded by an armature coil as armature tooth and similarly to a tooth surrounded by field coil as a field tooth. The field winding provides machine with the excitation. To ensure correct function of the machine, the flux linkage produced by one field coil must be opposite to the direction of the flux linkage produced by the adjoining field coil. This will enable change of polarity of the flux linkage in the armature coils. The direction of the flux linkage produced does not change and remains the same during the operation of the machine. Armature windings are placed in remaining

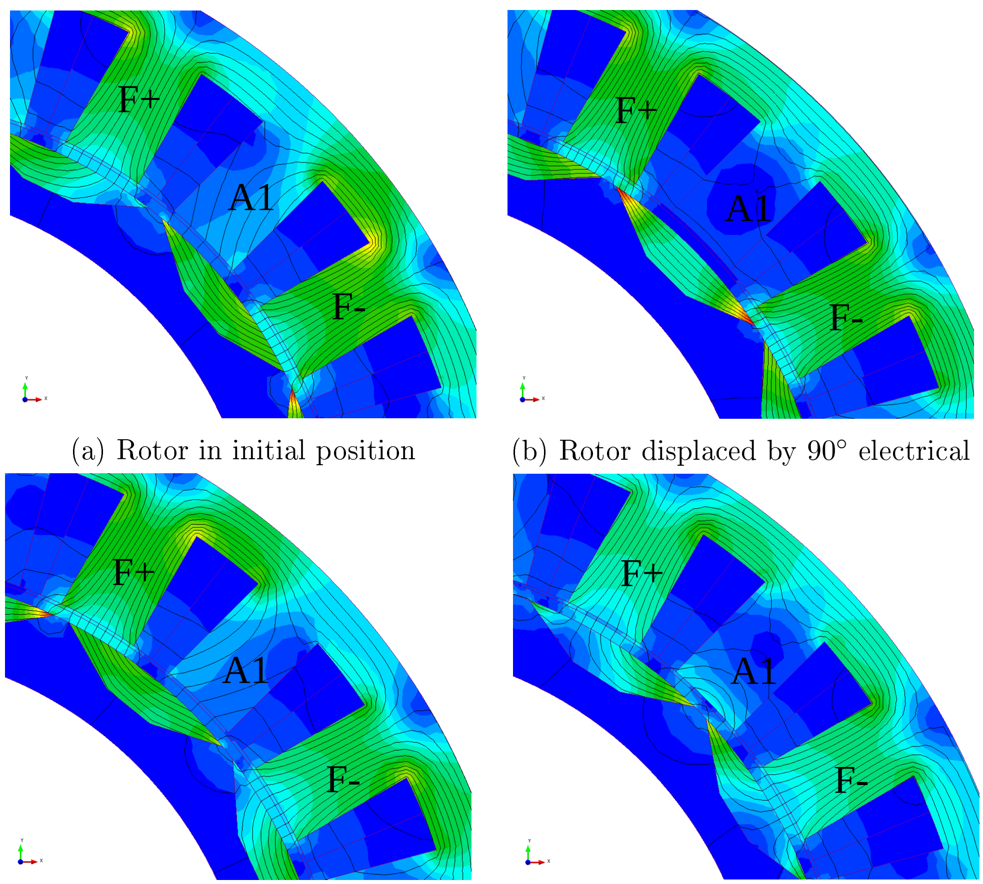

(a) Rotor in initial position (b) Rotor displaced by 90° electrical

(c) Rotor displaced by 180° electrical (d) Rotor displaced by 270° electrical

Fig. (5-3): One electric cycle rotation of the rotor in four steps, 90° electrical each. Only field winding is fed.

slots following the pattern to enable three phase operation. This pattern is changing accordingly with number of rotor segments used.

To demonstrate the function of the three phase FWFS, one electrical cycle of the rotation is shown on the Fig. 5-3 and corresponding phases of the induced BEMF flux linkage in phase A are shown in the Fig. 5-4, from which is also evident, why the initial position was chosen in this point.

In the initial position , Fig. 5-3a, the rotor segment is aligned between the the field tooth and tooth encircled by one of the phase A coils. The flux linkage produced by the field coil is linked to the armature coil through the air gap and the rotor segment. With the displacement of 90° electrical, Fig. 5-3b, the rotor segment moves into the position, where no flux is linking the field and armature coil. This is the first moment when the flux linkage in the armature coil is zero. In another 90° step, Fig. 5-3d, the segment is in the position, where it links the armature coil with another field coil. Hence

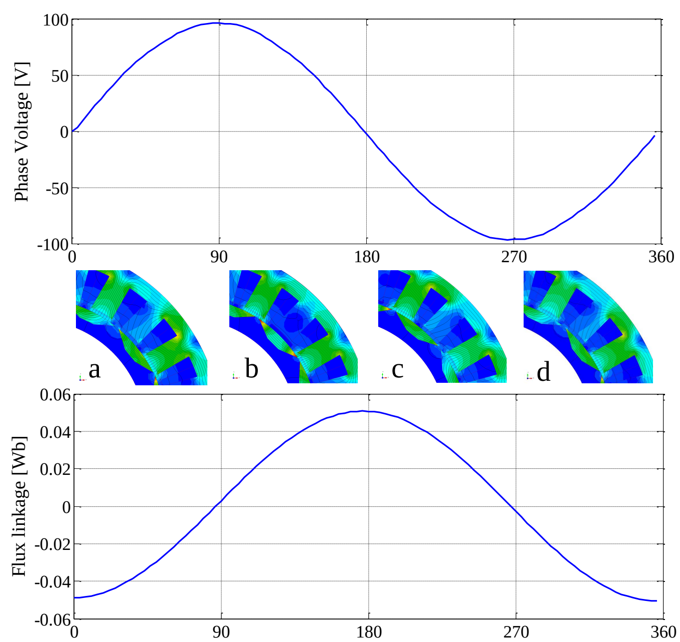

Fig. (5-4): Rotor rotation of one electrical cycle with current only in field winding the flux in the armature tooth is now of opposite direction than in the first step.

The last step, (Fig.5-3b), the segment gets for the second time in the position where is no flux linked to the armature coil and the cycle is complete. By extending described process to the remaining armature coils and hence other two phases, the machine is capable maintaining three phase operation assuming correct ratio between the number of stator slots and rotor segments.

Here is worth point out that as was just shown, the field teeth are during the operation stressed with the unipolar flux linkage, while the armature teeth and back iron part that connect the armature teeth to the field once faces bidirectional flux. It also shows, that when the magnetic flux from field tooth linking adjoining armature coil, all the flux is flowing through the back iron. This is different situation from operation of the Gen 3.1 , where the flux flowing from a tooth split on both sides.

Hence the stator back iron of the Gen 3.1 is of half thickness of the stator tooth, the optimal width of the FWFSM stator back iron should be of the same thickness as the tooth.

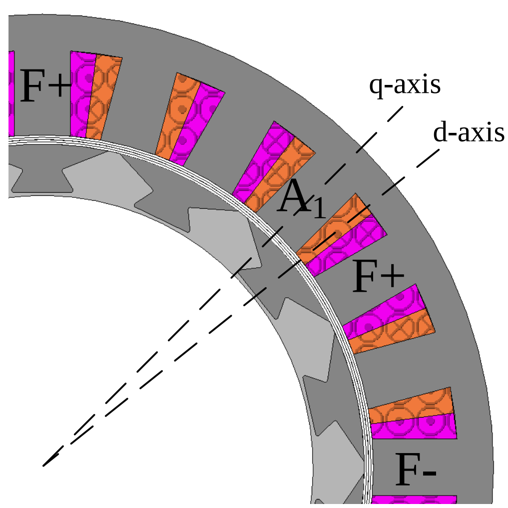

Fig. (5-5): Direct and quadrature axis interpretation in FWFS machine

However, it can be seen from the 5-3 that the back iron is not saturated, even the flux produced by the field coil does not split in two ways, but all the flux flow in direction to the one of the adjoining armature teeth.

5.8 Stator related modifications

Although one of the main design conditions was not to modify the geometry of the machine stator, minor changes have to be done in the way how the coils are going to be connected to allow proper function according to principle of operation of the FWFS machine. Hence the rings, used to connect the phases of the Gen 3.1 in to the delta connections can be removed, as they are not providing the flexibility needed in coils arrangement needed. After their removal, the space cleaned can be used to bring out terminals of every coil out of the casing and achieve flexibility in changes of the way how their are connected and utilised. This can be seen in the Appendix B.1. This is the only modification regarding the stator during the whole process of Gen 3.1 modification.

5.9 Rotor design process

The process of the rotor design is described in several steps. As it has been already identified that the best alternative type of the machine is the FWFS, the design process consists of following steps:

- Number of the rotor segments determination
- Segment shape and dimensions optimisation to deliver best torque performance
- Performance analysis

- Modification to the proposed rotor design based on the previous analysis

5.9.1 Number of segments

The Gen 3.1 is IPMSM with 16 poles, ie. 16 PMs inset into the rotor. As was shown in the Section 5.7, the number of rotor segments influences the operation of the machine in many ways. In the number of segments defines pole pair number of the machine as the electrical angular speed of FWFS is given as:

$$\omega_e = n_s \omega_m \tag{1}$$

where n_s is number of rotor segments and ω_m and ω_e are mechanical and electrical angular speed respectively. Also not all the numbers of rotor segments work ideally with the 24 slot stator or at all.

The rotors that were initially considered were with 7 to 24 segments. This range was chosen due to the fact, that smaller number of segments would lead to ineffectively big segments, considering the diameter of the machine's rotor and rotors with number of segments equal or larger than the number of slots would conclude in segments not able to fully overlap the adjoining teeth. Most of these rotors have potential to work in combination with 24 stator slots, apart from some of them. These are the rotors with number of segments divisible by three [55]. This rotor topology leads to a single phase machine. Also the the rotors with odd number suffer from unbalanced magnetic force and hence are not preferable if other segments number can provide balanced performance.

The first step to find the ideal number of rotor segments was a no load test with rotors equipped with the rotor segments within the range of 7 - 24 segments. The results are shown on the Fig. 5-6 that shows results for one phase, but for each of the coils separately and on Fig. 5-7, where the voltages are summed up and added remaining two phases to get complete three phase BEMF. Although the results were produced without any further optimisation of the segments shape, hence the performance between the machines cannot be compared, at this stage such simplification is not a problem, as the overview it provides over the BEMF is still credible.

As the result, it can be seen that the rotors with segments of multiple of three cannot generate three phase BEMF and hence cannot be considered for this application. Apart from this, it is shown, that rotor with equal number of segments and slots does not produce any BEMF. The rotors with 7,13,17,19, and 23 segments generate BEMF with double the frequency of the actual electrical cycle. Rotors with 8,16 and 20 segments produce BEMF with high harmonic distortion and hence the remaining rotors with 10 and 14 segments are concluded as the topologies to be investigated further towards as the candidates.

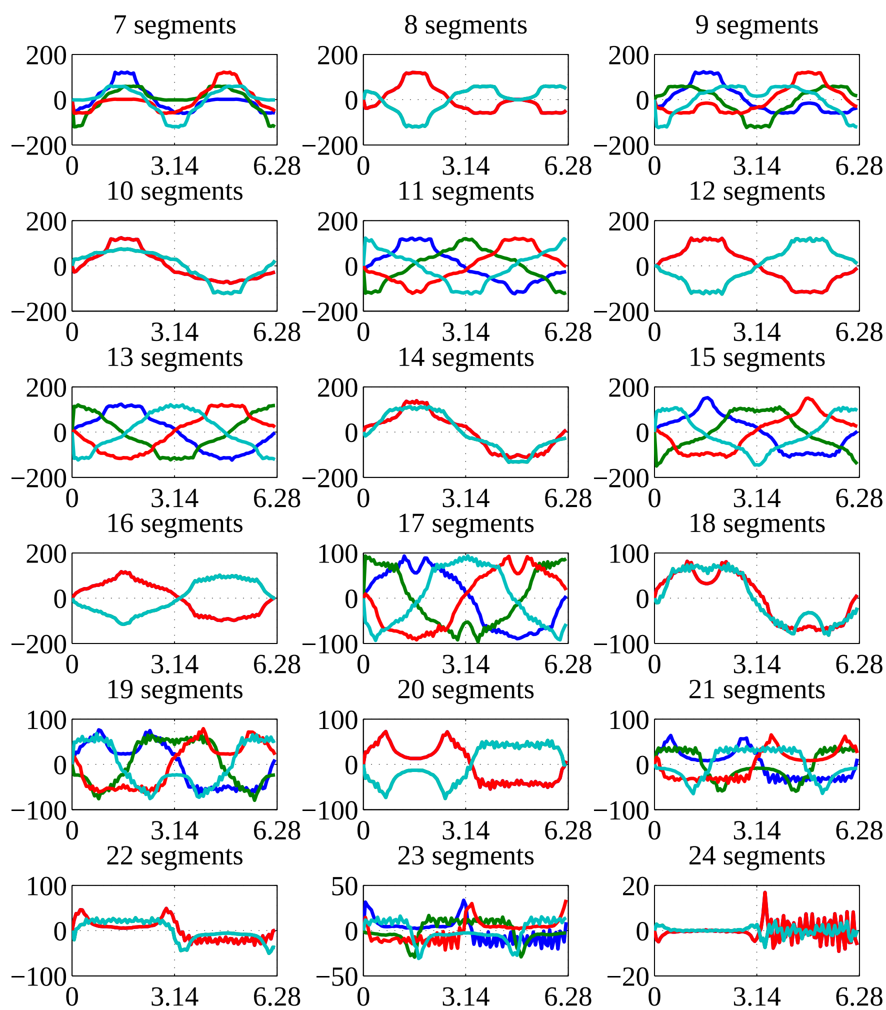

Fig. (5-6): BEMF for one phase consisting of four coils for FWFS machines with 7 to 24 segments on the rotor for one electrical period. $ag = 1.7mm$, speed 1300rpm.

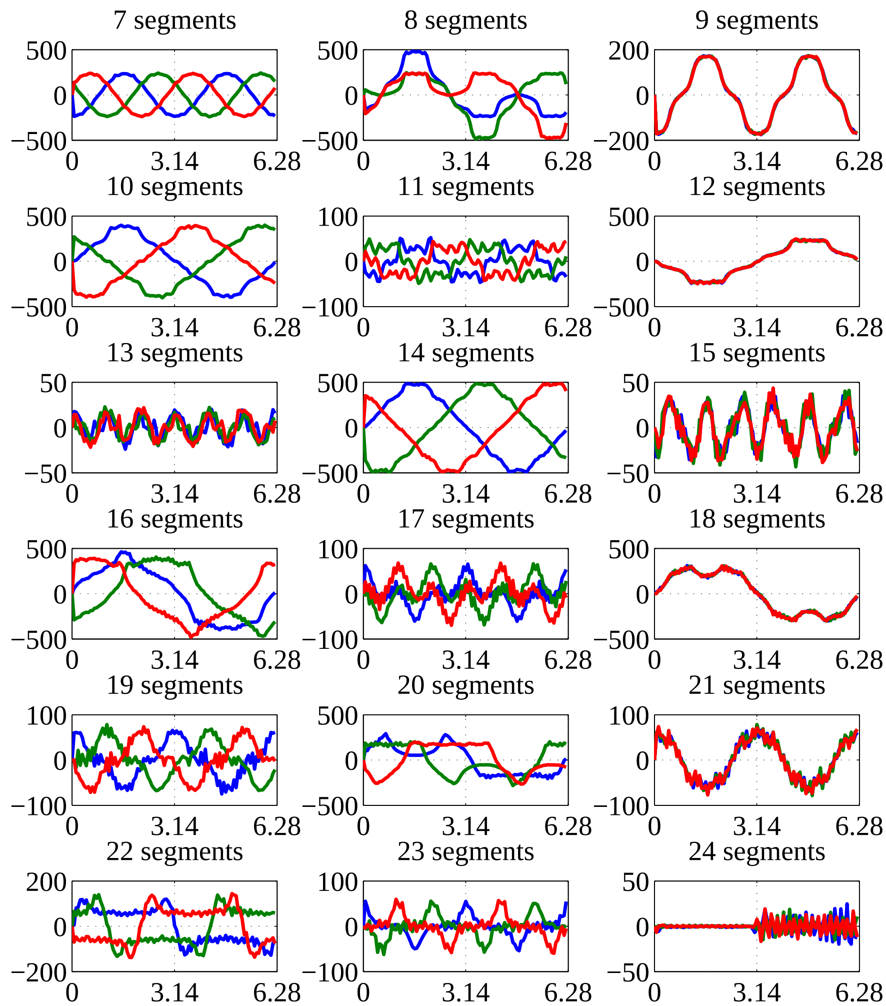

Fig. (5-7): Three phase BEMF for FWFS machines with 7 to 24 segments on the rotor for one electrical period. $ag = 1.7mm$, speed 1300rpm.

Comparing the BEMF of both the machines with Wye windings connection, the result of the fast Fourier transformation (FFT) showed on Fig. 5-9, in both machines is first harmonic dominant, but BEMF of the machine with 10 segments is influenced also by the third harmonic.

The torque comparison of performance under the load, showed on the Fig. 5-8b, in respect to mean torque resulted better for the rotor with 14 segments. Therefore based on these outcomes, from all the considered number of segments, the optimisation and design process focus on the rotor with 14 segments.

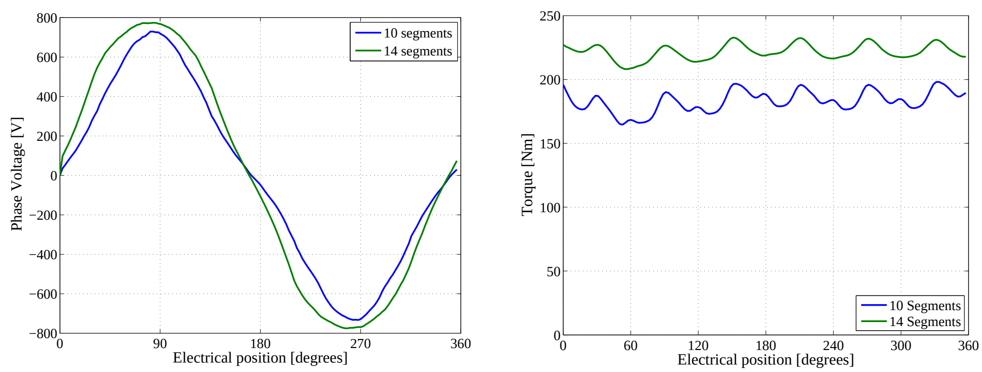

(a) BEMF for the machines at 1300rpm

(b) Torque for the machines, $i_q = i_f = 33A$

Fig. (5-8): Comparision of the machines with 10 and 14 segments

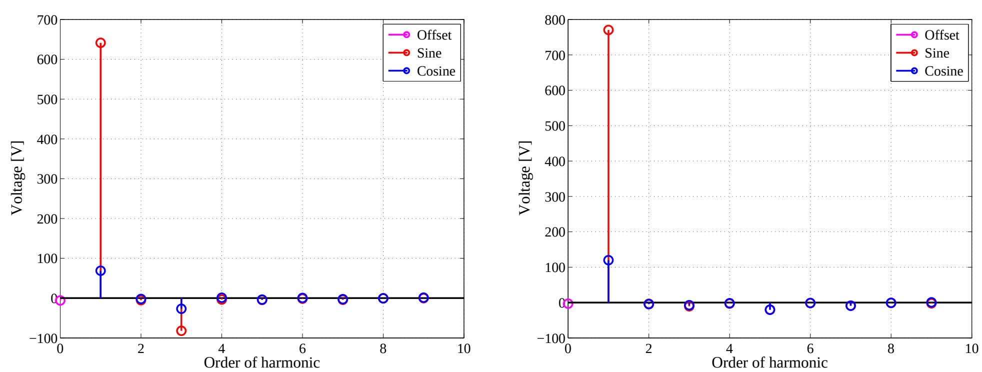

(a)

(b)

Fig. (5-9): FFT of the BEMF for 10 (a) and (b) 14 segments rotor

5.9.2 Segment dimensions

For the optimisation process three parameters of the segments were chosen. They are visualised on the Fig. 5-10, and are namely Segment span, segment depth and base width. These parameters were iterated and for every combination of them was simulated load operation of the machine. Then, the performance was evaluated and the machines were compared regarding their mean torque performance.

The boundaries of the segments dimensions were based on the geometrical limitations. The depth of the segment was limited due to the possibility of using the rotor hub of Gen 3.1 , to further increase the proportion of reused parts. Also the segment span was limited in the way, that its lower limit had to be big enough to overlap two adjoining tooth and its upper limit was set to avoid unwanted leakage between two segments. Base width was limited in the to respect the distance given by the segment span, it means that the point, where the two segments are closest to each other is at the tip of the segment.

After the first set of simulations, it became obvious that regarding segment span, the wider it is, the better performance it provides. Hence the optimisation process was later reduced to two parameters, the segment depth and segment base width. The results for all simulations are visualised in the

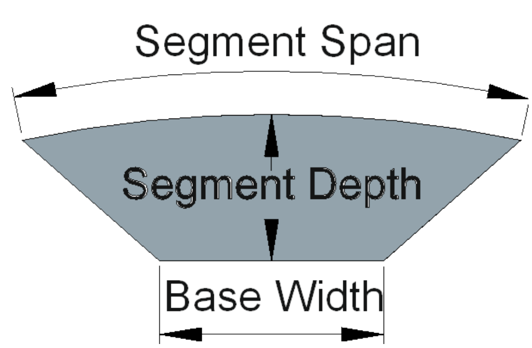

Fig. (5-10): The segment parameters for optimisation

Fig. 5-11.

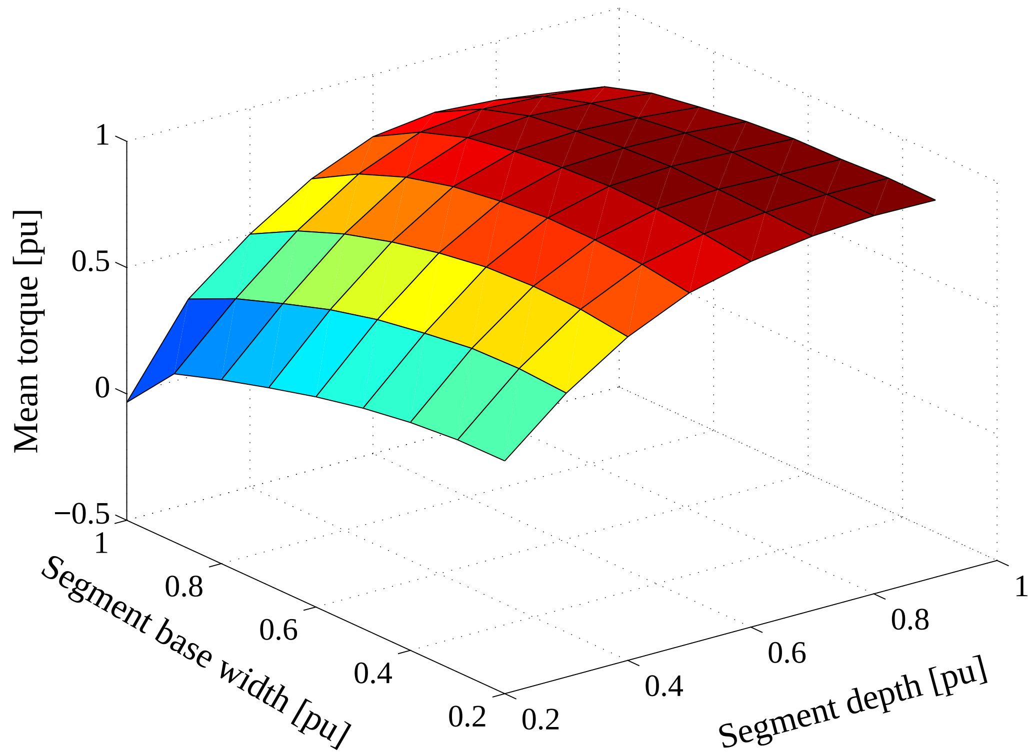

Fig. (5-11): Outcome of the segment dimensions optimisation for 1300rpm, $I_q = 23.6A$ $I_f = 16.7A$ and 1.7mm air gap

5.9.3 Air gap variation

The Gen 3.1 was designed with the active air gap (AG) of 1.7mm thickness. This thickness is optimal for such a PMSM machine, as it reflects the design and the air gap flux density restrictions. It is hence convenient to choose the 1.7mm AG as the base for the torque performance across the variations of the AGs as shown on the 5-12. With the FWFS machine, AG can be minimised, to improve the torque performance. Although it has been stressed out that the direct comparison with the Gen 3.1 torque wise is not the appropriate, it worth note the absolute values of the achieved torques at various AGs. To make the comparison fair, the machines are simulated under the current

Table (5.2): Comparison of torques of FWFS machines of various AGs against Gen3.1

Machine variant	Mean torque [Nm]
Gen 3.1	220.0
FWFS 0.5mm AG	139.5
FWFS 1.7mm AG	33.8
FWFS 4.0mm AG	13.5

loading, that will create the same copper losses, as if the Gen 3.1 is fed by its rated current. It means $I_f = 9.6A$ and $I_q = 16.6A$. The results are summed up in the table .

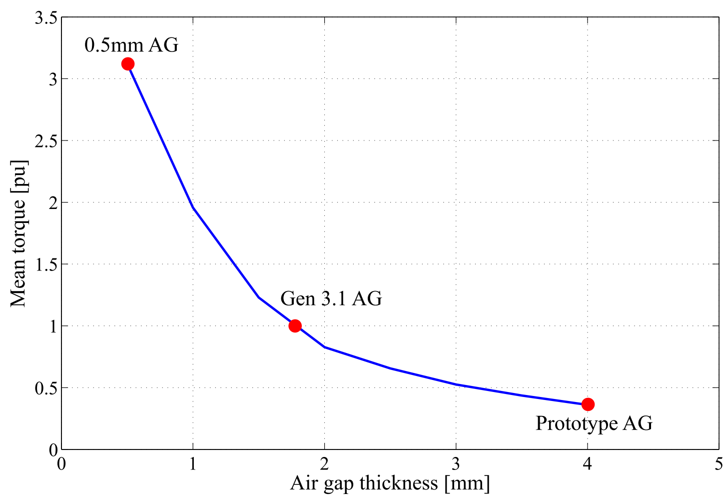

Fig. (5-12): FWFS machine air gap variation

The simulations showed that by shrinking the AG thickness to 0.5mm, the torque could be improved more then three times compared to the 1.7mm AG. Unfortunately, in the case of our machine, the air gap not only could not be decreased, but it had to be increased to 4mm. The main reason behind such step against the torque performance, was to maintain control simplicity. As the machine control scheme consist of three phase inverter to control the armature winding, the field winding could be controlled by a simple DC supply. Lowering the air gap would cause unipolar voltage ripple in the field winding. This would mean, that to maintain a constant DC current, an AC voltage would be needed and hence a simple DC supply would not be able to control the field current. With the 4mm AG, the the field voltage ripple is not removed, but it is suppressed, therefore to keep field current constant, only unipolar DC voltage is required.

Due to this complication, the segment's dimensions that were optimised for 1.7mm AG had to be redesigned in the same way, as was described in the subsection 5.9.2, to obtain design that respect the new circumstances.

The final shape and dimensions of the segment are shown on the Fig. 5-13 and 5-14. The stack length of the pack is 86.75mm and it is cut of silicon steel M235-35A with lamination thickness of 0.35mm as is evident from the material name.

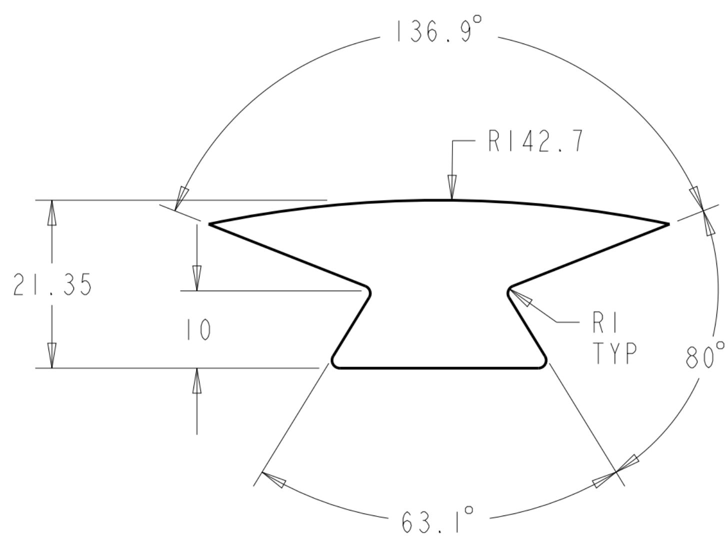

Fig. (5-13): Final segment dimensions

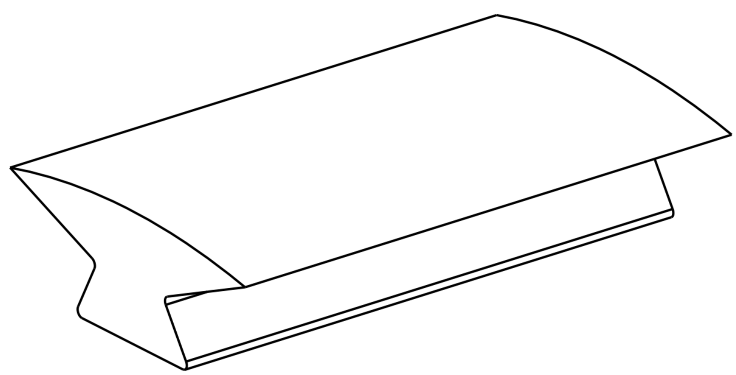

Fig. (5-14): Final segment dimensions - isometric view

5.10 Conclusion

In this chapter, the Gen 3.1 was introduced and the motivation and benefits behind its re-utilisation were highlighted. The FWFS machine has been identified as a machine with the stator topology very similar to the Gen 3.1 therefore the rotor could be designed accordingly to the needs of the stator. Minor changes to the stator were introduced and the whole design process of the rotor was described. Following the analysis of best combination of the number of segments and number of stator slots, the rotor with 14 segments was evaluated as the best performing. Then the segment's shape optimisation was described and trade off between torque capability, technical difficulty and control strategy has concluded in the concession of larger air gap to keep the possibility of simple control topology with a simple DC current supply instead of need for another inverter. This choice of the 4 mm air gap thickness had its negative influence on the performance of the machine in a way that the achievable output torque resulted in ten times lower value compared to the machine design with 0.5 mm air gap thickness. The dimensions of the rotor segments were therefore redesigned to improve the torque performance under the new conditions and the draft of the segment was presented. The experimental validation of the final design is presented in following chapter.

Chapter 6

Experiments on the FWFSM

This chapter presents the experimental rig that has been built for the experiments and tests performed on the FWFSM. The results obtained from the experiments on the FWFSM and their comparison with the predictions based on FE analysis and models of the FWFSM are provided. The experiments are divided into no load/no excitation and load tests, where each part contains set of experiments. Description of each experiment is provided, as well as comments on the results.

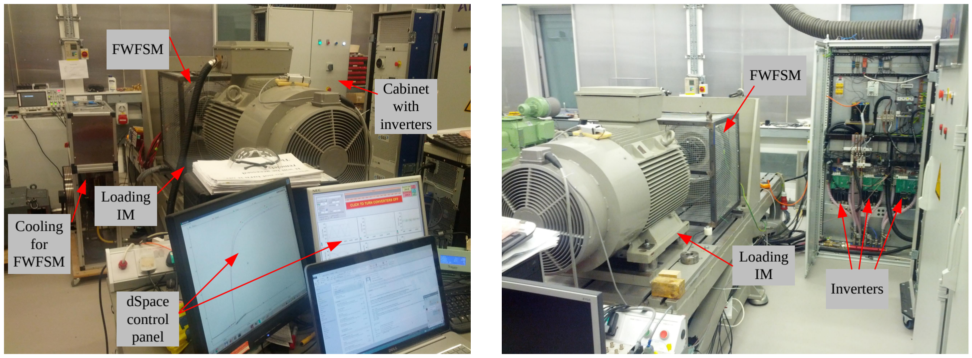

(a) (b)

Fig. (6-1): FWFS machine test rig

6.1 The experimental rig for the FWFS machine

The Fig. 6-1 shows experimental rig configuration while the control scheme used during the experiments is shown on Fig. 6-2.

The rig was controlled through modular dSpace that was connected to three SKAI modules connected to a common DC link bus bars.

First two SKAI modules were used for powering the FWFS, one for armature, and second as a DC/DC converter to supply the field winding. Third SKAI module controlled the IM.

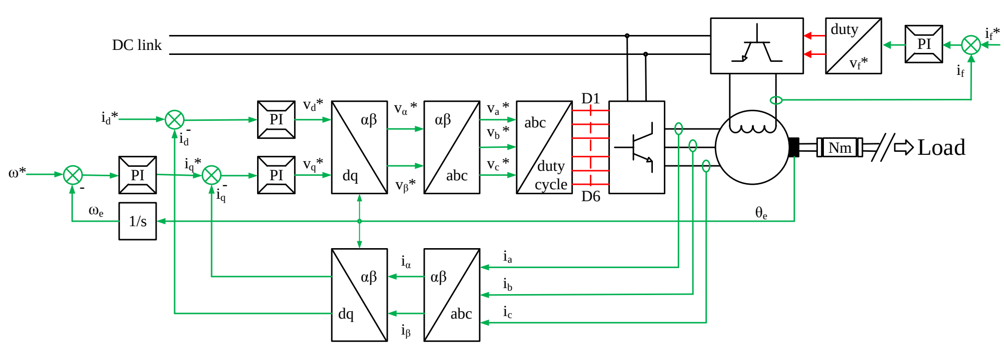

Fig. (6-2): FWFS drive control diagram

6.2 No load experiments

Figure Fig. 6-3 captures the BEMF amplitudes during the no load test with three different levels of field current from speed of 100rpm up 1400rpm. As shows very good match with the FEA model across the full spectrum of speeds and tested levels of the field currents. Some samples captured on via scope are presented in Fig. 6-4 where the Y axis is common for both, DC field current (blue colour) and the three phase armature BEMF. It shows the quality of the DC current control without any ripples or noise.

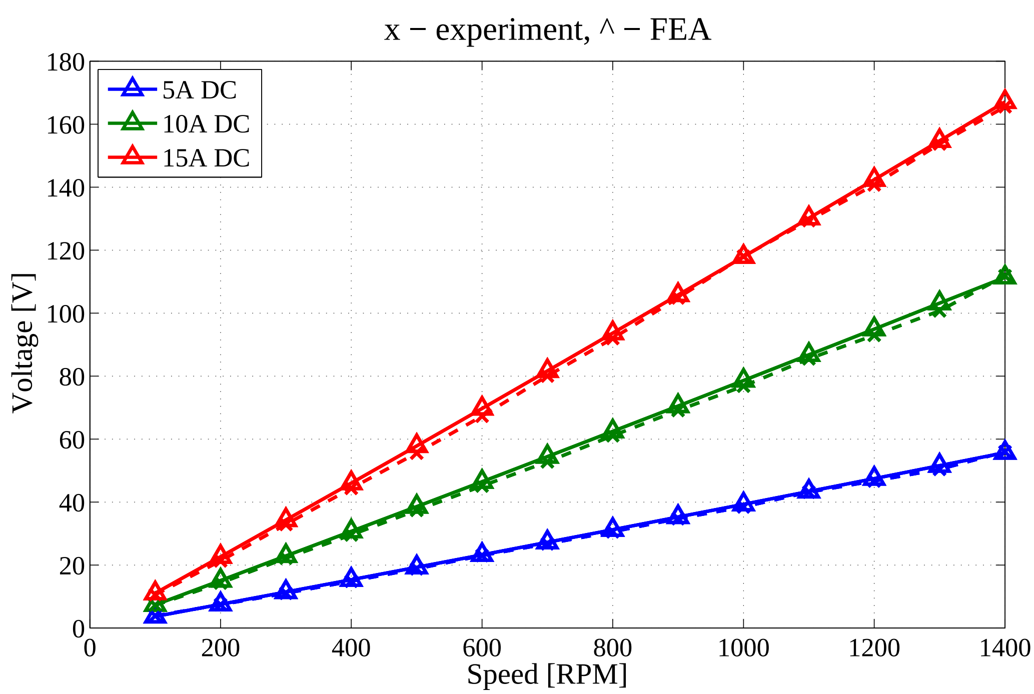

Fig. (6-3): FWFS machine at no load with varying speed and field current

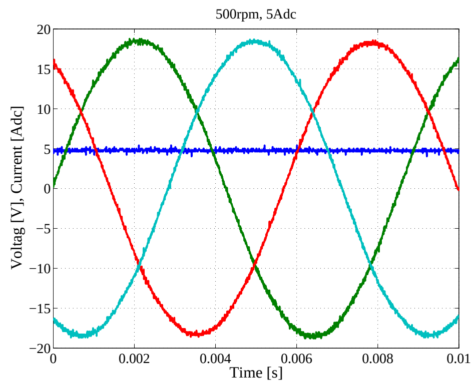

(a) 500rpm, $i_f = 5A$

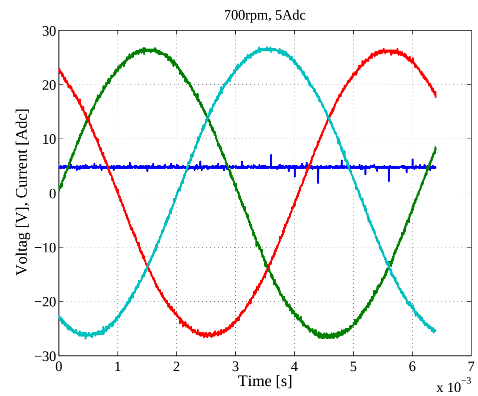

(b) 700rpm, $i_f = 5A$

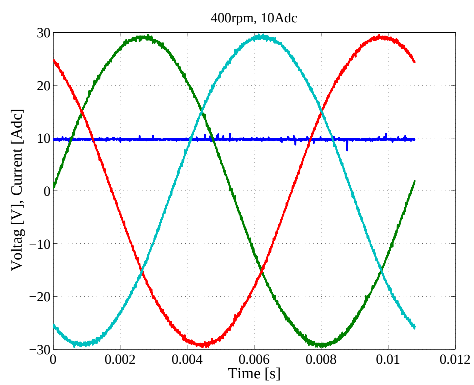

(c) 400rpm, $i_f = 10A$

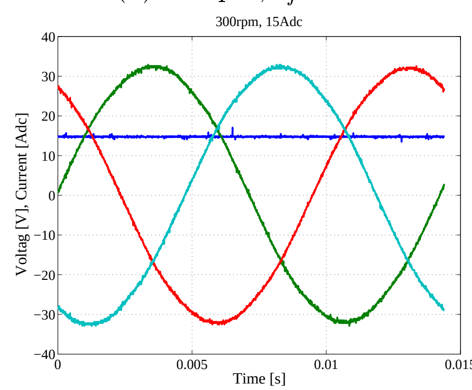

(d) 300rpm, $i_f = 15A$

Fig. (6-4): Set of no load experiment results with various speeds and field currents

6.3 Load Test

The FWFS machine was tested under load in range of i_q current from $5A$ to $25A$ and in terms of field current i_f from $5A$ to $15A$. These values have been chosen as in the tested coil arrangement, when the armature winding is formed from the coils connected in series and phases connected in star and all the field coils are connected in series as well, the current loading in compare to Gen 3.1 is $16Arms$. although due to the large air gap and, half of the slots used for field winding and with no PM, the results show that these two machines are too different to be comparable.

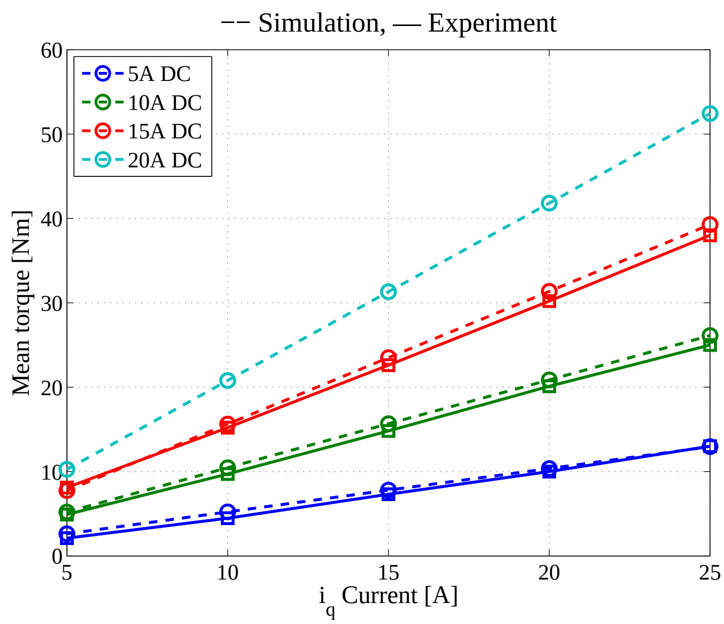

Fig. (6-5): Load test with various values of armature and field current at speed of 100rpm

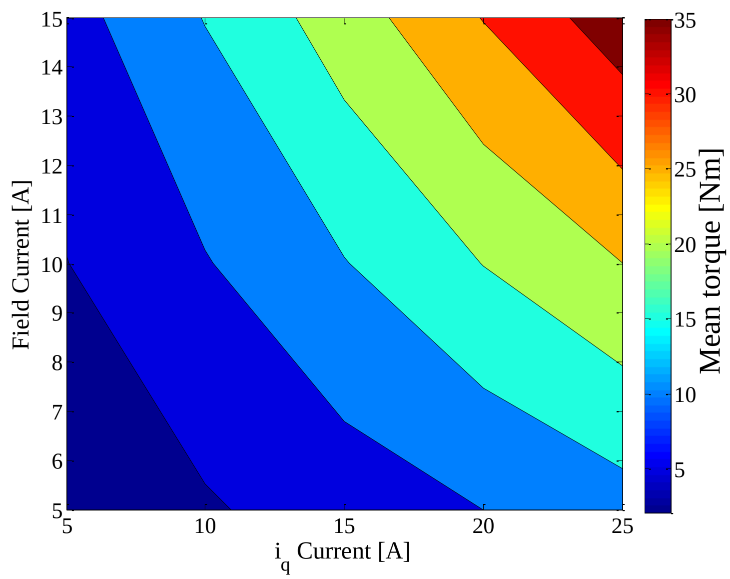

Fig. (6-6): Torque map of the FWFS machine for 100rpm and various values of the armature and field current

6.4 Conclusion

In this chapter, the experiment results and performance under the no load and load conditions are presented. The results confirm the prediction, that the decision to design the machine with the 4 mm air gap will have significant influence on its performance. In details, at the comparable copper loses, the FWFS machine delivers sixteen times lower torque in compare to Gen 3.1. However, in previous chapter was shown that this could be addressed through reduction of the air gap thickness. It was also shown that the FWFS machine with 0.5 mm air gap would be capable of torque only 1.8 times lower compared to Gen.3.1. It was shown, that although there is a potential in the rotor design for improvement, the restrictions given by, but not only, the original design of the stator, the geometry of the magnetic circuit, the number of turns per coil and conductor cross section area are too strict to give enough variability to design a machine with a competitive performance in compare to the Gen3.1. The data obtained from the simulations match those from experiment results and also the concept of FWFS with unusual ratio of axial length to rotor diameter has been proved as valid.

Chapter 7

Conclusion

The thesis addresses the design and tests of the unconventional electrical machine topologies designed for more electric applications in which the fault tolerance and torque density are the main factors. The challenges of utilising the PM material within the machine and their advantages over field wound solutions are addressed through an extensive simulation study and experimental validations. Initially, the unconventional FRM topology is proposed to improve the FTe capability and lower the costs whilst achieving significant improvement in the torque with minimal volume of PM material. The FRM was manufactured and the results of the FEA were validated through experimental work. The experiments have confirmed that the predicted results have good agreement under both the no load conditions and load conditions.

It also has been confirmed that the machine can be classified as the FT machine because it satisfies the FT criteria in which continuous operation under fault can be performed and thus the function can be maintained by overloading the machine whilst accommodating the fault. Though, the machine belongs into the FT category, an inter-turn fault will be a problematic since the field due to the magnet cannot be simply removed. However, the PMs can be accommodated if the appropriate design selection in terms of slot and pole numbers has been made.

In Chapter 4, the influence of the S/P combination on inter-turn SC current in permanent magnet assisted machines was investigated. The 2D sub-domain field computational model with the MOGA was used for the design and performance prediction of the considered machines. The machines' electromagnetic losses including iron, magnet and winding losses were systematically calculated using analytical tools. During the post processing stage, the 1D analysis was employed for turn-turn fault analysis. The method calculates self and mutual inductances of both the faulty and healthy turns under the SC fault condition with respect to the fault locations, and thus the SC fault current considering its location. Eight FT PM machines with different S/P combinations were analysed. Both the performance of the machine during normal operation and when currents were induced during the turn-turn SC fault were investigated. To evaluate the thermal impact of each S/P combination under the inter-turn fault condition, the thermal analysis was undertaken using FEM. It was concluded that the low rotor pole number machines have better fault tolerance capability whilst the high rotor pole number machines are lighter and provide higher efficiency. However, FTe is still challenging if the it combination with high performance is required to be achieved by the application.

To overcome the challenges related to the SC fault, the topology which eliminates the PM material and works on a basis of the field winding was developed in Chapter 5. As the SC fault cannot be fully eliminated, the solution which prevent the catastrophic failure and minimises the consequences by using the excitation system instead of the PM was proposed. The modification of PM machine towards improvement of the FTe was presented in detail. Different rotor structures were investigated and optimised to maximise the torque performance. It has been confirmed that using stator of existing machine and replacing the current rotor containing PMs not only improve the FTe but also down size the manufacturing and material costs.

Finally, the proposed machine solution was tested at both load and no load condition. It was shown that the assumptions based on the FEA were valid and the machine has the potential in applications where FT and excitation field weakening performances are required. The advantage of fully controllable and hence removable excitation field limits the volt-amp rating and the losses associated to the converter.

7.1 Future work

The study will be further extended through following studies:

- Due to the restrictions on the stator in considered design, only rotor is optimised to enhance the torque. The torque density of the design can be further improved adopting completely free stator and rotor selection in which the winding methodology and magnetic path will be investigated.

- Another challenge involved in the field wound flux switching machine is to investigate the rotor losses which take place in the rotor hub. Different material selection allows minimising the losses whilst enhancing the mechanical stability. Also alternative rotor structure made of laminated steel can be considered to minimise the rotor magnetic losses as shown in Fig. 7-1 below. The design the magnetic path has to be optimised in order to improve the performance.

- To achieve the most out of the separated armature and field winding, both the field winding and armature winding should be controlled separately. However, using the field winding as an input filter of DC link side of the 3 phase voltage converter, both the windings can be controlled as a modular approach where field winding connected to DC side and armature winding controlled by H-bridge.

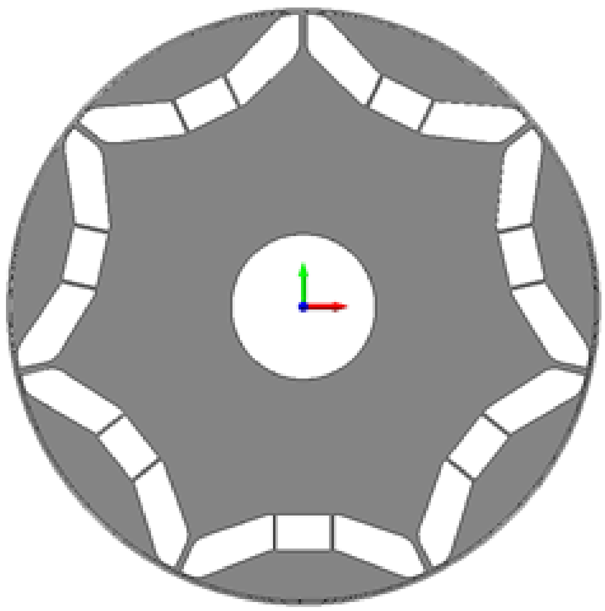

Fig. (7-1): Concept of new FWFSM rotor

Appendix A

List of publications

A.1 Journal papers

J. Dusek, P. Arumugam, C. Brunson, E. Amankwah, T. Hamiti, and C. Gerada, "**Impact of Slot/Pole Combination on Inter-Turn Short Circuit Current in Fault Tolerant Permanent Magnet Machines**," *IEEE Transactions on Magnetics*, vol. 52, no. 4, p. 1–9, Apr 2016.

P. Arumugam, J. Dusek, S. Mezani, T. Hamiti, and C. Gerada, "**Modelling and analysis of eddy current losses in permanent magnet machines with multi-stranded bundle conductors**," *Math. Comput. Simul.*, Nov 2015.

A.2 International conferences

J. Dusek, P. Arumugam, T. Hamiti, and C. Gerada, "**Selection of slot-pole combination of permanent magnet machines for aircraft actuation**," in *Electr. Syst. Aircraft, Railw. Sh. Propuls. Road Veh. (ESARS), 2015 Int. Conf.*, pp. 1–5, 2015.

P. Arumugam, J. Dusek, A. Aigbomian, G. Vakil, S. Bozhko, T. Hamiti, C. Gerada, and W. Fernando, "**Comparative Design Analysis of Permanent Magnet Rotor Topologies for an Aircraft Starter-Generator**," pp. 273–278, 2014.

Appendix B

FWFS rig and manufacturing

B.1 Stator

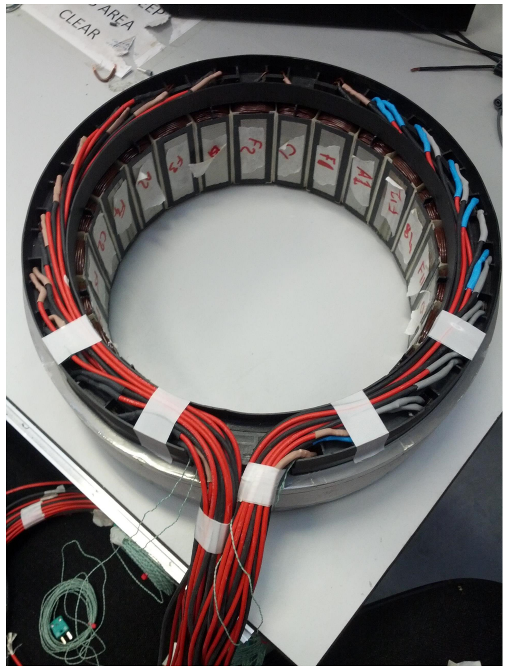

Fig. (B.1): Reconnection of the stator coils - detail

Fig. (B.2): Reconnection of the stator coils - wider view

B.2 Rotor hub

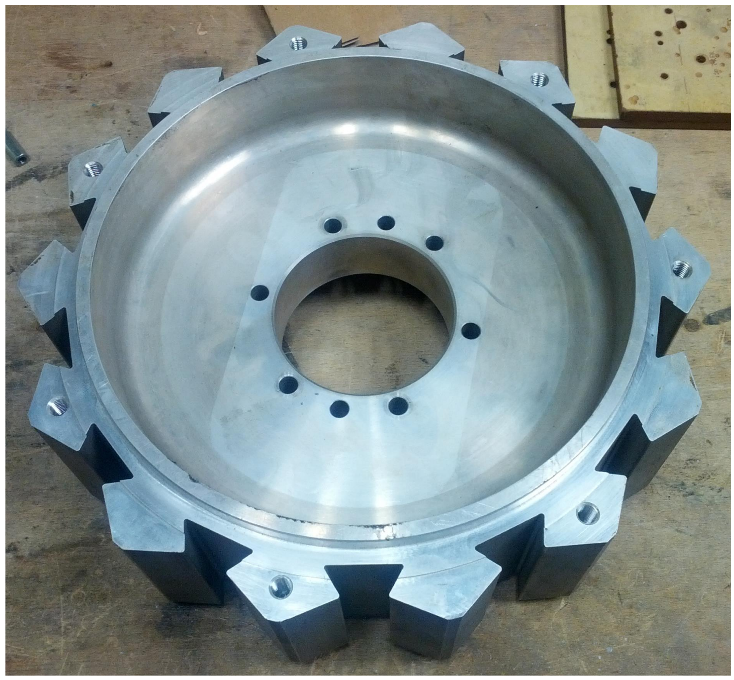

Fig. (B.3): Aluminium rotor support

B.3 Rotor segments

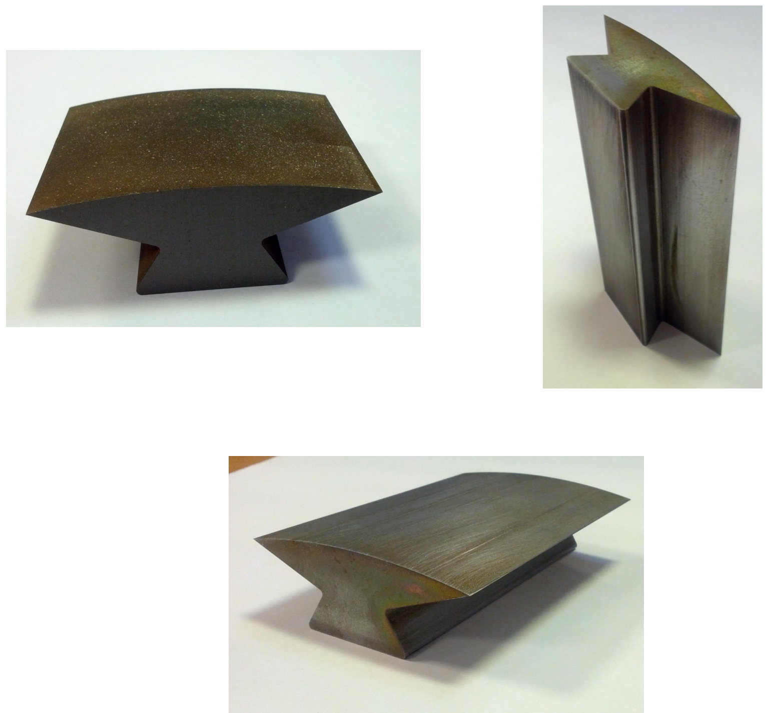

Fig. (B.4): Rotor segment cut out

B.4 The FWFS test rig

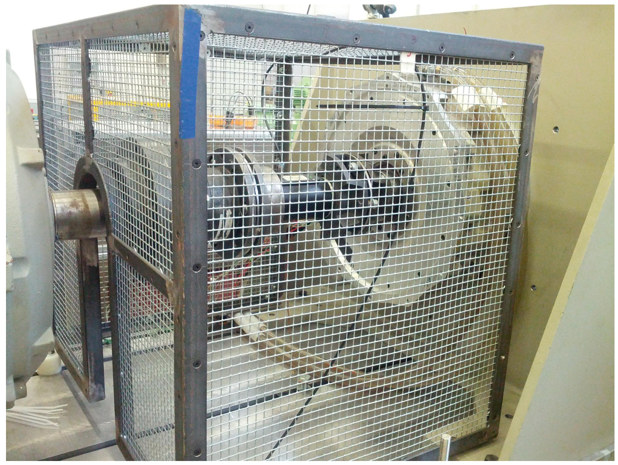

Fig. (B.5): Coupling between the IM and FWFS machine with torque meter

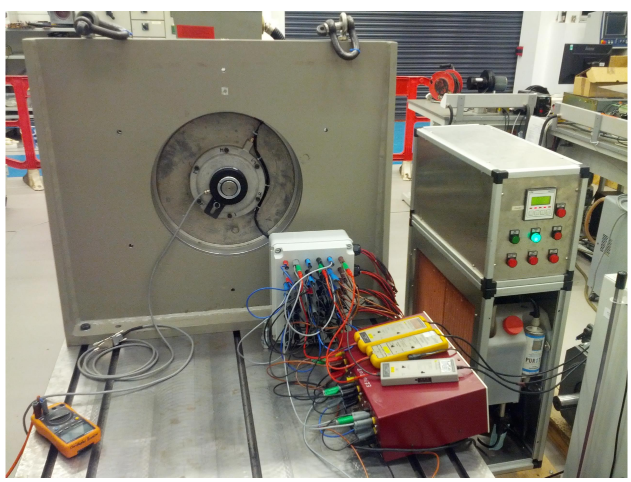

Fig. (B.6): Backe end of the FWFS machine with encoder and coils terminal box

Fig. (B.7): The cabinet with the SKAI modules

Fig. (B.8): dSpace + interface board

Appendix C

Rotor drafts

CREO PARAMETRIC

REL NO	REV	DETAIL	DWN	CKD	APVD	DATE
ECO-139704	A	DEVELOPMENT_RELEASE	NRD	TP	TP	28NOV13

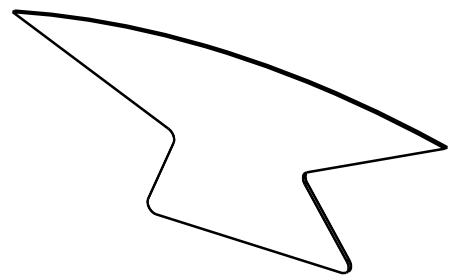

ISOMETRIC VIEW

NOTES:

1. LAMINATION THICKNESS 0.35mm.

2. MATERIAL: SILICON STEEL M235-35A C5 COATING.

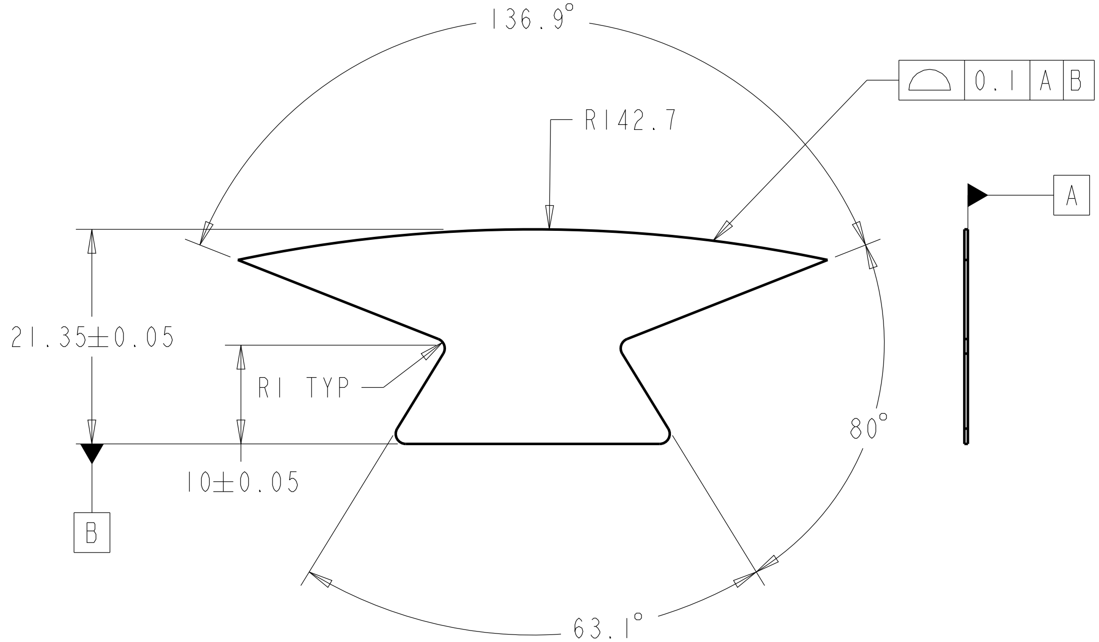

UNLESS OTHERWISE SPECIFIED, ALL DIMENSIONS ARE IN MILLIMETERS

DIM		HOLE
X ± 0.2		0.00- 4.99 +0.15/-0.08
X.X ± 0.2		5.00- 9.99 +0.20/-0.10
X.XX± 0.2		10.00-17.49 +0.25/-0.13
		17.50-24.99 +0.30/-0.13

ANG TOL: ± 0.5° SCALE: 2.000

SIM TO .

DO NOT SCALE PRINT

- CONFIDENTIAL - PROPERTY OF CUMMINS GENERATOR TECHNOLOGIES

DWN NRD
CKD TP
APVD TP
DATE 28NOV13

FOR INTERPRETATION OF DIMENSIONING AND TOLERANCING, SEE ASME Y14.5M-1994

FIRST USED ON -

SITE CODE STA

CUMMINS GENERATOR TECHNOLOGIES

LAMINATION, ROTOR

.

DWG SIZE A3 A048G661 SHEET 1 REV A

CREO PARAMETRIC

REL NO	REV	DETAIL	DWN	CKD	APVD	DATE
ECO-139704	A	DEVELOPMENT_RELEASE	NRD	TP	TP	28NOV13

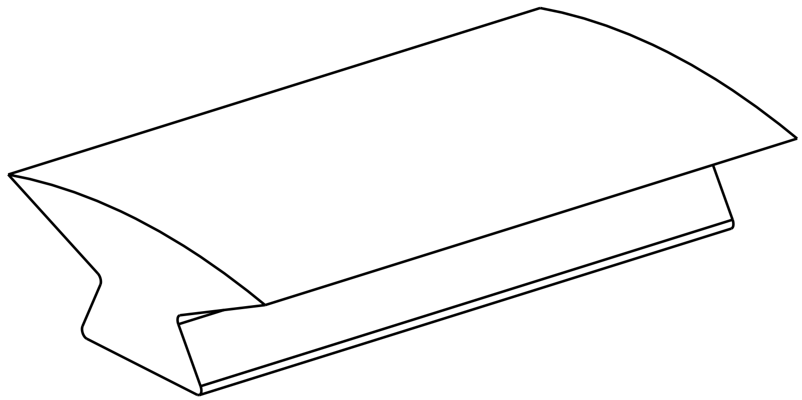

ISOMETRIC VIEW

NOTE:

1. FOR LAMINATION REFER TO DRAWING 'ROTOR LAMINATION A048G661'

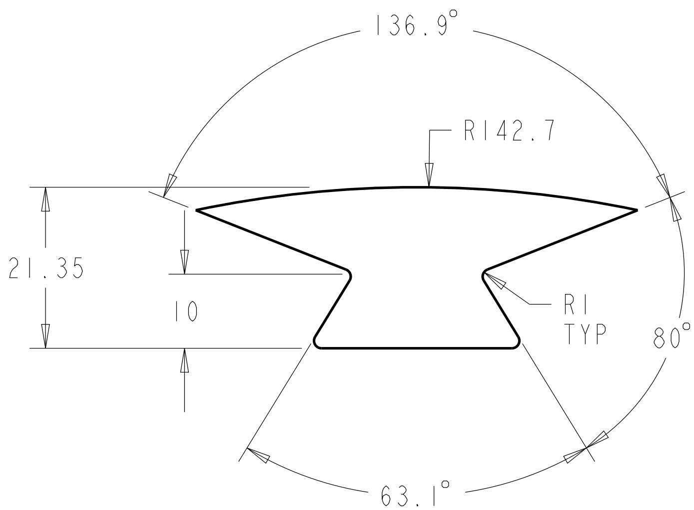

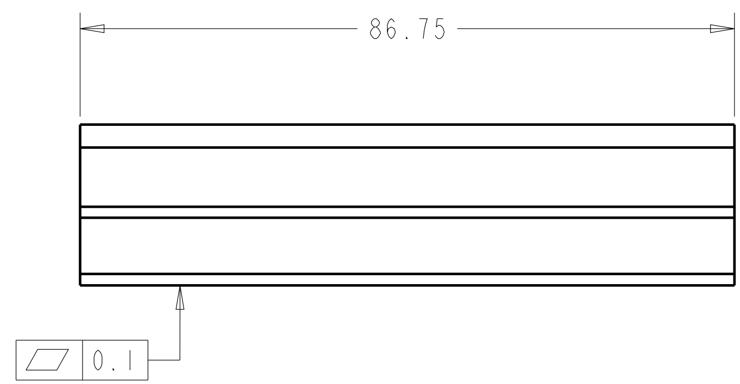

UNLESS OTHERWISE SPECIFIED, ALL DIMENSIONS ARE IN MILLIMETERS		
DIM	X ± 0.2 X.X ± 0.2 X.XX± 0.2	HOLE 0.00- 4.99 +0.15/-0.08 5.00- 9.99 +0.20/-0.10 10.00-17.49 +0.25/-0.13 17.50-24.99 +0.30/-0.13
ANG TOL: ± 0.5°	SCALE: 1.500	

SIM TO .

DO NOT SCALE PRINT

- CONFIDENTIAL -
PROPERTY OF CUMMINS GENERATOR TECHNOLOGIES

DWN	NRD
CKD	TP
APVD	TP
DATE	28NOV13
FOR INTERPRETATION OF DIMENSIONING AND TOLERANCING, SEE ASME Y14.5M-1994	FIRST USED ON -

SITE CODE STA

CUMMINS GENERATOR TECHNOLOGIES

LAMINATION, ROTOR

.

DWG SIZE		SHEET	REV
A3	A048G756	1	A

REL NO	REV	DETAIL	DWN	CKD	APVD	DATE
ECO-120782	A	SHEET 1	TBP	RPM	KP	08MAR13

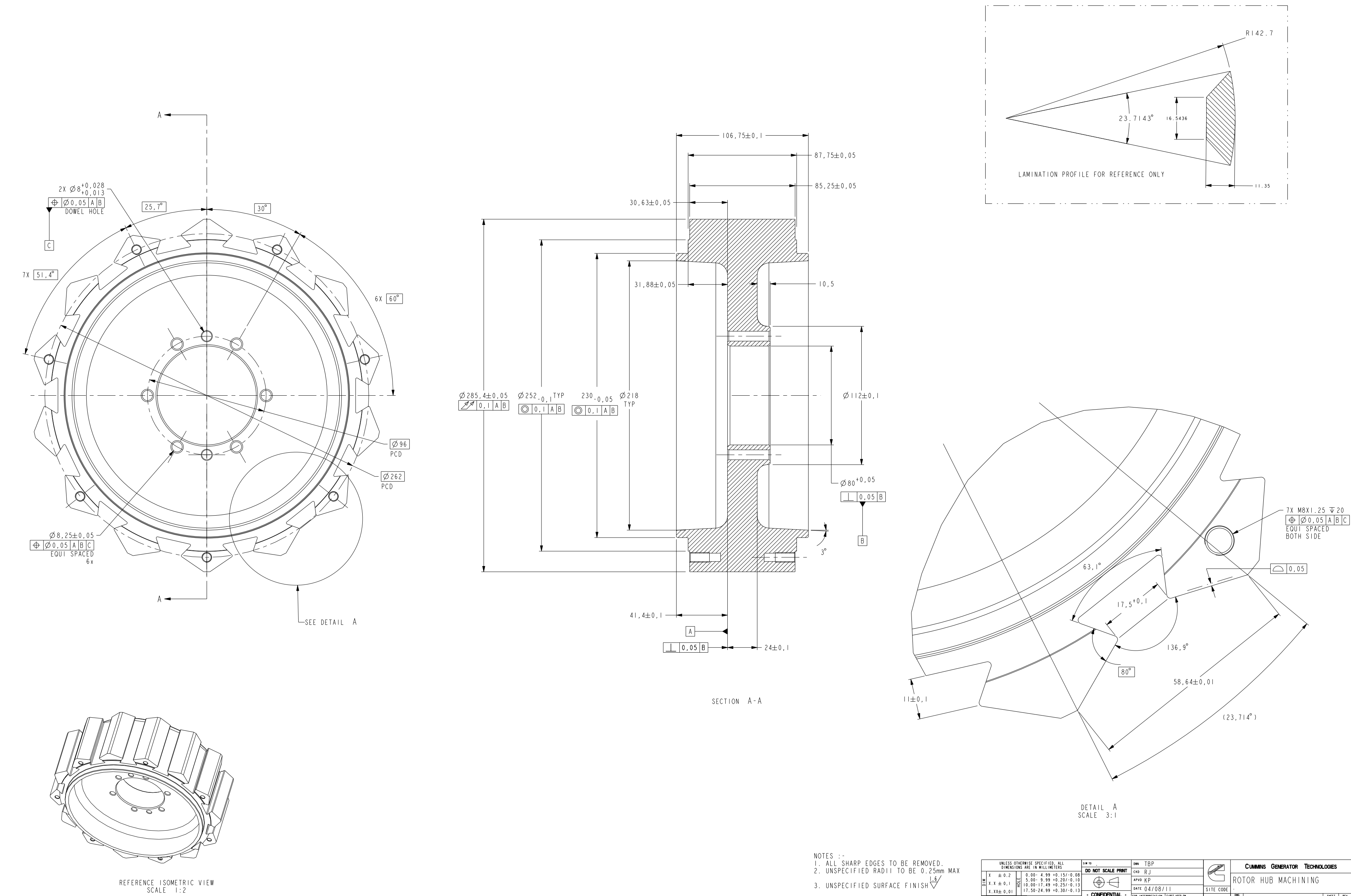

NOTES :-
1. ALL SHARP EDGES TO BE REMOVED.
2. UNSPECIFIED RADII TO BE 0.25mm MAX
3. UNSPECIFIED SURFACE FINISH 1.6

UNLESS OTHERWISE SPECIFIED, ALL DIMENSIONS ARE IN MILLIMETERS

X ±0.2 | X.X ±0.1 | X.XX ±0.01

HOLE: 0.00-4.99 +0.15/-0.08 | 5.00-9.99 +0.20/-0.10 | 10.00-17.49 +0.25/-0.13 | 17.50-24.99 +0.30/-0.13

ANG TOL: ± 0.5° | SCALE: 1:1

DO NOT SCALE PRINT

- CONFIDENTIAL - PROPERTY OF CUMMINS GENERATOR TECHNOLOGIES

DWN TBP | CKD RJ | APVD KP | DATE 04/08/11

FIRST USED ON: MGI GEN3 | SITE CODE: STA

CUMMINS GENERATOR TECHNOLOGIES

ROTOR HUB MACHINING

A0 A045S849 | SHEET 1 | REV A

Pro/ENGINEER

Pro/ENGINEER

REL NO	REV	DETAIL	DWN	CKD	APVD	DATE
ECO-133029	A	DEVELOPMENT RELEASE	TBP	TBP	NB	07MAR13

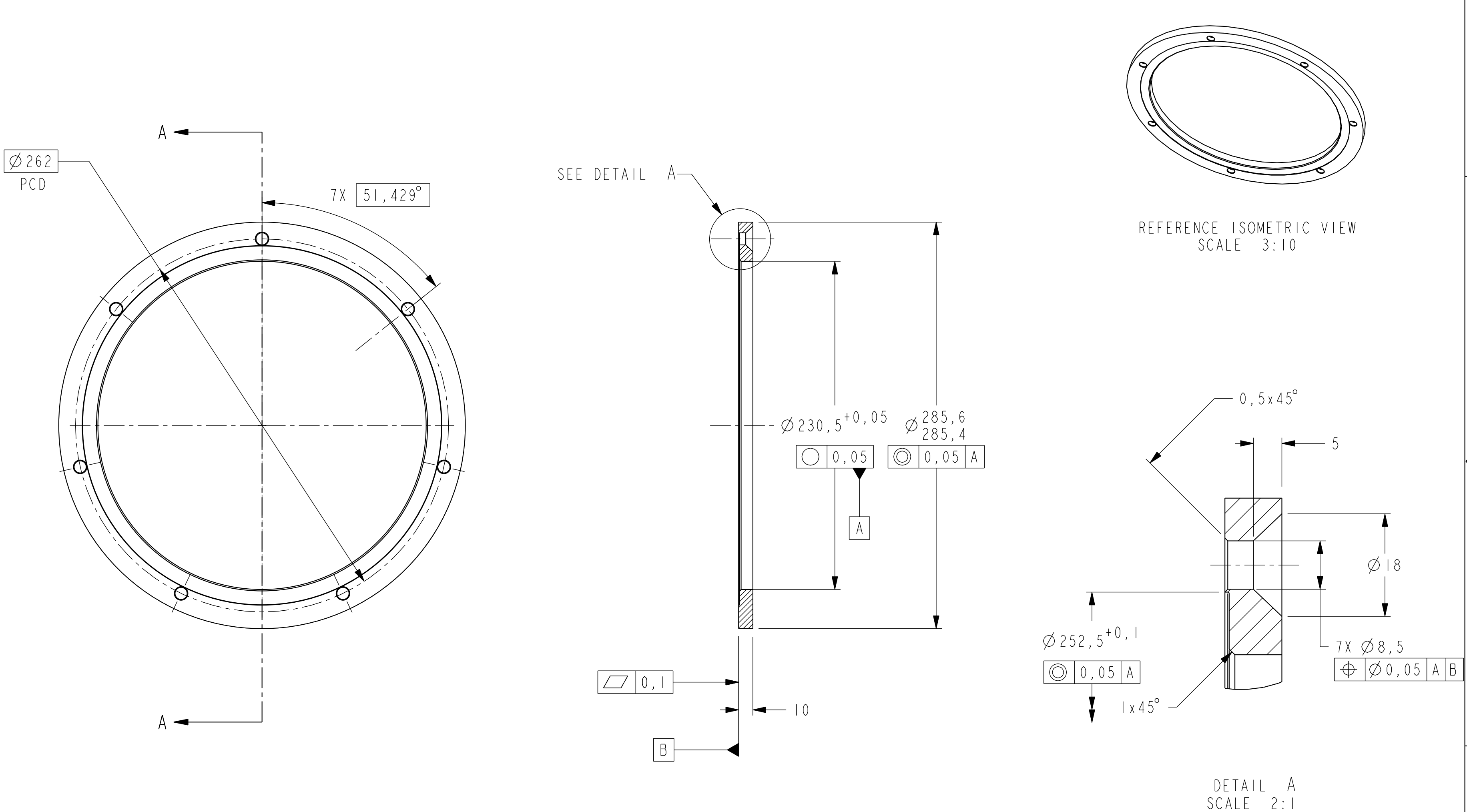

SECTION A-A

DETAIL A
SCALE 2:1

NOTES :-
1. ALL SHARP EDGES & BURRS TO BE REMOVED.
2. UNSPECIFIED RADII TO BE 0.25mm MAX
3. UNSPECIFIED SURFACE FINISH 1.6

PRELIMINARY ISSUE
DRAWING IS SUBJECT TO CHANGE
DRAWING IS FOR REFERENCE, PRE-PRODUCTION, PROTOTYPING
AND QUOTING PURPOSES ONLY
DRAWING MUST NOT BE USED FOR PRODUCTION MANUFACTURE

UNLESS OTHERWISE SPECIFIED, ALL DIMENSIONS ARE IN MILLIMETERS

DIM		HOLE	
	X ± 0.20		0.00- 4.99 +0.15/-0.08
	X.X ± 0,1		5.00- 9.99 +0.20/-0.10
	X.XX± 0,01		10.00-17.49 +0.25/-0.13
			17.50-24.99 +0.30/-0.13
ANG TOL: ± 0,5°		SCALE:	3:10

SIM TO .
DO NOT SCALE PRINT
- CONFIDENTIAL -
PROPERTY OF CUMMINS GENERATOR TECHNOLOGIES

DWN TBP
CKD TBP
APVD NB
DATE 07MAR13
FOR INTERPRETATION OF DIMENSIONING AND TOLERANCING, SEE ASME Y14.5M-1994
FIRST USED ON MGI Gen3.1
SITE CODE STA

CUMMINS GENERATOR TECHNOLOGIES
MAGNET RETAINING RING
DWG SIZE A2 A045S851
SHEET 1 REV A

Bibliography

[1] F. Movements, "EUROCONTROL Seven-Year Forecast September 2015," no. September, 2015.

[2] M. Provost, "The More Electric Aero-engine: a general overview from an engine manufacturer," in *Int. Conf. Power Electron. Mach. Drives*, vol. 2002, pp. 246–251, IEE, 2002.

[3] A. A. AbdElhafez and A. J. Forsyth, "A Review of More-Electric Aircraft," 2009.

[4] H. H. Chary, R. A. Miller, and R. Summers, "Electrical Machines," *Flight Int.*, p. 162, 1963.

[5] A. Tessarolo and F. Luise, "Design for Improved Fault Tolerance in Large Synchronous Machines," *2015 IEEE Work. Electr. Mach. Des. Control Diagnosis*, pp. 45–52, mar 2015.

[6] Mehdi Khosrowpour, *Dictionary of Information Science and Technology.* Idea Group Inc (IGI), 2012.

[7] R. Gumzej, *Real-time Systems' Quality of Service: Introducing Quality of Service Considerations in the Life Cycle of Real-time Systems.* Springer Science & Business Media, 2010.

[8] M. . S. RUBA L., M. Ruba, and L. Szabó, "Fault Tolerant Electrical Machines. State of the Art and Future Directions," *J. Comput. Sci. Control Syst.*, vol. 1, no. 1, pp. 202–207, 2008.

[9] S. Wang, M. Tomovic, and H. Liu, *Commercial Aircraft Hydraulic Systems: Shanghai Jiao Tong University Press Aerospace Series.* Elsevier Science, 2015.

[10] a.G. Jack, B. Mecrow, and J. Haylock, "A comparative study of permanent magnet and switched reluctance\nmotors for high performance fault tolerant applications," *IAS '95. Conf. Rec. 1995 IEEE Ind. Appl. Conf. Thirtieth IAS Annu. Meet.*, vol. 1, no. 4, pp. 889–895, 1995.

[11] P. Kakosimos, E. Tsampouris, and A. Kladas, "Design Considerations in Actuators for Aerospace Applications," *Magn. IEEE Trans.*, vol. 49, no. 5, pp. 2249–2252, 2013.

[12] J. Urresty, J. Riba, and L. Romeral, "A Back-emf Based Method to Detect Magnet Failures in PMSMs," *Magn. IEEE Trans.*, vol. 49, no. 1, pp. 591–598, 2013.

[13] L. Jiangui, K. T. Chau, J. Z. Jiang, L. Chunhua, and L. Wenlong, "A New Efficient Permanent-Magnet Vernier Machine for Wind Power Generation," *Magn. IEEE Trans.*, vol. 46, no. 6, pp. 1475–1478, 2010.

[14] J. R. Riba Ruiz, J. A. Rosero, A. G. Espinosa, and L. Romeral, "Detection of Demagnetization Faults in Permanent-Magnet Synchronous Motors Under Nonstationary Conditions," *Magn. IEEE Trans.*, vol. 45, no. 7, pp. 2961–2969, 2009.

[15] W. Jiabin, K. Atallah, and D. Howe, "Optimal torque control of fault-tolerant permanent magnet brushless machines," *Magn. IEEE Trans.*, vol. 39, no. 5, pp. 2962–2964, 2003.

[16] C. Wenping, B. C. Mecrow, G. J. Atkinson, J. W. Bennett, and D. J. Atkinson, "Overview of Electric Motor Technologies Used for More Electric Aircraft (MEA)," *Ind. Electron. IEEE Trans.*, vol. 59, no. 9, pp. 3523–3531, 2012.

[17] C. Gerada and K. J. Bradley, "Integrated PM Machine Design for an Aircraft EMA," *Ind. Electron. IEEE Trans.*, vol. 55, no. 9, pp. 3300–3306, 2008.

[18] P. Arumugam, T. Hamiti, C. Brunson, and C. Gerada, "Analysis of Vertical Strip Wound Fault-Tolerant Permanent Magnet Synchronous Machines," *Ind. Electron. IEEE Trans.*, vol. 61, no. 3, pp. 1158–1168, 2014.

[19] P. Arumugam, T. Hamiti, and C. Gerada, "Modeling of Different Winding Configurations for Fault-Tolerant Permanent Magnet Machines to Restrain Interturn Short-Circuit Current," *Energy Conversion, IEEE Trans.*, vol. 27, no. 2, pp. 351–361, 2012.

[20] B. C. Mecrow, A. G. Jack, J. A. Haylock, and J. Coles, "Fault-tolerant permanent magnet machine drives," *Electr. Power Appl. IEE Proc. -*, vol. 143, no. 6, pp. 437–442, 1996.

[21] R. P. Deodhar, S. Andersson, I. Boldea, and T. J. E. Miller, "The flux-reversal machine: a new brushless doubly-salient permanent-magnet machine," in *Ind. Appl. IEEE Trans.*, vol. 33, pp. 925–934, 1996.

[22] S. E. Rauch and L. J. Johnson, "Design Principles of Flux-Switch Alternators," *Power Appar. Syst. Part III. Trans. Am. Inst. Electr. Eng.*, vol. 74, no. 3, pp. 1261–1268, 1955.

[23] M. Cheng, W. Hua, J. Zhang, and W. Zhao, "Overview of Stator-Permanent Magnet Brushless Machines," *Ind. Electron. IEEE Trans.*, vol. 58, no. 11, pp. 5087–5101, 2011.

[24] I. Boldea, E. Serban, and R. Babau, "Flux-Reversal Stator PM Single Phase Generator with Controlled DC Output," in *OPTIM-96*, pp. 1123–1137, 1996.

[25] C. Wang, S. A. Nasar, and I. Boldea, "Three-phase flux reversal machine (FRM)," *Electr. Power Appl. IEE Proc. -*, vol. 146, no. 2, pp. 139–146, 1999.

[26] X. Luo, D. Qin, and T. Lipo, "A novel two phase doubly salient permanent magnet motor," in *IAS '96. Conf. Rec. 1996 IEEE Ind. Appl. Conf. Thirty-First IAS Annu. Meet.*, vol. 2, pp. 808–815, IEEE, 1996.

[27] Y. Liao, F. Liang, T. a. Lipo, L. Yuefeng, L. Feng, and T. a. Lipo, "A novel permanent magnet motor with doubly salient structure," *Ind. Appl. IEEE Trans.*, vol. 31, no. 5, pp. 1069–1078, 1995.

[28] K. Dooley and M. Dowhan, "Method and apparatus for controlling an electric machine," 2008.

[29] J. G. Washington, G. J. Atkinson, N. J. Baker, A. G. Jack, B. C. Mecrow, B. B. Jensen, L. Pennander, G. Nord, and L. Sjoberg, "An improved torque density Modulated Pole Machine for low speed high torque applications," in *Power Electron. Mach. Drives (PEMD 2012), 6th IET Int. Conf.*, pp. 1–6, 2012.

[30] D. S. More and B. G. Fernandes, "Power density improvement of three phase flux reversal machine with distributed winding," *Electr. Power Appl. IET*, vol. 4, no. 2, pp. 109–120, 2010.

[31] D. S. More, H. Kalluru, and B. G. Fernandes, "Outer Rotor Flux Reversal Machine for Rooftop Wind Generator," in *Ind. Appl. Soc. Annu. Meet. 2008. IAS '08. IEEE*, pp. 1–6, 2008.

[32] I. Boldea, Z. Jichun, and S. A. Nasar, "Theoretical characterization of flux reversal machine in low-speed servo drives-the pole-PM configuration," *Ind. Appl. IEEE Trans.*, vol. 38, no. 6, pp. 1549–1557, 2002.

[33] G. Pellegrino and C. Gerada, "Modeling of Flux Reversal Machines for direct drive applications," in *Power Electron. Appl. (EPE 2011), Proc. 2011-14th Eur. Conf.*, pp. 1–10, 2011.

[34] D. S. More and B. G. Fernandes, "Novel three phase Flux Reversal Machine with full pitch winding," in *Power Electron. 2007. ICPE '07. 7th Internatonal Conf.*, pp. 1007–1012, 2007.

[35] D. S. More, H. Kalluru, and B. G. Fernandes, "d-q equivalent circuit representation of three-phase flux reversal machine with full pitch winding," in *Power Electron. Spec. Conf. 2008. PESC 2008. IEEE*, pp. 1208–1214, 2008.

[36] Y. Yang, J. Zhang, L. Ma, X. Wang, and N. Wang, "The electromagnetic performance calculation and comparison of flux reversal machine with different winding topologies," in *2014 17th Int. Conf. Electr. Mach. Syst.*, pp. 605–609, IEEE, oct 2014.

[37] D. S. More, H. Kalluru, and B. G. Fernandes, "Comparative analyis of Flux Reversal machine and Fractional slot concentrated winding PMSM," in *Ind. Electron. 2008. IECON 2008. 34th Annu. Conf. IEEE*, pp. 1131–1136, 2008.

[38] Heung-Kyo Shin, Tae Heoung Kim, and Cherl-Jin Kim, "Demagnetization characteristic analysis of inset-type-flux-reversal machines," 2012.

[39] H. Wei, W. Zhongze, and C. Ming, "A novel three-phase flux-reversal permanent magnet machine with compensatory windings," in *Electr. Mach. Syst. (ICEMS), 2010 Int. Conf.*, pp. 1117–1121, 2010.

[40] K. Tae Heoung, "A Study on the Design of an Inset-Permanent-Magnet-Type Flux-Reversal Machine," *Magn. IEEE Trans.*, vol. 45, no. 6, pp. 2859–2862, 2009.

[41] Y. Gao, R. Qu, D. Li, J. Li, G. Zhou, S. Member, D. Li, J. Li, and G. Zhou, "Consequent-Pole Flux-Reversal Permanent-Magnet Machine for Electric Vehicle Propulsion," *IEEE Trans. Appl. Supercond.*, vol. 26, pp. 1–5, jun 2016.

[42] T. Kim, "Demagnetization Characteristic Analysis of inset-type-flux-reveral machines.pdf," no. mm.

[43] A. Tura and Z. Dong, "A Review of Finite Element Analysis Method," 2012.

[44] E. Armando, R. I. Bojoi, P. Guglielmi, G. Pellegrino, and M. Pastorelli, "Experimental identification of the magnetic model of synchronous machines," *IEEE Trans. Ind. Appl.*, vol. 49, no. 5, pp. 2116–2125, 2013.

[45] A. Mitcham, G. Antonopoulos, and J. J. A. Cullen, "Implications of shorted turn faults in bar wound PM machines," *Electr. Power Appl. IEE Proc. -*, vol. 151, no. 6, pp. 651–657, 2004.

[46] J. A. Haylock, B. C. Mecrow, A. G. Jack, and D. J. Atkinson, "Operation of fault tolerant machines with winding failures," *Energy Conversion, IEEE Trans.*, vol. 14, no. 4, pp. 1490–1495, 1999.

[47] J. Dusek, P. Arumugam, T. Hamiti, and C. Gerada, "Selection of slot-pole combination of permanent magnet machines for aircraft actuation," in *Electr. Syst. Aircraft, Railw. Sh. Propuls. Road Veh. (ESARS), 2015 Int. Conf.*, pp. 1–5, 2015.

[48] A. M. El-Refaie, "Fault-tolerant permanent magnet machines: a review," *Electr. Power Appl. IET*, vol. 5, no. 1, pp. 59–74, 2011.

[49] L. Guohai, Y. Junqin, Z. Wenxiang, J. Jinghua, C. Qian, and G. Wensheng, "Design and Analysis of a New Fault-Tolerant Permanent-Magnet Vernier Machine for Electric Vehicles," *Magn. IEEE Trans.*, vol. 48, no. 11, pp. 4176–4179, 2012.

[50] A. S. Abdel-Khalik, S. Ahmed, A. M. Massoud, and A. A. Elserougi, "An Improved Performance Direct-Drive Permanent Magnet Wind Generator Using a Novel Single-Layer Winding Layout," *Magn. IEEE Trans.*, vol. 49, no. 9, pp. 5124–5134, 2013.

[51] T. Lubin, S. Mezani, and A. Rezzoug, "2-D Exact Analytical Model for Surface-Mounted Permanent-Magnet Motors With Semi-Closed Slots," *Magn. IEEE Trans.*, vol. 47, no. 2, pp. 479–492, 2011.

[52] T. Lubin, S. Mezani, and A. Rezzoug, "Analytical Computation of the Magnetic Field Distribution in a Magnetic Gear," *Magn. IEEE Trans.*, vol. 46, no. 7, pp. 2611–2621, 2010.

[53] K. Deb, A. Pratap, S. Agarwal, and T. Meyarivan, "A fast and elitist multiobjective genetic algorithm: NSGA-II," *Evol. Comput. IEEE Trans.*, vol. 6, no. 2, pp. 182–197, 2002.

[54] M. Popescu and D. G. Dorrell, "Proximity Losses in the Windings of High Speed Brushless Permanent Magnet AC Motors With Single Tooth Windings and Parallel Paths," *Magn. IEEE Trans.*, vol. 49, no. 7, pp. 3913–3916, 2013.

[55] A. Zulu, B. Mecrow, and M. Armstrong, "A wound-field three-phase flux-switching synchronous motor with all excitation sources on the stator," in *Energy Convers. Congr. Expo. 2009. ECCE 2009. IEEE*, pp. 1502–1509, 2009.